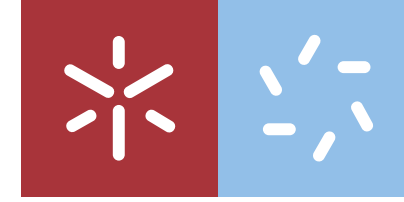




Study of the Förster Resonance Energy Transfer in Ensembles of Colloidal PbS Quantum Dots, emitting in the Near-Infrared Spectral Range

João Martins

UMinho | 2020



Universidade do Minho
Escola de Ciências

João Ricardo Gonçalves Martins

Study of the Förster Resonance Energy Transfer in Ensembles of Colloidal PbS Quantum Dots, emitting in the Near-Infrared Spectral Range

September 2020



Universidade do Minho

Escola de Ciências

João Ricardo Gonçalves Martins

**Study of the Förster Resonance Energy
Transfer in Ensembles of Colloidal PbS
Quantum Dots, emitting in the
Near-Infrared Spectral Range**

Master Dissertation
Master Degree in Physics

Dissertation supervised by
Mikhail I. Vasilevskiy
Willem L. Vos

DECLARATION

Nome: João Ricardo Gonçalves Martins

Endereço Eletrónico: pg35992@alunos.uminho.pt

Telemóvel: (+351) 913 054 072

Número de cartão de cidadão: 14742408

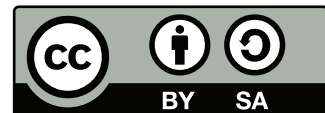
Título da dissertação: Study of the Förster Resonance Energy Transfer in Ensembles of Colloidal PbS Quantum Dots, emitting in the Near-Infrared Spectral Range

Orientadores: Mikhail I. Vasilevskiy e Willem L. Vos

Ano de conclusão: 2020

Designação do Mestrado: Mestrado em Física

Esta obra tem a licença **Creative Commons** “Atribuição-CompartilhaIgual 4.0 Internacional”.



Braga, setembro de 2020

João Ricardo Gonçalves Martins

ACKNOWLEDGEMENTS

First and foremost, I would like to thank my main advisor Mikhail Vasilevskiy and my co-supervisor Willem Vos, for providing me the essential guidance and knowledge in order to produce a nicely written dissertation, to develop my scientific research abilities and to consolidate my knowledge in the field of Condensed Matter Physics and Nano-Optics. For all the exchanged emails and long discussion meetings, I deeply thank your effort into this dissertation.

I would like also to thank COPS (Complex Photonic Systems) group of the University of Twente. Mainly, from this group, I would like to thank the essential help of Willem Vos, for being by main advisor during my stay at COPS, Andreas Schulz, who introduced me to the experimental procedures at the optical table and helped me on the chemistry procedure for binding quantum dot solutions, Matthijs Velsink, for all the kind technical help and the essential exchange of knowledge regarding the experimental procedures and data treatment, Christian Blum, for his great insights and help on the conceiving of the experiments, and Cornelis Hartevelde, for his great technical assistance in the laboratory. To the remaining group I thank you all for all exchange of knowledge during the COPS Monday meetings, your companionship and your friendship during my stay in the University of Twente.

I would like to thank Richard Egberink, from the Molecular Nanofabrication (MNF) research group of the University of Twente, for his essential mentoring on producing cross-linked quantum dots using EDC/NHS surface chemistry.

I would like to thank the Erasmus+ scholarship, which made possible my stay in Enschede, in The Netherlands, working at COPS, in the University of Twente, where I developed the basic experimental content of this dissertation.

I would like to thank my friends, family and my parents for all the love, support and encouragement, crucial for surpassing high demanding tasks. Specially, I thank my grandmother for being to me an eternal example of a great human being.

STATEMENT OF INTEGRITY

I hereby declare having conducted this academic work with integrity. I confirm that I have not used plagiarism or any form of undue use of information or falsification of results along the process leading to its elaboration.

I further declare that I have fully acknowledged the Code of Ethical Conduct of the University of Minho.

RESUMO

Titulo: *Estudo da transferência ressonante de energia de Förster em amostras coloidais de pontos quânticos de PbS, emissores no infravermelho próximo.*

A transferência ressonante de energia de Förster (em inglês, *Förster resonance energy transfer*, ou, simplesmente, FRET) é um mecanismo de transferência de energia não radiativo presente entre duas unidades fluorescentes, como dois pontos quânticos ou duas moléculas. Neste mecanismo, um dador excitado (por exemplo, um ponto quântico ou uma molécula) transfere a sua energia de excitação para um aceitador (outro ponto quântico ou molécula) com o qual se encontra em ressonância, por acoplamento dipolo-dipolo. O FRET é um mecanismo dominante entre emissores distanciados entre si a uma ordem dos nanómetros. Outros fatores dominantes que influenciam a eficiência deste mecanismo de transferência são a sobreposição do espectro de emissão do dador com o espectro de absorção do aceitador e a orientação relativa do momento dipolar de ambas as partículas. Este mecanismo tem também um papel fundamental em processos biológicos como a fotossíntese em plantas e bactérias. Algumas aplicações de FRET podem ser encontradas em sistemas fotovoltaicos, na análise de distâncias e interações moleculares, e no armazenamento de informação quântica.

O objetivo principal desta tese de mestrado é a deteção do mecanismo de FRET numa mistura coloidal de duas amostras pontos quânticos de PbS (símbolo químico para Galena, ou sulfeto de chumbo) com diferentes tamanhos, que são unidas por processos de química de superfícies. Estes processos químicos promovem, neste caso específico, ligações cruzadas físicas entre dois, ou mais, pontos quânticos, a uma distância da ordem dos nanómetros, que promove a presença de FRET. A deteção de FRET em sistemas de pontos quânticos que emitem no espectro infravermelho próximo (isto é, com comprimentos de onda entre $0.7 - 1.4\mu\text{m}$), como os pontos quânticos de PbS, não é amplamente encontrada na literatura, a qual foca na deteção de mecanismos de FRET em pontos quânticos que emitem no espectro visível, como pontos quânticos de CdTe ou CdSe. O espectro infravermelho próximo permite, como exemplo, aplicações em cristais fotónicos, aonde o mecanismo de FRET é predomi-

nante pela inibição da emissão radiativa espontânea, assim como a aplicação em lasers que emitem no infravermelho e absorção de luz no infravermelho em sistemas fotovoltaicos. De forma a detectar a presença de FRET nas amostras de pontos quânticos, foram medidos espectros de emissão e cinéticas fotoluminescentes, estas obtidas por técnicas de resolução temporal de fotoluminescência como TCSPC (em inglês, *Time Correlated Single Photon Counting*).

Em conjunto com os resultados experimentais obtidos, é apresentado nesta tese o estudo estatístico das cinéticas fotoluminescentes das amostras de pontos quânticos PbS, cujas cinéticas foram obtidas pela técnica de TCSPC. A partir desta análise estatística, é possível de avaliar e comparar várias propriedades das cinéticas, tais como o tempo médio de decaimento, o erro quadrático médio e a medida da assimetria da cinética obtida. De forma a compreender os resultados obtidos, alguns modelos de decaimentos do dador foram desenvolvidos e estudados, em conjunto com outras funções de decaimento que são encontradas na literatura. De forma a sustentar os modelos teóricos de decaimento, é também apresentado um tratamento teórico do mecanismo de FRET.

Palavras-chave: Pontos quânticos (QDots, ou QD), Transferência ressonante de energia de Förster (FRET), Sulfeto de chumbo (PbS)

ABSTRACT

Förster resonance energy transfer (FRET) is a non-radiative energy transfer mechanism between two light-emitting systems, such as two quantum dots (QDots) or molecules. This mechanism involves an excited donor fluorophore (e.g., a QDot or a dye molecule) which transfers its energy of excitation to an acceptor (another QDot or molecule which is in resonance with the donor), via dipole-dipole coupling. FRET is the dominant type of energy transfer between emitters at a nanometre proximity. Other factors that influence the efficiency of this energy transfer mechanism include the spectral overlap of the donor emission spectrum and the acceptor absorption spectrum and the relative orientation of the dipole moment of both particles. In nature, for instance, FRET plays a dominant role in the energy transfer in photosynthetic apparatus of plants and bacteria. Some interesting applications of FRET can be found in photovoltaics, probing of molecular distances and molecular interactions, and storage and transfer of quantum information.

The main goal of this master thesis lies in detecting the presence of the FRET mechanism when two different colloidal QDot samples of PbS (short for Lead Sulfide), with different QDot size, are linked together via surface chemistry. This chemical procedure activates carboxyl or phosphate groups, which promote the binding of primary amines of organic glutathione QDot shell molecules. In other words, it promotes a cross-linkage between the organic shells of two, or more, quantum dots at a distance at which FRET is present. Using PbS quantum dots, which emit in the near-infrared (NIR) region of the light spectrum, these experiments can be reported as one of the first attempts to find The FRET mechanism in a near-infrared system of QDots. Most previous reports of FRET mechanisms were concerned with QDots which emit in the visible range, such as CdTe and CdSe QDots. The NIR spectral range, for instance, promotes interesting applications in photonic crystals, where FRET can be enhanced by spontaneous emission inhibition, in photovoltaics, in order to greatly absorb infrared light, and in the production of near-infrared QDot lasers. In order to find evidences of the presence of the FRET mechanism, emission spectra and time-resolved measurements, using the time correlated single photon counting technique (TCSPC), of cross-linked colloidal PbS QDot solutions have been performed

and will be shown in this master thesis.

Along with the experimental results, a study of statistical moments of the PbS quantum dot photoluminescence kinetics will be presented in this thesis, which experimental kinetics were acquired with TCSPC. With this statistical analysis, it is possible to evaluate and compare various decay properties, such as the average decay time, the mean-squared value of the decay and the measure of asymmetry of the time-resolved distribution. In order to understand the obtained results, some donor decay models were developed and studied, alongside with other decay functions found in the literature. A theoretical description of the FRET mechanism will be presented in order to understand the proposed decay models.

Keywords: Quantum dot (QDot, or QD), Förster resonant energy transfer (FRET), Lead Sulphide (PbS)

CONTENTS

1	INTRODUCTION	1
1.1	Semiconductor quantum dots (QDots)	1
1.1.1	Colloidal quantum dots	4
1.2	Size-dependent properties of colloidal PbS quantum dots	5
1.3	Förster resonance energy transfer: main concepts	6
1.4	Objectives of this work and outline of this thesis	9
2	THEORETICAL BACKGROUND	13
2.1	Effective mass approximation for electron and hole energy levels	13
2.1.1	Coulomb exciton interaction: Weak and strong confinement	17
2.2	Spontaneous emission and photoluminescence in two-level quantum systems	20
2.2.1	Local density of states (LDOS)	24
2.3	Dipole-dipole resonance interaction between two quantum dots	25
2.3.1	Energy transfer matrix element	27
2.3.2	Transfer rate	29
2.4	FRET rate and the Förster radius in Dexter's theory	30
2.4.1	Derivation of the Dexter expression for the Förster radius	31
2.5	FRET in 3-dimensional QDot ensembles	38
2.5.1	Homogeneous Distribution	40
2.5.2	"Fixed-shell" Distribution	41
2.6	Photoluminescence decay in QDots	42
2.6.1	Decay time in fluorophores	42
2.6.2	Decay models	43
2.6.3	Non-exponential decay in QDots	45
3	MAIN TECHNIQUES AND EXPERIMENTAL PROCEDURE	47
3.1	Time-Correlated Single Photon Counting (TCSPC)	47
3.1.1	Convolution integral	49
3.1.2	Working with near-infrared lasers on quantum dot samples	50
3.2	Optical table setup for TCSPC and emission spectrum studies	51
3.3	Binding of quantum dots via molecular linkers	53
3.3.1	Interacting molecules	54

3.3.2	Covalent binding with carboxyl functionality: EDC/NHS coupling	55
3.3.3	Chemistry procedure: Inter-particle linking of lead sulfide (PbS) quantum dots via EDC/NHS chemistry	56
4	EXPERIMENTAL RESULTS AND DISCUSSION	59
4.1	Emission spectra	60
4.2	Time-resolved decay: data fitting with theoretical decay functions	65
4.2.1	Log-normal distribution of decay rates function	67
4.2.2	Homogeneous acceptor distribution decay function	70
5	STATISTICAL MOMENTS OF QUANTUM DOTS IN PHOTOLUMINESCENCE KINETICS	75
5.1	Statistical moments of theoretical decay functions	75
5.1.1	Single exponential function	76
5.1.2	Homogeneous distribution decay function	77
5.1.3	Fixed-Shell distribution decay function	79
5.1.4	Log-normal distribution decay function	80
5.2	Study of statistical moments of experimental data sets	85
5.3	Discussion of the statistical moments analysis' results	86
5.3.1	Best fit distribution	86
5.3.2	Determining the experimental Förster radius and the average donor-acceptor distance	90
6	CONCLUSION	97
	Appendices	101
A	DERIVATION OF SOME THEORETICAL RELATIONS USED IN THE THESIS	103
A.1	Description of electric field normal modes in terms of Green function dyadics	103
A.2	Energy transfer matrix element derivation	107
A.3	Average of the energy transfer matrix element	111
B	CALCULATIONS FROM EXPERIMENTAL DATA	115
B.1	Calculation of the acceptor concentration and the average QDot size in colloidal QDot sample "Only B"	115
C	COMPUTATIONAL WORK	119
C.1	Matlab code for fitting photoluminescence kinetics	119
C.2	Numerical integration of experimental data	124
C.3	Statistical moment calculation of experimental data	125

LIST OF FIGURES

- Figure 1 Schematic illustration of the changes in the density of states (DOS) of the conduction band with increasing number of dimensions of carrier confinement. Schematic figure adapted from figure of reference [1]. 2
- Figure 2 Schematic representation of the exciton states of CdSe nanocrystals involved in the Stokes shift. Figure obtained from reference [2]. 3
- Figure 3 On top: variation of emitted colour with increased crystalite size of CdSe colloidal QDots, when excited with a near-ultraviolet lamp. On the bottom: Photoluminescence spectra of different sized QDots. As on the top figure, when bigger the QDot, the bigger is the peak emission wavelength. Figure obtained from reference [3]. 3
- Figure 4 Stages of monodisperse colloidal quantum dot synthesis, from initial nucleation to particle growth stages. Figure obtained from reference [4]. 4
- Figure 5 Jablonski diagram of the Förster Resonance Energy Transfer (FRET) between a donor and acceptor molecules. The black lines indicate the transfer of virtual photons, which are intermediate quantum mechanical states which describe the interaction of the entangled donor-acceptor system [5]. Figure reproduced from reference [6]. 7
- Figure 6 Effect of FRET on the emission spectrum of PbS colloidal quantum dots. The legend indicates the concentration of chemical linker, the ion Zn^{2+} , that binds quantum dots at nanometre distance. The higher the Zn^{2+} concentration the more redshifted is the emission spectra. This is an evidence of the FRET mechanism between quantum dots. Figure obtained from reference [7]. 9

- Figure 7 Ground state exciton energy, ΔE_{GS} , as function of QDot diameter, $d = 2R$, for PbS QDots, as calculated with effective mass approximation (EMA) theory, compared with the empirical sizing curve presented by Moreels et al, in reference [8]. 20
- Figure 8 Transition from a initial state to a set of final states. Figure taken from reference [9]. 21
- Figure 9 Excitonic picture of the donor-acceptor quantum system. The horizontal arrow shows the direction of the exciton transfer. There can be a distribution of allowed final exciton states. 26
- Figure 10 Electronic picture for the FRET mechanism in Dexter's formulation. The horizontal arrows describe the direction of electron transfer. The states are broadened due to molecule interactions with the surrounding medium. It is assumed the same state broadening of the excited ($\Delta\omega'$) and ground ($\Delta\omega$) states for the donor and acceptor. 32
- Figure 11 General principle of the Time-Correlated Single Photon Counting technique (TCSPC). Image obtained from reference [10]. 48
- Figure 12 Operation principle of a time-to-amplitude converter (TAC). Image obtained from reference [11]. 49
- Figure 13 Convolution of an instrument response function $L(t_k)$ with the sample's response signature $I(t)$ to yield the measured data $N(t_k)$. Figure obtained from reference [12]. 50
- Figure 14 Scheme of the setup for Time Correlated Single Photon Counting (TCSPC) experiments. [13] 53
- Figure 15 The molecular structure of Glutathione. Figure adapted from reference [14]. 54
- Figure 16 Cross-linker molecules: **a)** 1-Ethyl-3-(3-dimethylaminopropyl) carbodiimide (EDC), and **b)** N-Hydroxysuccinimide (NHS). Figures obtained from references [15, 16]. 55
- Figure 17 Emission spectra in function of wavenumber, $\tilde{\nu}$, i.e, frequency divided by the speed of light (translated into wavelength, λ , in the top line) of the PbS quantum dot samples studied: **a)** Sample A, **b)** Sample B, **c)** Sample C. 61
- Figure 18 Emission spectra of B+B sample collected at different times Δt after the start of the cross-linking chemistry: a) $\Delta t = [13, 80]$ minutes b) $\Delta t = [80, 900]$ minutes. 63

- Figure 19 Overlap of B+B Spectra with Sample B with no cross-linking (Only B). 64
- Figure 20 Peak of B+B sample versus time Δt after the start of the cross-linking chemistry. The dashed red lines correspond to the position of the emission peak measured for sample B with no cross-linking - Only B (See Figure 19), including upper and lower error. 65
- Figure 21 Comparison between experimental photoluminescence kinetics from: **a)** Sample Only B (with no cross-linker), and **b)** Sample B+B (with cross-linker). The y axis, representing the number of single photon counts per bin, is set in the logarithmic scale. Both kinetics were detected at the light wavenumber $\tilde{\nu} = 8333 \text{ cm}^{-1}$. 66
- Figure 22 Time correlated measurements of sample B+B for two different wavenumbers: **a)** $\tilde{\nu} = 8333 \text{ cm}^{-1}$ ($\lambda = 1200\text{nm}$) ($\chi^2 \approx 1.04$), **b)** $\tilde{\nu} = 9091 \text{ cm}^{-1}$ ($\lambda = 1100\text{nm}$) ($\chi^2 \approx 1.02$) . Log-normal distributions are fitted with red lines. 68
- Figure 23 Results from the fitting of the log-normal distribution decay function in kinetics of sample B+B, in function of light wavenumber $\tilde{\nu}$ for three different QDot aggregation stages Δt : **a)** Most frequent decay rate, Γ_{mf} . Here it is compared the behaviour of sample B+B with the sample Only B (in purple); **b)** Measured FRET decay rate, Γ_{FRET} ; **c)** Measured efficiency of FRET, η_{FRET} . The grey horizontal dashed lines indicate the upper and lower bounds of η_{FRET} . 69
- Figure 24 Time correlated measurements of sample B+B for two different wavenumbers: **a)** $\tilde{\nu} = 8333 \text{ cm}^{-1}$ ($\lambda = 1200\text{nm}$) ($\chi^2 \approx 1.03$), **b)** $\tilde{\nu} = 9091 \text{ cm}^{-1}$ ($\lambda = 1100\text{nm}$) . Homogeneous distribution decay functions are fitted with red lines. A graph of the residuals of the data fit is shown. 73

- Figure 25 Results from the fitting of the homogenous acceptor distribution decay function in kinetics of sample B+B, in function of light wavenumber $\tilde{\nu}$ for three different QDot aggregation stages Δt : **a)** Most frequent decay rate, Γ_{mf} . Here it is compared the behaviour of sample B+B with the sample Only B (in purple); **b)** Number of acceptor QDots N_0 , inside a sphere of radius R_0 ; **c)** Measured FRET decay rate, Γ_{FRET} ; **d)** Measured efficiency of FRET, η_{FRET} . The grey horizontal dashed lines indicate the upper and lower bounds of η_{FRET} . 74
- Figure 26 Ratio of moments R_n for the single exponential function. 77
- Figure 27 Ratio of moments R_n , with varying number of acceptors N_0 inside a sphere of Förster radius R_0 , for two theoretical acceptor distributions: the homogeneous and fixed-shell ones. 81
- Figure 28 Variation of the ratio of moments R_2 in function of the parameter α , with $N_0 = 1$ and $\Gamma = 2\mu s^{-1}$. 82
- Figure 29 Ratio of moments R_n for the fixed-shell distribution decay function, for values of α in the range $\alpha \in [0.80, 1.20]$ 83
- Figure 30 Ratio of moments R_n for the log-normal distribution decay function, for different values of the width parameter ω . 85
- Figure 31 Emission spectra for the two samples studied - Only B and B+B - as shown in the previous chapter. Here the four arrows mark four different regions of the spectra for which statistical moments were calculated. 86
- Figure 32 Calculated R_n for four different emission wavelengths: **a)** 1140 nm, **b)** 1160 nm, **c)** 1200 nm and **d)** 1240 nm. Error bars, though proportionally small to the values of R_n , are presented in each dot. In figure b), for $n \in [6, 8]$ the red curve presents negative values, which are not presented in the plot. 89
- Figure 33 Experimental results for the ratio R_n for $\lambda = 1240\text{nm}$. In the top right corner some R_n functions based on theoretical decay functions are presented. 90
- Figure 34 Comparison of data curve obtained from experimental results with theoretical decay models. 91

- Figure 35 2-dimensional schematic of a QDot spherical cluster, with radius a_c . In the centre of the sphere, in an orange circle, lies the donor QDot and, surrounding this donor, in vivid red circles, are presented several acceptor QDots. 94
- Figure 36 Schematic for the orientation of the transition dipole moments \mathbf{d}_A and \mathbf{d}_D in relation to the donor-acceptor distance vector \mathbf{R} , aligned with the z axis. 112
- Figure 37 Estimation of the full width at half maximum an peak centre of the spectrum of the PbS sample Only B. 116
- Figure 38 Comparison of results for the ratio R_n of an experimental decay curve for two types of numerical integration: trapezoidal rule (in red) and Simpson's rule (in blue). The use of the Simpson rule for higher moments n shows a clear advantage to the use of the trapezoidal rule, since it increases the accuracy of the numerical integration. 126

INTRODUCTION

1.1 SEMICONDUCTOR QUANTUM DOTS (QDOTS)

Quantum Dots (QDots or QDs, in abbreviation) are small semiconductor crystallites, on the nanometre scale, which have properties intermediate between bulk semiconductors and discrete atoms or molecules. QDots are often referred to as artificial atoms, emphasizing their singularity, having bound, discrete electronic states, even though they consist of many (around 10^3) atoms [17, 18, 19]. These effects arrive from carrier confinement in all three dimensions, which drastically changes the electronic density of states (DOS) near the band-edges, by confining electrons or holes, or both. Figure 1 shows the effect of quantum confinement in different structures, from bulk (3 dimensions), quantum well (2 dimensions), quantum wire (1 dimension) and quantum dot (0 dimension). A three-dimensional confinement, which leads to zero-dimensional structures, restrains the electronic DOS for bulk semiconductors into Dirac-delta type of peaks¹, comparable to what is predicted for isolated atoms. Carrier confinement also produces an increase on the band-gap energy. This increase of energy is inversely proportional to the size of the QDot, i.e., the smaller the QDot the higher the band-gap energy. The effective band-gap energy depends on factors such as size, shape, materials and impurities of the QDots.

Due to the discrete electronic states, these semiconductor nano-particles show a distinctive peaked emission spectra. The peak emission wavelength increases with increasing QDot average size. In Figure 3 this trend is found on emission spectra of different sized CdSe QDot samples. The width of the transmission spectra arises from QDot size dispersion on fabricated samples with the know techniques.

The effects of size quantization appear when the carrier motion is limited in a layer of the thickness of the order of the carriers' de Broglie wavelength, which wavelength depends on the effective mass of the carrier and on the temperature [20]. The exciton

¹ Note that, in real quantum dots, the size distribution leads to a broadening of this line function.

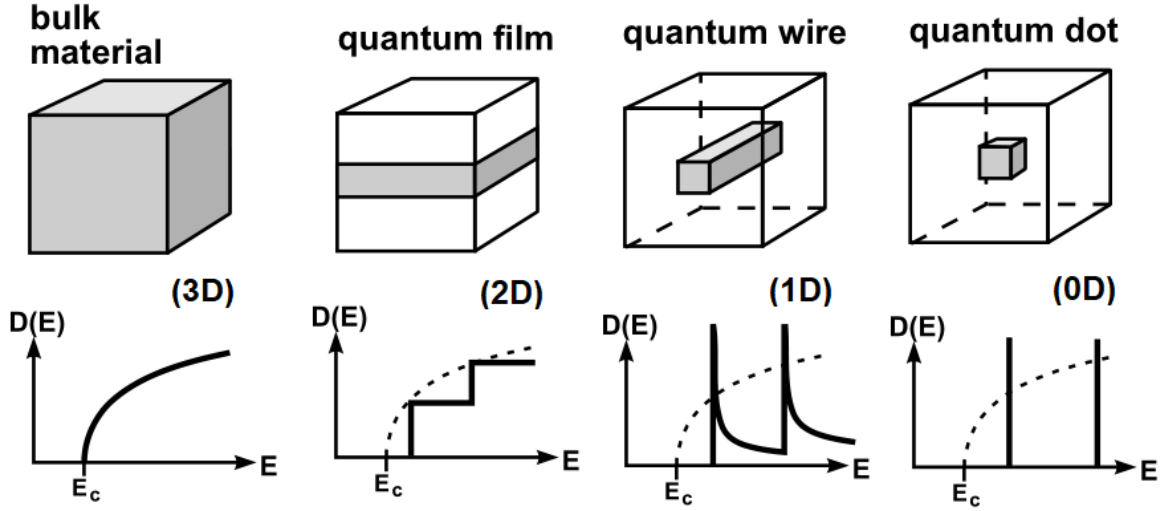


Figure 1: Schematic illustration of the changes in the density of states (DOS) of the conduction band with increasing number of dimensions of carrier confinement. Schematic figure adapted from figure of reference [1].

Bohr radius r_B , defined as the distance between the electron and a hole², sets a threshold for carrier confinement. It is defined as:

$$r_B \equiv \frac{\hbar^2 \varepsilon}{e^2} \left(\frac{1}{m_e^*} + \frac{1}{m_h^*} \right), \quad (1.1)$$

where ε , \hbar , and e are the static dielectric constant, reduced Planck's constant and the charge of an electron, respectively, and m_e^* and m_h^* are the electron's and hole's effective masses, which differ between different materials. If the dimension of the QDot, R , approaches r_B , i.e., $R \approx r_B$, or if $R < r_B$, the motion of the electrons and holes is strongly spatially confined to the dimension of the QDot [18]. For $R > r_B$ one has the weak confinement regime, where the electron-hole Coulomb interaction is predominant.

Semiconductor QDots have the property of presenting an energy shift between the absorption spectrum and the emission spectrum. This shift is called the Stokes shift, and it is an effect where the peak of the emission band lies at a smaller energy than the lowest maximum of the absorption band. In most cases it is caused mainly by the size distribution in the measured ensemble of QDots. However, a smaller Stokes shift is also present for individual dots, which comes from the particular structure of

² Exciton stands for the electron-hole pair, produced when an electron from the valence band is excited to the conduction band and leaves a *hole* in the valence band, considered as a positive charged particle.

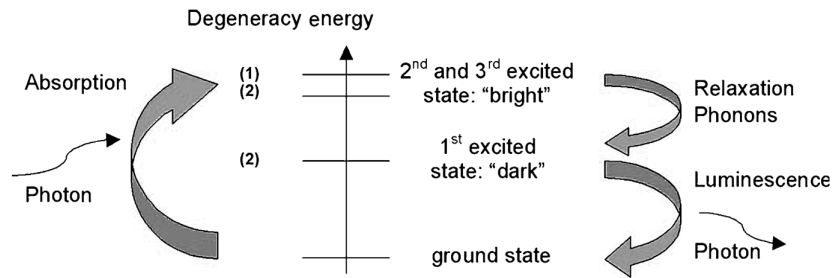


Figure 2: Schematic representation of the exciton states of CdSe nanocrystals involved in the Stokes shift. Figure obtained from reference [2].

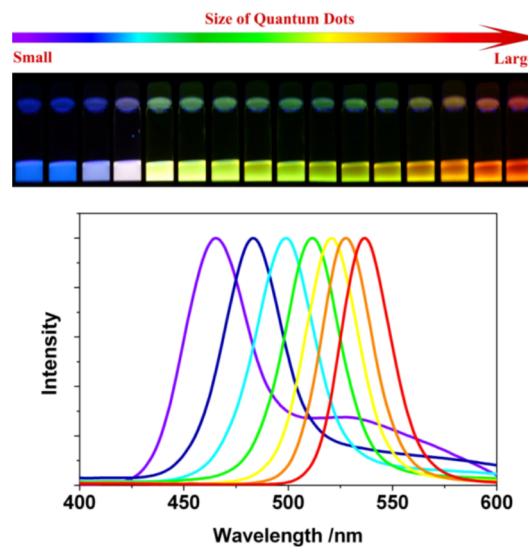


Figure 3: On top: variation of emitted colour with increased crystalite size of CdSe colloidal QDots, when excited with a near-ultraviolet lamp. On the bottom: Photoluminescence spectra of different sized QDots. As on the top figure, when bigger the QDot, the bigger is the peak emission wavelength. Figure obtained from reference [3].

the exciton energy levels inside the nanocrystal QDot [2]. The fine structure of the excited state consists in several degenerate states, whose degeneracy is lifted due to a symmetry reduction as, for instance, non-spherical shape of the dot or hexagonal structure of the underlying material. Figure 2 presents these states for CdSe QDots. Some states, called "bright", of higher energy, are optically allowed states to which electrons are excited, while another state, called "dark", of lower energy, is optically inactive because of symmetry-dictated selection rules. Relaxation occurs via phonon emission from bright states to the dark state and radiative recombination occurs, yielding a lower energy photon. This energy difference is of the order of 10-15 meV in isolated QDots.

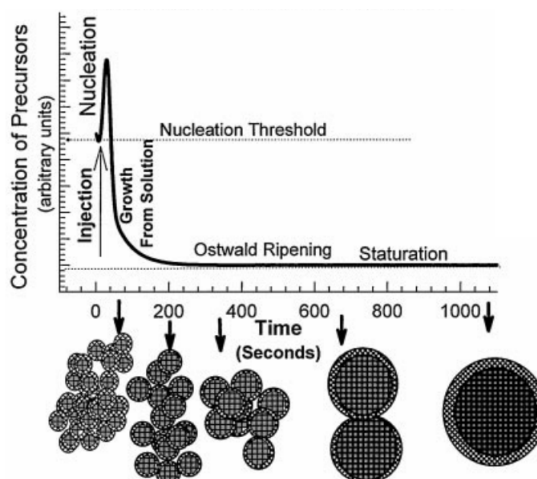


Figure 4: Stages of monodisperse colloidal quantum dot synthesis, from initial nucleation to particle growth stages. Figure obtained from reference [4].

1.1.1 Colloidal quantum dots

Colloidal QDots are semiconductor nanocrystallites that are suspended throughout a liquid substance, obtained from the chemical process of precipitation of a solid phase from a solution. The fabrication of colloidal QDots relies on two main steps: nucleation and particle growth stages [4, 21, 22]. Figure 4 presents these precipitation stages. The nucleation stage starts when the solution is supersaturated with precursors, i.e., the semiconductor particles. In this stage, stable self-organized nuclei are formed due to the instability of the supersaturated solution. The uniformity of size distribution of these nanocrystals is obtained by a short nucleation period. As nucleation reduces the solution's saturation by molecular addition, the nucleation process stops when the concentration drops below the critical level of the solution's solubility, and particles proceed growing by molecular addition until the equilibrium concentration of the precipitated crystallites is reached. If the chemical reaction is not stopped, the size of the crystals can extend into the micrometre regime on the saturated stage [4]. During the particle growth stage, there is a stage when there is a broad size distribution, named Ostwald ripening or defocusing [22]. If the reaction is stopped at this stage, there will be two size regimes, a bigger one and a smaller one.

In order to finally produce stable nanoparticles, the produced crystallites are surrounded during the reaction by adding organic ligands or inorganic capping materials. The use of organic ligands to stabilize the nanoparticles comes from the diverse use of colloidal quantum dots in biomedical applications [23, 24]. The systematic adjustment of the reaction parameters, such as the reaction time, temperature, concentration, and

the selection of the reagents and surfactants are used to control the size, shape and quality of the colloidal QDots.

1.2 SIZE-DEPENDENT PROPERTIES OF COLLOIDAL PBS QUANTUM DOTS

Lead Sulfide (PbS) is an inorganic compound, appears in nature as the mineral Galena, and it is a natural group IV-VI semiconductor [25]. Bulk PbS has a direct band gap of 0.41 eV at 300K, it has a rock-salt structure, with lattice constant $a = 5.936 \text{ \AA}$ [8], and has a large exciton Bohr radius of 18 nm [8, 26, 27]. Due to such a large Bohr radius, colloidal QDots of PbS are characterized by the strong confinement regime [8, 28], and can be produced with a band gap in the Near-Infrared (NIR) spectral range [8]. PbS nanocrystals have an electron effective mass, m_e^* equal to the hole effective mass, m_h^* , with the value of $0.085m_0$, where m_0 is the electron rest mass [29]. PbS QDots have been estimated to have a static dielectric constant $\epsilon_0 = 14.5 \pm 1.8$ [30]. Colloidal PbS quantum dots can be controlled to absorb light in the range of 600-3000 nm [31]. These QDots maintain their rock-salt crystal structure even when the size is decreased from bulk down to the nanoscale [8, 32, 33].

In the work by Moreels et al [8], colloidal PbS quantum dots are shown to be non-stoichiometric, with an excess of Pb over Sulphur ion, S^{-2} . With Rutherford backscattering spectrometry experiments, the ratio of Lead and Sulphur Pb/S has been found to vary between 1.23 and 1.37. The work presents as well an experimental sizing curve of the QDots by correlating the band gap E_0 with the QDot size d as

$$E_0 = 0.41 + \frac{1}{0.0252 d^2 + 0.283 d} \quad (1.2)$$

where the size range was $3.9 < d < 13.3$ nm. The experimental sizing curve agrees well with tight-binding calculations [32]. The molar extinction coefficient of a colloidal solution of PbS QDots, ϵ , scales with the QDot volume and the molar extinction coefficient at the band gap was found to scale as $d^{1.3}$ [8].

For a semiconductor QDot, the temperature dependence of the energy band gap is proportional to the size of the nanocrystallite. For PbS QDots the same trend is found, where, for bigger PbS QDots, around 16 nm, $\partial E_0 / \partial T$ approaches the bulk PbS semiconductor value ($\sim 500 \mu\text{eV}/\text{T}$), and for smaller 2 nm to 4 nm sized QDots the temperature dependence is nearly zero [34].

The Stokes shift on PbS QDots has been reported by Liu et al and Voznyy et al to reach energy shifts of around 200 meV, which is considerably greater than, e.g, CdSe

QDots [35, 36]. The main arguments presented by the authors to understand this shift are QDot defects and QDot aggregation.

Walsh et al [37] has shown the theoretical effect of the elongation of PbS QDots on its electronic and optical properties. Using the $\mathbf{k} \cdot \mathbf{p}$ method with the rock-salt crystal structure [38], Walsh et al shown that the elongation of a spherical PbS QDot along the longitudinal (z) and/or the transverse (x or y) directions yields a lower band gap. Due to the incremental change in the confinement volume, the geometrical symmetry breaking increases the number of optically allowed transitions and moves the absorption cross section peaks to lower energies.

PbSe QDots, another well known lead chalcogenide, present similar properties to PbS QDots, regarding crystal structure, but a slightly smaller bulk band gap energy of 0.28 eV and a larger Bohr radius of 46 nm, where the latter property gives stronger quantum confinement effects [13, 34, 38, 39]. Both types of QDots can achieve stronger quantum confinement³ than the most common CdSe QDots and other II-VI and III-V semiconductor materials [34]. PbSe QDots show similar QDot size dependence to the band gap E_0 as found with PbS QDot, although PbS QDots are typically larger than PbSe QDots for a given E_0 [8, 39]. Due to their similar properties and sharp emission spectra in the near-infrared spectral range, PbS and PbSe QDots are of great interest for studies of nanophotonic control over spontaneous emission of light in strongly interacting silicon photonic crystal structures [40, 41, 42, 43].

PbS QDots have been applied in photovoltaics due to low energy band gap, high absorption coefficient $1 - 5 \times 10^5 \text{cm}^{-1}$ and large exciton Bohr radius [31, 44, 45]. Other known applications are in bioanalysis [46], photonic crystals [40, 41, 42, 43] and lasers [47]. Together with other lead chalcogenides, they are amongst the most promising materials for quantum emitters in the infrared spectral range [34, 48].

1.3 FÖRSTER RESONANCE ENERGY TRANSFER: MAIN CONCEPTS

The FRET mechanism, short for Förster resonance energy transfer or fluorescence resonance energy transfer, is a mechanism which describes non radiative energy transport between two quantum dots, or fluorescence molecules. It was first theoretically described by Förster in 1948 [49], and still forms the basis of most of the work in the domain of nonradiative energy transfer. This mechanism involves an excited donor

³ Strong quantum confinement effects occur when the QDot radius, R , is much smaller the the exciton Bohr radius, a_B . In lead chalcogenide QDots the ratio (R/a_B) can reach small values around 0.02, whereas, e.g. in CdSe QDots the minimum possible value is around 0.16 [34].

fluorophore (e.g., a quantum dot or a dye molecule) which transfers its energy of excitation to an acceptor fluorophore via dipole-dipole coupling, i.e., by dipole-dipole resonance. In a quantum mechanical description, the energy transfer is mediated by virtual photons, i.e., intermediate quantum mechanical states which describe the interaction of the entangled donor-acceptor system [5]⁴. FRET is one of the main types of energy transfer between emitters at a nanometre proximity. It can also act as a mechanism of non-radiative de-excitation of a QDot if the energy is transferred to a dissipative environment [50].

Figure 5 shows a Jablonski diagram, i.e., a diagram of molecular electronic states, in case of a FRET mechanism. At first, the donor molecule is excited to a higher energy level S_1 ⁵. Typical relaxation to the state of least vibrational energy occurs, with a decay rate of the order of picoseconds [51]. The non-radiative FRET mechanism mediates the donor electron's excited energy into the acceptor molecule, which excites the acceptor into its excited level, and then finally decays into the ground state. Thus, FRET introduces a new decay channel for the excited state, which, without FRET, predominantly decays via the donor radiative mechanism (displayed in green in Figure 5).

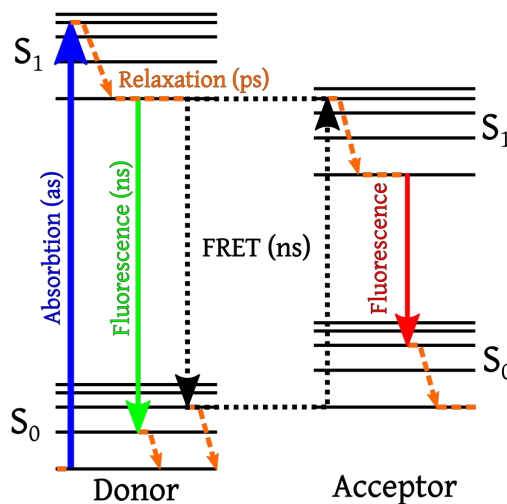


Figure 5: Jablonski diagram of the Förster Resonance Energy Transfer (FRET) between a donor and acceptor molecules. The black lines indicate the transfer of virtual photons, which are intermediate quantum mechanical states which describe the interaction of the entangled donor-acceptor system [5]. Figure reproduced from reference [6].

⁴ Detailed consideration of the dipole-dipole resonance interaction for quantum dots, in a quantum-mechanical description, is found in Chapter 2.3.

⁵ In a Jablonski diagram, the energy levels, namely S_0 and S_1 , are arranged vertically and divided into multiple vibrational energy levels. See reference [51] for further explanation.

As previously mentioned, adding a acceptor into the donor's environment introduces FRET as a new energy decay channel to the fluorescent system. Therefore, the total decay rate, Γ_{DA} , of a FRET coupled donor is $\Gamma_{DA} = \Gamma_D + \Gamma_{FRET}$, where Γ_D is the total decay rate of an isolated donor. Since the latter is the sum of the radiative rate Γ_{rad} and the non-radiative rate Γ_{nr} , $\Gamma_D = \Gamma_{rad} + \Gamma_{nr}$, the FRET efficiency, η_{FRET} , can be written as follows:

$$\eta_{FRET} \equiv \frac{\Gamma_{FRET}}{\Gamma_{FRET} + \Gamma_{rad} + \Gamma_{nr}} = 1 - \frac{\Gamma_D}{\Gamma_{DA}} \quad (1.3)$$

By measuring the decay rates Γ_{DA} and Γ_D one can find evidence of the presence of FRET by studying its efficiency η_{FRET} . The donor-acceptor decay rate Γ_{DA} should be higher or equal comparing with the isolated donor decay rate Γ_D , in order to yield efficiencies below or equal to one. The decay rate values can be determined with a statistical study of the arrival time of emitted photons from excited quantum dot samples, such as the Time-Correlated Single Photon Counting (TCSPC) technique (See chapter 3.1).

The rate of energy transfer, Γ_{FRET} , from a specific donor to a specific acceptor, in the strong confinement regime, is given by

$$\Gamma_{FRET} = \frac{1}{\tau_D} \left(\frac{R_0}{R} \right)^6, \quad (1.4)$$

where R_0 is the Förster distance, i.e. the distance between donor and acceptor where the efficiency is 50%, i.e, where the transfer rate equals the rate of emission, $\tau_D = 1/\Gamma_D$ is the lifetime of the donor in absence of the acceptor and R is the distance between the two entities [12, 49, 52]. The mechanism's efficiency depends on the inverse 6th-power law of the distance R , due to the dipole-dipole interaction of these particles.

FRET strongly depends on three main parameters, which are the following:

1. Distance R between donor and acceptor;
2. Spectral overlap of the donor emission spectrum and the acceptor absorption spectrum;
3. The relative orientation of the transition dipole moment of the donor and the acceptor.

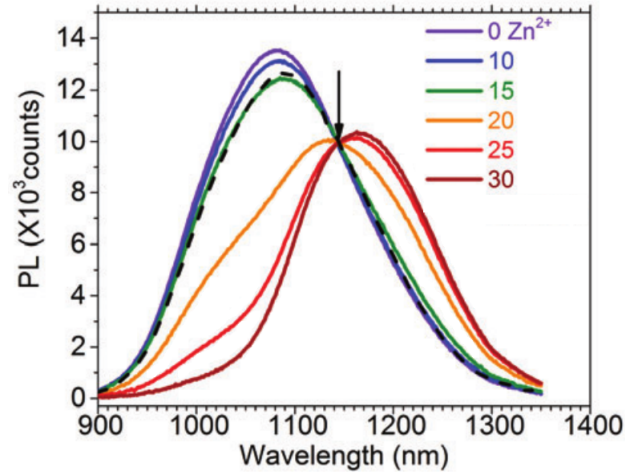


Figure 6: Effect of FRET on the emission spectrum of PbS colloidal quantum dots. The legend indicates the concentration of chemical linker, the ion Zn^{2+} , that binds quantum dots at nanometre distance. The higher the Zn^{2+} concentration the more redshifted is the emission spectra. This is an evidence of the FRET mechanism between quantum dots. Figure obtained from reference [7].

Since, in quantum dots, the emission spectrum is redshifted in comparison with the absorption spectrum (the Stokes shift), the optimal spectral overlap occurs when the donor quantum dots are smaller (i.e, higher band-gap energy) than the acceptor quantum dots (i.e, lower band-gap energy). This condition yields higher FRET mechanism efficiency and, in a emission spectrum, the energy transfer translates into a redshift of the emission peak, comparing with QDots with no FRET mechanism. In Figure 6 this effect is found on PbS colloidal quantum dots, by increasing the concentration of a chemical linker that binds QDots together at nanometre distance [7].

One possible application of the FRET mechanism in quantum dots is to create a quantum information system, by embedding the quantum dots in a photonic bandgap crystal. The photonic bandgap crystal, such as a inverse woodpile photonic crystal [13, 53, 54], inhibits the radiative decay of quantum dots, thus increasing the efficiency of the FRET mechanism.

1.4 OBJECTIVES OF THIS WORK AND OUTLINE OF THIS THESIS

The main objective of this work was to detect the presence of the FRET mechanism in ensemble of colloidal PbS quantum dots, where the quantum dots act as both

the donor and acceptor entities. Experimental techniques, such as emission spectra acquirement and Time-Correlated Single Photon Counting (TCSPC), were used to study photoluminescence properties of the QDot samples. By introducing a chemical linker, namely using the EDC/NHS surface chemistry⁶, the QDots were binded at a fixed length, at a nanometre distance. This binding allows to detect changes on the emission and decay properties of the QDot samples, which can be related with the appearance of new energy decay mechanism, such as the FRET mechanism. In order to further understand the experimental results, theoretical studies were performed, followed by an analysis of the statistical moments of some empirical and derived decay functions.

The use of colloidal PbS QDots leads to the study of FRET in QDots emitting in the near-infrared (NIR) part of the light's spectrum. Most studies of FRET mechanisms in colloidal QDot systems use QDots emitting in the visible light spectrum.

Similar experimental techniques were used by Wang et al [7], where the authors reported signals of the presence of energy transfer. According to them, it occurred by multi-step hopping of near-infrared excitons, within aggregates of PbS QDots capped with glutathione and aggregated using Zn^{+2} cations. A redshift of the samples' emission and absorption spectra with increase of the concentration of Zn^{+2} cations shown the increasing efficiency of the FRET mechanism, since it can be an evidence of energy transfer from a larger gap (smaller sized) QDot to a smaller gap (larger sized) one.

Experimental results obtained in the framework of this thesis, after a careful statistical analysis performed, also demonstrate that the FRET mechanism was present in the samples. Such results give an insight of some expected photoluminescence results of PbS QDot aggregations.

The thesis is consisted by this introduction (Chapter 1) and five chapters, with appendices.

In Chapter 2 a theoretical background is presented for the study of FRET in semiconductor PbS quantum dots. Here are presented studies of the band gap energy of confined excitons (Chapter 2.1), the study of spontaneous emission in two-level quantum systems (Chapter 2.2), studies of the FRET mechanism, in a quantum electro-

⁶ The molecules EDC (1- Ethyl- 3- (3- dimethylaminopropyl) carbodiimide) and NHS (N-Hydroxysulfosuccinimide) were the cross-linker molecules used to bind the PbS QDots. See Chapter 3.3 for further insight.

dynamics description, between two model quantum dots (Chapter 2.3), the derivation of the Förster radius (Chapter 2.4), the derivation of decay functions for 3-dimensional QDot ensembles (Chapter 2.5) and a brief review of theoretical approaches to study photoluminescence decay in QDots, including empirical decay functions, found in the literature (Chapter 2.6).

In Chapter 3 the main experimental techniques and the experimental procedure are introduced, used to develop the study of cross-linked ensembles of PbS QDots. It is presented a description of the TCSPC technique (Chapter 3.1), along with the experimental setup over an optical table (Chapter 3.2). Brief studies of the technique of surface chemistry and the main interacting molecules for cross-link of QDots are also present, including the chemistry procedure used for creating colloidal PbS QDot aggregates (Chapter 3.3).

In Chapter 4 the main experimental results of this thesis are presented. Emission spectra and time resolved photoluminescence measurements of cross-linked PbS QDot samples and non-cross-linked ones are compared in order to detect evidences of FRET due to the agglomeration of QDots. Data fitting time resolved measurements, with empirical and derived decay functions is achieved in this chapter, finding possible evidences of FRET for the studied samples, albeit the obtained results hold interpretation struggles.

In Chapter 5 a study is developed of the statistical moments of the photoluminescence kinetics of the PbS QDot samples. Firstly, the statistical moments of empirical and derived decay functions are studied (Chapter 5.1) and they are afterwards compared with the statistical moments obtained from the data treatment of the studied PbS QDot samples (Chapter 5.3). From the obtained results, evidences of FRET have been found in the studied samples and an estimate of the Förster radius and the average QDot agglomerate size is here presented.

In Chapter 6 a conclusion over the content of this thesis is presented, including the summary of the main achievements of this work, as well as suggestions for improving the viability of the experimental results for the further development of studying FRET in colloidal QDot ensembles.

THEORETICAL BACKGROUND

2.1 EFFECTIVE MASS APPROXIMATION FOR ELECTRON AND HOLE ENERGY LEVELS

To describe the electronic spectrum of a quantum dot (QDot), let us assume a spherical QDot with radius R . To a first approximation, the QDot's involving material creates an infinite height potential for both confined electrons and holes of the QDot. Such an approximation is only valid if the surrounding medium has a band gap energy much higher than the semiconductor QDot [19, 55, 56]. This approximation is valid for colloidal PbS QDots in water ¹. If considering, for instance, QDots embedded in a crystal, one must take into account a finite potential V_0 , for which analytical solutions are difficult to produce. Nanda et al [55, 28] has developed a model for a finite potential square-well model, which applied to determine the band-gap of PbS and CuBr nanoparticles. On a more general study, many mathematical models, within the effective mass and nonparabolic band theory ², were developed in order to find, using numerical approximations, the electronic structure of semiconductor QDots [58].

In this chapter a study is presented of the ground state (i.e, $l = 0, m = 0$) of the electronic spectrum of a 0D semiconductor for an infinite barrier potential. By calculating the ground state eigenvalues one evaluates the size-dependent band gap of the QDot. One finds, as well, to a first approximation, the effect of the Coulomb interaction between electrons and holes in the QDots.

-
- ¹ The energy band gap of water is calculated as 7.3 eV in room temperature (300K) in the literature [57]. This energy is at least 7 times higher than the band gap of PbS QDots, considering equation 1.2 from reference [8]. Thus, this approximation can be valid for colloidal PbS QDots in water, which means that the QDot wave function extends negligibly outside the QDot.
 - ² Many other approaches, such as tight binding, configuration interaction, density functional theory (DFT), multiband and one band, were developed to study QDot systems. As a guideline, see the references mentioned on the second paragraph of the introduction of reference [58].

Using spherical coordinates, the Schrödinger equation which describes the electron and hole wavefunction inside the spherical infinite potential well is:

$$\left\{ -\frac{\hbar^2}{2m^*} \left[\frac{1}{r^2} \frac{d}{dr} \left(r^2 \frac{d}{dr} \right) \right] + \nabla_{\theta,\phi}^2 \right\} \Psi(r, \theta, \phi) = E \Psi(r, \theta, \phi) \quad (2.1)$$

where m^* is the electron (or hole) effective mass and $\nabla_{\theta,\phi}^2$ is the angular part of the Laplacian, with spherical harmonics eigenfunctions $Y_{lm}(\theta, \phi)$, and with eigenvalues:

$$\nabla_{\theta,\phi}^2 Y_{lm}(\theta, \phi) = -\frac{l(l+1)}{r^2} Y_{lm}(\theta, \phi). \quad (2.2)$$

One assumes that one exciton is produced³. The exciton's electron has an energy $E_e \geq E_c$, where E_c is the bottom value of the conduction band, and the exciton's hole has an energy $E_h \leq E_v$, where E_v is the top value of the valence band. Since one needs to find the ground state energy, one chooses $l = 0$. In this way, the Schrödinger equations for the electron and the hole with wavefunctions Φ_e and Φ_h , respectively, read inside the QDot ($r < R$):

$$-\frac{\hbar^2}{2m_e^*} \left[\frac{1}{r^2} \frac{d}{dr} \left(r^2 \frac{d}{dr} \right) \right] \Phi_e(r) + E_c \Phi_e(r) = E_e \Phi_e(r) \quad (2.3a)$$

$$\Leftrightarrow \frac{d^2}{dr^2} \Phi_e(r) + \frac{2}{r} \frac{d}{dr} \Phi_e(r) + k_e^2 \Phi_e(r) = 0,$$

and

$$-\frac{\hbar^2}{2m_h^*} \left[\frac{1}{r^2} \frac{d}{dr} \left(r^2 \frac{d}{dr} \right) \right] \Phi_h(r) + E_v \Phi_h(r) = E_h \Phi_h(r) \quad (2.3b)$$

$$\Leftrightarrow \frac{d^2}{dr^2} \Phi_h(r) + \frac{2}{r} \frac{d}{dr} \Phi_h(r) - k_h^2 \Phi_h(r) = 0,$$

with

$$\frac{2m_e^* (E_e - E_c)}{\hbar^2} = k_e^2 \text{ and } \frac{2m_h^* (E_v - E_h)}{\hbar^2} = k_h^2; \quad k_e, k_h > 0. \quad (2.4)$$

³ We shall call an electron-hole pair exciton for clarity, even if the electron-hole interaction energy is small compared to the confinement energy. See chapter 2.1.1 for further development.

The ground state solutions to equations 2.3a and 2.3b are the wavefunctions Φ_e and Φ_h , respectively, equal to:

$$\Phi_e(r) = A_e j_0(k_e r_e), \quad (2.5a)$$

$$\Phi_h(r) = A_h j_0(k_h r_h), \quad (2.5b)$$

$$j_0(kr) \equiv \frac{\sin(kr)}{kr},$$

where j_0 is the spherical Bessel function of first kind and A_e and A_h are the respective normalization constants. In this model it is assumed that $A_e = A_h = A$.

At the boundary of the QDot, i.e, $r = R$, the wavefunctions must vanish, due to the infinite barrier at the QDot's radius:

$$\Phi_e(R) = \Phi_h(R) = 0 \quad (2.6a)$$

using the definition of the Bessel function j_0 :

$$\Leftrightarrow \frac{\sin(k_e R)}{k_e R} = 0 \wedge \frac{\sin(k_h R)}{k_h R} = 0 \quad (2.6b)$$

Thus,

$$\Leftrightarrow k_e = \frac{n_e \pi}{R} \wedge k_h = \frac{n_h \pi}{R}, \quad (2.6c)$$

where $n_{e,h} = 1, 2, \dots$. Since the ground state is to be studied, then $n_e = n_h = 1$, since it yields the lower energy state. Thus we have, in the ground state, that

$$k = k_e = k_h = \frac{\pi}{R} \quad (2.7)$$

The normalization constants of the electron and hole wavefunctions, equations 2.5a and 2.5b, respectively, can be calculated using the result of equation 2.7. The normalization constant is the same for both wavefunctions and yields the following expression:

$$\begin{aligned}
|A|^2 \int_V \frac{\sin^2(kr)}{k^2 r^2} d\mathbf{r} &= 1 \\
\Leftrightarrow |A|^2 \int_0^{2\pi} d\phi \int_0^\pi \sin\theta d\theta \int_0^R \frac{\sin^2(kr)}{k^2} dr &= 1 \\
\Leftrightarrow |A|^2 4\pi \left(\frac{R}{\pi}\right)^3 \int_0^\pi dx \sin^2(x) &= 1 \\
\Leftrightarrow |A| &= \sqrt{\frac{\pi}{2R^3}},
\end{aligned} \tag{2.8}$$

where the variable substitution $x \equiv kr = \frac{\pi}{R}r$ was used. By inserting equation 2.7 into equation 2.4 one obtains the energy E_e of the ground state of the electron to be equal to

$$\begin{aligned}
E_e &= E_c + \frac{\hbar^2 k_e^2}{2m_e^*} = E_c + \frac{\hbar^2 \pi^2}{2m_e^* R^2} \\
\Rightarrow E_e - E_v &= E_g + \frac{\hbar^2 \pi^2}{2m_e^* R^2}
\end{aligned} \tag{2.9a}$$

while, the hole's energy is equal to

$$E_h - E_v = -\frac{\hbar^2 \pi^2}{2m_h^* R^2} \tag{2.9b}$$

This way, we find the ground state energy, $\Delta E_G = E_e - E_h$, for the QDot to be

$$\Delta E_G(R) = E_g + \frac{\hbar^2 \pi^2}{2R^2} \left(\frac{1}{m_e^*} + \frac{1}{m_h^*} \right) + U_C \tag{2.10}$$

where U_C is the exciton Coulomb interaction energy between the electron and the hole, which will be derived in the following subsection.

2.1.1 Coulomb exciton interaction: Weak and strong confinement

The exciton energy spectrum strongly depends on the magnitude of the Coulomb interaction between the electron and the hole, when compared with the typical value of the energy gained by the particles due to their confinement ($\Delta E_e = E_e - E_c$ for the electron and $\Delta E_h = E_h - E_v$ for the hole). The typical energy of the Coulomb exciton interaction between the electron and the hole U_C can be estimated to be [2, 19]

$$U_C = -\zeta \frac{e^2}{\epsilon_1 R}, \quad (2.11)$$

where R is the QDot radius, e is the elementary electric charge, ϵ_1 is the dielectric constant of the QDot and ζ is a coefficient of the order of the unity. By comparing the energy U_C with the electron-hole energy gap $\Delta E = \Delta E_e + \Delta E_h$, one may find two different regimes, namely, the strong and weak confinement regimes. In the strong confinement regime one has that $\Delta E \gg |U_C|$ or, equivalently, $r_B \gg R$, where r_B is the exciton Bohr radius [2, 19]. In this regime, the Coulomb interaction can be considered to be a small perturbation comparing the confinement energy. On the other hand, the weak confinement regime has $\Delta E \ll |U_C|$, or $r_B \ll R$. In this case, the Coulomb interaction is predominant and creates strongly bound excitons.

Most reports regarding PbS quantum dots [8, 26, 59, 60] describe these QDots as belonging to the strong confinement regime. Therefore, a strong confinement description is hereby presented. The Coulomb interaction is considered as a small perturbation. So, to a first approximation, the exciton wavefunction is the product of the independent electron and hole wavefunctions:

$$\Psi(\mathbf{r}_e, \mathbf{r}_h) = \Phi_e(\mathbf{r}_e)\Phi_h(\mathbf{r}_h). \quad (2.12)$$

The Coulomb correction is given, in first order perturbation theory, by the mean value of the Coulomb potential:

$$\begin{aligned} U_C &\simeq \left\langle -\frac{e^2}{\epsilon_1 |\mathbf{r}_e - \mathbf{r}_h|} \right\rangle = -\frac{e^2}{\epsilon_1} \left\langle \frac{1}{|\mathbf{r}_e - \mathbf{r}_h|} \right\rangle \\ &= -\frac{e^2}{\epsilon_1} \int \int |\Phi_e(\mathbf{r}_e)|^2 |\Phi_h(\mathbf{r}_h)|^2 \frac{d\mathbf{r}_e d\mathbf{r}_h}{|\mathbf{r}_e - \mathbf{r}_h|}. \end{aligned} \quad (2.13)$$

The inverse modulus factor in equation 2.13 can be written in terms of Legendre polynomials [61] as

$$\frac{1}{|\mathbf{r}_e - \mathbf{r}_h|} = \begin{cases} \sum_{l=0}^{\infty} \frac{r_h^l}{r_e^{l+1}} P_l(\cos \gamma), & \text{if } r_e < r_h \\ \sum_{l=0}^{\infty} \frac{r_e^l}{r_h^{l+1}} P_l(\cos \gamma), & \text{if } r_e > r_h \end{cases} \quad (2.14)$$

where γ is the angle between \mathbf{r}_e and \mathbf{r}_h and $P_l(\cos \gamma)$ are the Legendre polynomials of order l . Since in this problem we are only interested in studying the wavefunction for the ground state, which is an s-state, if one deals only with s-states in equation 2.13 then the only dependence on angle, in the same equation, lies with the Legendre polynomial obtained in equation 2.14. We have for the Legendre polynomials that

$$\int P_l(\cos \gamma) d\Omega_\gamma = 0, \quad \text{if } l \neq 0. \quad (2.15)$$

where $d\Omega_\gamma$ is the angular part of $d\mathbf{r}$ ($d\mathbf{r} = r^2 dr d\Omega_\gamma$, in spherical coordinates). Due to this definition, the only non-zero element in the sum in equation 2.14, if only considering the exciton ground state wave functions, is for $l = 0$. In this way equation 2.14 is simplified as:

$$\frac{1}{|\mathbf{r}_e - \mathbf{r}_h|} = \begin{cases} r_h^{-1}, & \text{if } r_e < r_h \\ r_e^{-1}, & \text{if } r_h < r_e \end{cases} \quad (2.16)$$

This expression simplifies equation 2.13 such that the total mean potential U_C is a sum of two regimes, $r_e < r_h$ and $r_h < r_e$. Using equations 2.5a and 2.5b in equation 2.13, with the approximation from equation 2.16, gives:

$$\begin{aligned} U_C &= -\frac{e^2}{\epsilon_1} 16\pi^2 A^4 \int_0^R dr_e r_e^2 j_0^2(kr_e) \cdot \left[\frac{1}{r_e} \int_0^{r_e} dr_h r_h^2 j_0^2(kr_h) + \int_{r_e}^R dr_h r_h j_0^2(kr_h) \right] \\ &= -\frac{e^2}{\epsilon_1} 16\pi^2 A^4 [I_1 + I_2], \end{aligned} \quad (2.17)$$

where

$$I_1 = \int_0^R dr_e \frac{\sin^2(kr_e)}{k^2 r_e} \int_0^{r_e} \frac{\sin^2(kr_h)}{k^2} dr_h \quad (2.18)$$

$$\approx 0.701389 \left(\frac{R}{\pi} \right)^5,$$

and

$$I_2 = \int_0^R dr_e \frac{\sin^2(kr_e)}{k^2} \int_{r_e}^R \frac{\sin^2(kr_h)}{k^2 r_h} dr_h \quad (2.19)$$

$$\approx 0.701389 \left(\frac{R}{\pi} \right)^5.$$

Assuming that the normalization constant A is given by equation 2.8, then the average Coulomb potential is given by:

$$U_C \approx -1.78607 \frac{e^2}{\epsilon_1 R}. \quad (2.20)$$

Using the result of Equation 2.20 into Equation 2.10 gives the exciton ground state energy of a strongly confined QDot to be

$$\Delta E_G(R) = E_g + \frac{\hbar^2 \pi^2}{2R^2} \left(\frac{1}{m_e^*} + \frac{1}{m_h^*} \right) - 1.78607 \frac{e^2}{\epsilon_1 R} \quad (2.21)$$

A plot of this energy band gap function for PbS is produced using some known constants. From Chapter 1.2, we have that, for PbS QDots, $E_g = 0.41\text{eV}$, $m_e^* = m_h^* = 0.085m_0$, where m_0 is the electron rest mass, $\epsilon_1 = 14.5$ and typical PbS QDot diameter ranges between 4nm and 20nm. Figure 7 presents the plot of the energy band gap of PbS QDots in function of QDot size, $d = 2R$, compared with the empirical sizing curve presented by Moreels et al in reference [8], and presented in this thesis in Equation 1.2 in Chapter 1.2. It is seen that the effective mass approximation prediction greatly overestimates the energy band energy for small diameter PbS QDots. Such an overestimation was also observed by Wang et al [29]. In this work, the overestimation is corrected by developing a "cluster" model, with a tight-binding approximation Hamiltonian. While the effective mass approximation gives, for this situation, too high exciton energies, it is an interaction model which can produce a simple analytic expression.

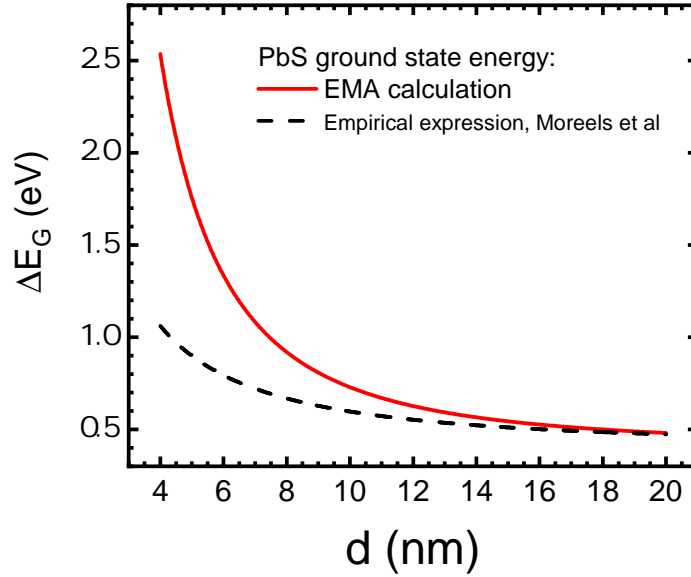


Figure 7: Ground state exciton energy, ΔE_{GS} , as function of QDot diameter, $d = 2R$, for PbS QDots, as calculated with effective mass approximation (EMA) theory, compared with the empirical sizing curve presented by Moreels et al, in reference [8].

2.2 SPONTANEOUS EMISSION AND PHOTOLUMINESCENCE IN TWO-LEVEL QUANTUM SYSTEMS

A semiconductor quantum dot has a sharp peaked, Dirac-delta like, density of states, as mentioned on Chapter 1.1. This property of QDots tells us that energy levels are sharply quantized, similarly to atoms. Thus, when involving interaction with light, the process of electronic excitation can be analogous to a two level quantum system, with a ground state and an excited state. The properties of spontaneous emission on these nanocrystals involve many variables, some of those are the band-gap energy and the surrounding environment.

Let us derive the spontaneous decay rate of a two-level quantum system located at $\mathbf{r} = \mathbf{r}_0$, which we shall call here as an "atom". The atom set initially in an excited state $|i\rangle$ will decay into a set of final states $|f\rangle$ with identical energies E_f . The set of final states only differ by the mode \mathbf{k} of the radiation field (see Figure 8). Since the transitions are independent, we sum all the transition probability for each mode to obtain the total transition rate. Here the polarization of the radiation field is neglected.

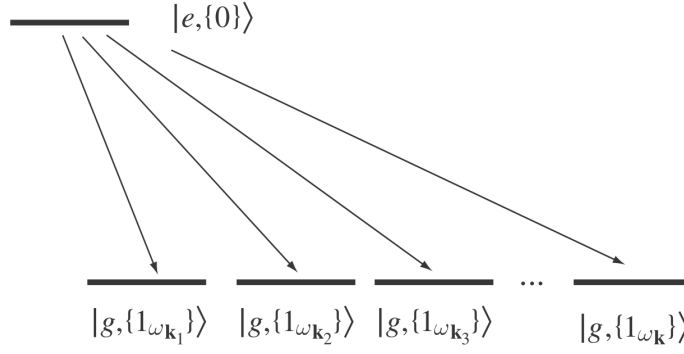


Figure 8: Transition from a initial state to a set of final states. Figure taken from reference [9].

According to Fermi's 2nd golden rule [62] the spontaneous decay rate γ is given as

$$\gamma = \frac{2\pi}{\hbar^2} \sum_f \left| \langle f | \hat{H}_I | i \rangle \right|^2 \delta(\omega_i - \omega_f), \quad (2.22)$$

where $\hat{H}_I = -\hat{\mathbf{d}} \cdot \hat{\mathbf{E}}$ is the interaction Hamiltonian in the dipole approximation, where $\hat{\mathbf{d}}$ is the dipole moment operator and $\hat{\mathbf{E}}$ the vacuum electric field operator. The initial energy is solely determined by the atom's excited state energy $E_e = \hbar\omega_i$ ⁴. On the other hand, the final energy is described by the atom and the field as $\hbar\omega_f = E_g + \hbar\omega_0$, where E_g is the energy of the ground state and $\hbar\omega_0$ is one quantum of electromagnetic radiation (photon), which is close to the exciton energy of the QDots. Therefore the delta function is a statement of energy conservation, by assuming, for $\omega_i = \omega_f$, that $E_e - E_g = \hbar\omega_0$.

Let us find the matrix elements of $\langle f | \hat{H}_I | i \rangle$. One can write $\hat{\mathbf{E}}$ in terms of the operators of the harmonic oscillator \hat{a} and \hat{a}^\dagger :

$$\hat{\mathbf{E}} = \sum_{\mathbf{k}} \left\{ \mathbf{E}_{\mathbf{k}}^+ \hat{a}_{\mathbf{k}}(t) + \mathbf{E}_{\mathbf{k}}^- \hat{a}_{\mathbf{k}}^\dagger(t) \right\}, \quad (2.23)$$

where $\mathbf{E}_{\mathbf{k}}^+$ and $\mathbf{E}_{\mathbf{k}}^-$ are the positive and negative parts of the complex electric field $\mathbf{E}_{\mathbf{k}}$, respectively, and the time-dependent harmonic oscillator operators are equal to

$$\hat{a}_{\mathbf{k}}^\dagger(t) = \hat{a}_{\mathbf{k}}^\dagger(0) \exp(i\omega_{\mathbf{k}}t) \quad \wedge \quad \hat{a}_{\mathbf{k}}(t) = \hat{a}_{\mathbf{k}}(0) \exp(-i\omega_{\mathbf{k}}t). \quad (2.24)$$

⁴ We neglect the zero point energy $\frac{1}{2}\hbar\omega_0$ since we are only interested in energy differences.

For a two-level atomic system with ground state $|g\rangle$ and excited state $|e\rangle$, the transition dipole moment operator can be rewritten as:

$$\hat{\mathbf{d}} = \mathbf{d} \left(\hat{r}^+ + \hat{r} \right), \quad (2.25)$$

with $\hat{r}^+ = |g\rangle \langle e|$ and $\hat{r} = |e\rangle \langle g|$. Here, the transition dipole moment is taken to be real, *i.e.*, $\langle g|\hat{\mathbf{d}}|e\rangle = \langle e|\hat{\mathbf{d}}|g\rangle$. Using the expressions for $\hat{\mathbf{E}}$ and $\hat{\mathbf{d}}$, equations 2.23 and 2.25 respectively, the interaction Hamiltonian \hat{H}_I is rewritten as:

$$\hat{H}_I = -\hat{\mathbf{d}} \cdot \hat{\mathbf{E}} = -\sum_{\mathbf{k}} \mathbf{d} \cdot \left[\mathbf{E}_{\mathbf{k}}^+ \hat{r}^+ \hat{a}_{\mathbf{k}}(t) + \mathbf{E}_{\mathbf{k}}^- \hat{r} \hat{a}_{\mathbf{k}}^\dagger(t) + \mathbf{E}_{\mathbf{k}}^+ \hat{r} \hat{a}_{\mathbf{k}}(t) + \mathbf{E}_{\mathbf{k}}^- \hat{r}^+ \hat{a}_{\mathbf{k}}^\dagger(t) \right] \quad (2.26)$$

The initial and final states, $|i\rangle$ and $|f\rangle$ respectively, are defined as:

$$\begin{aligned} |i\rangle &= |e, \{0\}\rangle = |e\rangle |\{0\}\rangle \\ |f\rangle &= |g, \{1_{\omega_{\mathbf{k}'}}\}\rangle = |g\rangle |\{1_{\omega_{\mathbf{k}'}}\}\rangle, \end{aligned} \quad (2.27)$$

where $|\{0\}\rangle$ stands for the zero-photon state and $|\{1_{\omega_{\mathbf{k}'}}\}\rangle$ stands for a one photon state with a mode \mathbf{k}' and frequency $\omega_0 = (E_e - E_g)/\hbar$. Operating the perturbation $\hat{\mathbf{d}} \cdot \hat{\mathbf{E}}$ on the mentioned states gives:

$$\langle f|\hat{\mathbf{d}} \cdot \hat{\mathbf{E}}|i\rangle = \mathbf{d} \cdot \sum_{\mathbf{k}} \mathbf{E}_{\mathbf{k}}^- e^{i\omega_{\mathbf{k}}t} \left\langle g, \{1_{\omega_{\mathbf{k}'}}\} \left| g, \{1_{\omega_{\mathbf{k}}}\} \right. \right\rangle, \quad (2.28)$$

$$\langle i|\hat{\mathbf{d}} \cdot \hat{\mathbf{E}}|f\rangle = \mathbf{d} \cdot \sum_{\mathbf{k}} \mathbf{E}_{\mathbf{k}}^+ e^{-i\omega_{\mathbf{k}}t} \left\langle g, \{1_{\omega_{\mathbf{k}}}\} \left| g, \{1_{\omega_{\mathbf{k}'}}\} \right. \right\rangle. \quad (2.29)$$

where Thus, the module squared $\left| \langle f|\hat{\mathbf{d}} \cdot \hat{\mathbf{E}}|i\rangle \right|^2$ is equal to:

$$\begin{aligned} \left| \langle f|\hat{\mathbf{d}} \cdot \hat{\mathbf{E}}|i\rangle \right|^2 &= \sum_{\mathbf{k}'} \sum_{\mathbf{k}} (\mathbf{d} \cdot \mathbf{E}_{\mathbf{k}'}^+ \otimes \mathbf{E}_{\mathbf{k}}^- \cdot \mathbf{p}) e^{i(\omega_{\mathbf{k}} - \omega_{\mathbf{k}'})t} \cdot \\ &\quad \cdot \langle g, \{1_{\omega_{\mathbf{k}'}}\} | g, \{1_{\omega_{\mathbf{k}}}\} \rangle \langle g, \{1_{\omega_{\mathbf{k}'}}\} | g, \{1_{\omega_{\mathbf{k}}}\} \rangle \end{aligned} \quad (2.30)$$

where we note that, as any dot product, $\mathbf{d} \cdot \mathbf{E}_{\mathbf{k}}^- = \mathbf{E}_{\mathbf{k}}^- \cdot \mathbf{d}$, and $\mathbf{E}_{\mathbf{k}'}^+ \otimes \mathbf{E}_{\mathbf{k}}^-$ stands for the outer product of the two vectors of the electric field (*i.e.*, a 3×3 matrix in 3D space with components $E_i E_j$). The matrix element 2.30 can be introduced in equation 2.22.

Expressing the sum of the final states as a sum over the modes \mathbf{k}' , the transition rate becomes

$$\begin{aligned} \gamma = & \frac{2\pi}{\hbar^2} \sum_{\mathbf{k}} \sum_{\mathbf{k}'} \left[\mathbf{d} \cdot \left(\mathbf{E}_{\mathbf{k}}^+ \otimes \mathbf{E}_{\mathbf{k}'}^- \right) \cdot \mathbf{d} \right] e^{i(\omega_{\mathbf{k}} - \omega_{\mathbf{k}'})t} \\ & \cdot \sum_{\mathbf{k}'} \langle g, \{1_{\omega_{\mathbf{k}'}}\} | g, \{1_{\omega_{\mathbf{k}'}}\} \rangle \langle g, \{1_{\omega_{\mathbf{k}'}}\} | g, \{1_{\omega_{\mathbf{k}'}}\} \rangle \delta(\omega_{\mathbf{k}} - \omega_0) \end{aligned} \quad (2.31)$$

Due to states' orthogonality, there are non-zero values in equation 2.31 only if $\mathbf{k}'' = \mathbf{k}' = \mathbf{k}$. Thus, the transition rate becomes

$$\gamma = \frac{2\pi}{\hbar^2} \sum_{\mathbf{k}} \left[\mathbf{d} \cdot \left(\mathbf{E}_{\mathbf{k}}^+ \otimes \mathbf{E}_{\mathbf{k}}^- \right) \cdot \mathbf{d} \right] \delta(\omega_{\mathbf{k}} - \omega_0). \quad (2.32)$$

If we rewrite $\mathbf{E}_{\mathbf{k}}^+$ and $\mathbf{E}_{\mathbf{k}}^-$ in terms of their respective normal modes $\mathbf{u}_{\mathbf{k}}$, such as⁵ [9]

$$\mathbf{E}_{\mathbf{k}}^+ = \sqrt{\frac{2\pi\hbar\omega_{\mathbf{k}}}{\epsilon_1}} \mathbf{u}_{\mathbf{k}} \quad \wedge \quad \mathbf{E}_{\mathbf{k}}^- = \sqrt{\frac{2\pi\hbar\omega_{\mathbf{k}}}{\epsilon_1}} \mathbf{u}_{\mathbf{k}}^* \quad (2.33)$$

where ϵ_1 is the effective dielectric constant of the surrounding medium, the decay rate in equation 2.32 can be written as:

$$\gamma = \frac{4\pi^2\omega}{3\hbar\epsilon_1} |\mathbf{d}|^2 \rho_{\text{p}}(\mathbf{r}_0, \mathbf{n}_{\text{d}}, \omega_0), \quad (2.34)$$

where $\mathbf{n}_{\text{d}} = \frac{\mathbf{d}}{|\mathbf{d}|}$ is the unit vector of the transition dipole moment \mathbf{d} , and ρ_{d} is the partial local density of states, defined as [9, 63]:

$$\rho_{\text{d}}(\mathbf{r}_0, \mathbf{n}_{\text{d}}, \omega_0) \equiv 3 \sum_{\mathbf{k}} \left[\mathbf{n}_{\text{d}} \cdot \left(\mathbf{u}_{\mathbf{k}} \otimes \mathbf{u}_{\mathbf{k}}^* \right) \cdot \mathbf{n}_{\text{d}} \right] \delta(\omega_{\mathbf{k}} - \omega_0), \quad (2.35)$$

The expression for the partial local density of states suggests that we need to integrate over a finite distribution of available final frequencies. By writing the expression in terms of a Green's dyadic $\overset{\leftrightarrow}{\mathbf{G}}$, the sum becomes a trace⁶:

$$\rho_{\text{d}}(\mathbf{r}_0, \mathbf{n}_{\text{d}}, \omega_0) = \frac{6\omega_0\eta^2}{\pi c^2} \left[\mathbf{n}_{\text{d}} \cdot \text{Im} \left\{ \overset{\leftrightarrow}{\mathbf{G}}(\mathbf{r}_0, \mathbf{r}_0; \omega_0) \right\} \cdot \mathbf{n}_{\text{d}} \right]. \quad (2.36)$$

⁵ CGS units are used in the following equations. The normal modes $\mathbf{u}_{\mathbf{k}}$ have dimensions of (volume)^{-1/2}.

⁶ See Appendix A.1 for deduction of the Green function representation of the normal modes of the electric field.

where $\eta = \sqrt{\epsilon_1}$ is the refractive index of the surrounding medium. With this equation for the partial local density of states one can calculate the spontaneous decay rate of a two-level quantum system in an arbitrary reference system. All one needs is to know the Green dyadic for the reference system.

2.2.1 Local density of states (LDOS)

In equation 2.34 the partial local density of states function $\rho_d(\mathbf{r}_0, \mathbf{n}_d, \omega_0)$ was introduced. It corresponds to the number of modes per unit volume and frequency, at the origin \mathbf{r} of the (point-like) quantum system with dipole orientation \mathbf{n}_d , into which a photon with energy $\hbar\omega_0$ can be released during the spontaneous decay process [9, 63].

If there is no fixed dipole axis \mathbf{n}_d and the medium is isotropic and homogeneous, the decay rate, given by equation 2.34 with partial local density of states given by equation 2.36, is averaged over all directions, which implies:

$$\begin{aligned}
& \langle \mathbf{n}_d \cdot \text{Im} \left\{ \overleftrightarrow{\mathbf{G}}(\mathbf{r}_0, \mathbf{r}_0; \omega_0) \cdot \mathbf{n}_d \right\} \rangle \\
&= \langle \mathbf{n}_d \cdot \mathbf{n}_d \text{Im} \left\{ \overleftrightarrow{\mathbf{G}}(\mathbf{r}_0, \mathbf{r}_0; \omega_0) \right\} \rangle \\
&= \langle |\mathbf{n}_d|^2 \text{Im} \left\{ \overleftrightarrow{\mathbf{G}}(\mathbf{r}_0, \mathbf{r}_0; \omega_0) \right\} \rangle \\
&= \frac{1}{3} \text{Im} \left\{ \text{Tr}[\overleftrightarrow{\mathbf{G}}(\mathbf{r}_0, \mathbf{r}_0; \omega_0)] \right\}
\end{aligned} \tag{2.37}$$

where $\langle \dots \rangle = n^{-1} \text{Tr}[\dots]$, where n is the number of elements of the vector. Inserting this result in equation 2.35 defines the total local density of states ρ , given by:

$$\begin{aligned}
\rho(\mathbf{r}_0, \omega_0) &= \frac{6\omega_0\eta^2}{\pi c^2} \left[\frac{1}{3} \text{Im} \left\{ \text{Tr}[\overleftrightarrow{\mathbf{G}}(\mathbf{r}_0, \mathbf{r}_0; \omega_0)] \right\} \right] \\
&= \frac{2\omega_0\eta^2}{\pi c^2} \left[\text{Im} \left\{ \text{Tr}[\overleftrightarrow{\mathbf{G}}(\mathbf{r}_0, \mathbf{r}_0; \omega_0)] \right\} \right] \\
&= \sum_{\mathbf{k}} |u_{\mathbf{k}}(\mathbf{r}_0, \omega_0)|^2 \delta(\omega_{\mathbf{k}} - \omega_0),
\end{aligned} \tag{2.38}$$

where, in the last step, the following relation between the Green function and the normal modes $\mathbf{u}_{\mathbf{k}}$ was used ⁷

$$\frac{2\omega_0\eta^2}{\pi c^2} \text{Im} \overset{\leftrightarrow}{\mathbf{G}}(\mathbf{r}_0, \mathbf{r}_0; \omega_0) = \sum_{\mathbf{k}} \mathbf{u}_{\mathbf{k}}^*(\mathbf{r}_0, \omega_{\mathbf{k}}) \mathbf{u}_{\mathbf{k}}(\mathbf{r}_0, \omega_{\mathbf{k}}) \delta(\omega_{\mathbf{k}} - \omega_0). \quad (2.39)$$

In summary, the spontaneous decay rate is proportional to the partial local density of states, which depends on the transition dipole between the two atomic states involved in the transition. Only in homogeneous environments or after orientational averaging can ρ_{d} be replaced by the total local density of states. In free space, for instance, the LDOS is uniform and ρ is equal to

$$\rho_0 = \frac{\omega_0^2 \eta^3}{\pi^2 c^3} \quad (2.40)$$

which, if $\eta = 1$, is the density of electromagnetic modes as encountered in, e.g., blackbody radiation [9, 63]. Using equation 2.40 in equation 2.34 gives the decay rate for a homogenous environment written as

$$\gamma = \frac{4E^3 \eta}{3\hbar^4 c^3} |\mathbf{d}|^2, \quad (2.41)$$

where $E = \hbar\omega_0$.

2.3 DIPOLE-DIPOLE RESONANCE INTERACTION BETWEEN TWO QUANTUM DOTS

In a wide range of phenomena in chemical physics, intermolecular interactions determine the observed behaviour of a system. These interactions are stronger at small distances, such that the molecule's wave function overlap and electron exchange occur, also known as electronic transfer [64, 65]. Nonetheless, inter-molecular interactions still remain significant at greater distances, such that individual molecules can be regarded as chemically distinct. The mechanism for these long-range interactions is electromagnetic; in this regime lies the non-radiative energy transfer. Energy transfer is different from electronic transfer in the sense that there is no net transport of charge; the charge neutral excitation is transferred as an entity from the donor to the acceptor.

In this section a thorough theoretical description of the non-radiative energy transfer mechanism is given, assuming the dipole approximation in the interaction Hamil-

⁷ See Appendix A.1 for the full derivation.

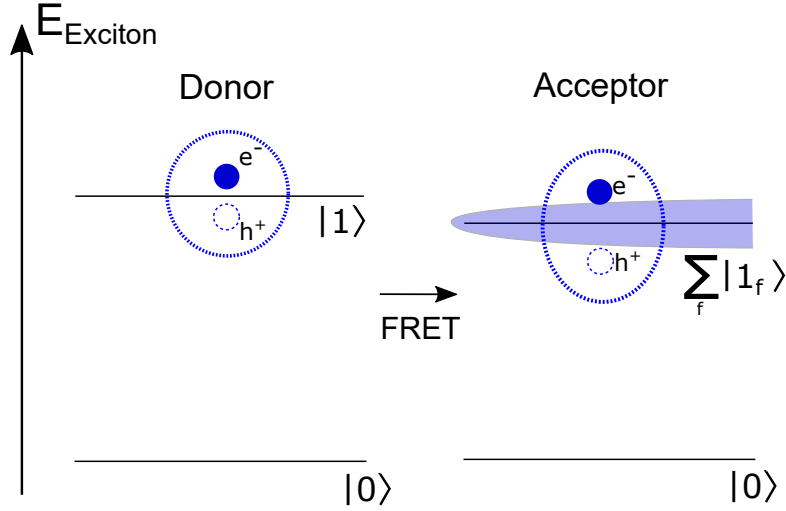


Figure 9: Excitonic picture of the donor-acceptor quantum system. The horizontal arrow shows the direction of the exciton transfer. There can be a distribution of allowed final exciton states.

tonian between two QDots [5, 66]. The energy transfer process can be considered using an excitonic (i.e, electron-hole) picture of the quantum system (see Figure 9). Alternatively, the process can be described using the single-particle picture, as it has been done in the classical work of D. Dexter [67]. This approach will be presented in Chapter 2.4. If the QDots are in the strong-confinement regime (as reported for PbS QDots [8, 26, 59, 60]), electron-hole interaction is negligible, and, thus, the exciton and the single-electron pictures are completely equivalent.

Here we shall consider two quantum dots of the same size R in a homogeneous dielectric medium with permittivity ϵ_1 . In the beginning the donor particle, labelled D , is photo-excited, being in state $|D_{n_i l_i m_i}\rangle$, whilst the acceptor particle, labelled A , is de-excited, being in state $|A_{\text{ground}}\rangle$. The initial state is described as the product of the initial states of the donor and acceptor QDots, and photons with wave vector \mathbf{k} and polarization λ ,

$$|i\rangle = |D_{n_i l_i m_i}\rangle |A_{\text{ground}}\rangle |N_{\mathbf{k}, \lambda}\rangle, \quad (2.42)$$

with energy $E_i = E_{n_i l_i}^{(D)} + N\hbar\omega_{\mathbf{k}}$ ⁸. The final state consists of the acceptor QDot in a excited state, the donor QDot in the ground state and the same number of photons, $N_{\mathbf{k}, \lambda}$, of the system, with wave vector \mathbf{k} and polarization λ ,

$$|f\rangle = |D_{\text{ground}}\rangle |A_{n_f l_f m_f}\rangle |N_{\mathbf{k}, \lambda}\rangle, \quad (2.43)$$

⁸ The energy of ground state is set to be zero, so there is no net contribution of $|A_{\text{ground}}\rangle$ to E_i .

with energy $E_f = E_{n_f l_f}^{(A)} + N\hbar\omega_{\mathbf{k}}$ ⁹.

Resonant energy transfer is promoted via an interaction Hamiltonian, described by a electric dipole interaction approximation, which takes the form

$$\hat{H}_{QD}^{\mathbf{r}} = -\hat{\mathbf{d}}_{QD} \cdot \mathbf{E}_{\mathbf{k},\lambda}(\mathbf{r}), \quad (2.44)$$

where $\hat{\mathbf{d}}_{QD}$ is the electric dipole momentum operator, induced on the quantum dot by the electric field measured in position \mathbf{r} , $\mathbf{E}_{\mathbf{k},\lambda}(\mathbf{r})$, which can be rewritten with the construction and annihilation harmonic oscillators, $\hat{a}_{\mathbf{k},\lambda}^{\dagger}$ and $\hat{a}_{\mathbf{k},\lambda}$ respectively, as

$$\mathbf{E}_{\mathbf{k},\lambda}(\mathbf{r}) = i \left(\frac{2\pi\hbar\omega_{\mathbf{k}}}{V\epsilon_1} \right)^{1/2} \left\{ \mathbf{e}_{\mathbf{k},\lambda} \hat{a}_{\mathbf{k},\lambda} e^{i(\mathbf{k}\cdot\mathbf{r} - \omega_{\mathbf{k}}t)} - \mathbf{e}_{\mathbf{k},\lambda}^* \hat{a}_{\mathbf{k},\lambda}^{\dagger} e^{-i(\mathbf{k}\cdot\mathbf{r} - \omega_{\mathbf{k}}t)} \right\}, \quad (2.45)$$

where $\mathbf{e}_{\mathbf{k}}$ and $\mathbf{e}_{\mathbf{k}}^*$ are the electromagnetic radiation polarization vectors, ϵ_1 is the effective dielectric constant of the surrounding medium and V is an arbitrary quantization volume.

2.3.1 Energy transfer matrix element

In order to determine the system's transfer matrix element $M_{i \rightarrow f}$, using second order perturbation theory, two virtual intermediate states of the system are defined, which involve the creation of virtual photons¹⁰, such as

$$\begin{aligned} |I_1\rangle &= |D_{\text{ground}}\rangle |A_{\text{ground}}\rangle |N_{\mathbf{k},\lambda} + 1\rangle; \\ |I_2\rangle &= |D_{n_i l_i m_i}\rangle |A_{n_f l_f m_f}\rangle |N_{\mathbf{k},\lambda} + 1\rangle, \end{aligned} \quad (2.46)$$

⁹ For the same reason as for E_i , there is no net contribution of $|D_{\text{ground}}\rangle$ to E_f .

¹⁰ In Quantum Field theory, a virtual photon is presented as a particle which mediates the exchange of momentum, *i.e.*, mediates the interactions, between two electromagnetic fields. The term "virtual" arises because these photons cannot be observed. Intermediate quantum states add virtual photons to the quantum system, which could be wrongly understood as a violation of conservation of energy but, due to its short term lifetime, the Heisenberg uncertainty principle tells us there is high uncertainty in energy, and it can actually have the same energy as the initial and final states. Further intuitions over the concept of virtual photons in Quantum Electrodynamics can be found on reference [68]. For a more in-depth theoretical description of manifestations of electromagnetic fields consider reading Quantum Field Theory books, such as Chapter 1.5 of reference [69].

which have energies $E_{I_1} = (N + 1)\hbar\omega_{\mathbf{k}}$ and $E_{I_2} = E_{n_i l_i}^{(D)} + E_{n_f l_f}^{(A)} + (N + 1)\hbar\omega_{\mathbf{k}}$. The quantum amplitude for RET, i.e. the matrix element $M_{i \rightarrow f}$ is calculated with the following expression ¹¹:

$$M_{i \rightarrow f} = \sum_{\mathbf{k}, \lambda} \left\{ \frac{\langle f | \hat{H}_{QD} | I_1 \rangle \langle I_1 | \hat{H}_{QD} | i \rangle}{E_i - E_{I_1}} + \frac{\langle f | \hat{H}_{QD} | I_2 \rangle \langle I_2 | \hat{H}_{QD} | i \rangle}{E_i - E_{I_2}} \right\}. \quad (2.47)$$

The acceptor QDot is located at position \mathbf{r}_A , whilst the donor is located at position \mathbf{r}_D . The vector \mathbf{R} defines the distance between the donor-acceptor pair, $\mathbf{R} = \mathbf{r}_A - \mathbf{r}_D$. If the resonance condition is fulfilled, then the initial and final energies of the system should be the same: $E_i = E_f \Rightarrow E_{n_i l_i}^{(D)} = E_{n_f l_f}^{(A)} \equiv E_{nl}$. Let us assume, as well, without losing generality, that the initial state of the system doesn't have photons, i.e. $N_{\mathbf{k}, \lambda} = 0$. This way, the state energies are rewritten as: $E_i = E_{n_i l_i}^{(D)}$, $E_f = E_{n_f l_f}^{(A)}$, $E_{I_1} = \hbar\omega_{\mathbf{k}}$ and $E_{I_2} = E_i + E_f + \hbar\omega_{\mathbf{k}}$. Using this information, Equation 2.47 is rewritten as

$$M_{i \rightarrow f} = \sum_{\mathbf{k}, \lambda} \left\{ \frac{\langle f | \hat{H}_{QD}^{(\mathbf{r}=\mathbf{r}_A)} | I_1 \rangle \langle I_1 | \hat{H}_{QD}^{(\mathbf{r}=\mathbf{r}_D)} | i \rangle}{E_{n_i l_i}^{(D)} - \hbar\omega_{\mathbf{k}}} - \frac{\langle f | \hat{H}_{QD}^{(\mathbf{r}=\mathbf{r}_D)} | I_2 \rangle \langle I_2 | \hat{H}_{QD}^{(\mathbf{r}=\mathbf{r}_A)} | i \rangle}{E_{n_i l_i}^{(D)} + \hbar\omega_{\mathbf{k}}} \right\}, \quad (2.48)$$

where $\hat{H}_{QD}^{(\mathbf{r}=\mathbf{r}_A)}$ and $\hat{H}_{QD}^{(\mathbf{r}=\mathbf{r}_D)}$ indicate the position where the Hamiltonian is interacting with the virtual photon.

Using the Hamiltonian defined in equation 2.44, writing the electric field as in equation 2.45, the matrix element is written as ¹²:

$$M_{i \rightarrow f} = \frac{1}{\epsilon_1} \mathbf{d}_A \mathbf{T} \mathbf{d}_D, \quad (2.49)$$

where $\mathbf{d}_A \equiv \mathbf{d}_A^{(f, g)} \equiv \langle A_{n_f l_f m_f} | \hat{\mathbf{d}}_A | A_{\text{ground}} \rangle$ and $\mathbf{d}_D \equiv \mathbf{d}_D^{(g, i)} \equiv \langle D_{\text{ground}} | \hat{\mathbf{d}}_D | D_{n_i l_i m_i} \rangle$ are the matrix elements of the transition dipole moment acting on the acceptor and the donor, respectively, and the tensor \mathbf{T} is defined as,

$$\mathcal{T}_{\alpha\beta} \equiv -q^3 \left[A(qR) \delta_{\alpha\beta} + B(qR) n_\alpha n_\beta \right] e^{iqR}, \quad (2.50)$$

11 This expression comes from using second order time-dependent perturbation theory on transitions from discrete states into continuous states. In this chapter's problem, the initial state corresponds to the state $|i\rangle$ and the final state corresponds to the state $|f\rangle$. See, for instance, chapter 13.4 of reference [70] for a development of this type of state transitions in time-dependent perturbation theory.

12 See Appendix A.2 for the full derivation.

with $A(x) = \frac{1}{x} + \frac{i}{x^2} - \frac{1}{x^3}$, $B(x) = -\frac{1}{x} - \frac{3i}{x^2} + \frac{3}{x^3}$, $q = \frac{\sqrt{\epsilon_1}}{\hbar c} E_{nl}$, \mathbf{R} is the donor-acceptor distance vector, $n_{\alpha,\beta} = R_{\alpha,\beta}/R$ is the unit vector of \mathbf{R} , i.e., $\mathbf{n} = \mathbf{R}/R$.

In the near-field approximation, where energy transfer is mediated by a virtual photon, $qR \ll 1$. Therefore, in this regime, the $1/(qR)^3$ factors are the dominant terms in $A(qR)$ and $B(qR)$ in equation A.33, which leads to an exciton transfer matrix element given as:

$$M_{i \rightarrow f} = \frac{1}{\epsilon_1 R^3} \{ (\mathbf{d}_A \cdot \mathbf{d}_D) - 3(\mathbf{d}_A \cdot \mathbf{n})(\mathbf{d}_D \cdot \mathbf{n}) \}. \quad (2.51)$$

2.3.2 Transfer rate

The exciton transfer rate, analogous with the non-radiative decay rate of the pair of QDots, is given by the Fermi's golden rule [62] in the form

$$\begin{aligned} \gamma_{D \rightarrow A} &= \frac{2\pi}{\hbar} \sum_{i,f} P_{n_i l_i m_i} |M_{i \rightarrow f}|^2 \delta(E_i - E_f) \\ &= \frac{2\pi}{\hbar} \sum_{i,f} P_{n_i l_i m_i} |M_{i \rightarrow f}|^2 \delta \left(E_{n_i l_i}^{(D)} - E_{n_f l_f}^{(A)} \right) \end{aligned} \quad (2.52)$$

The delta function in equation 2.52 shows the requirement of energy conservation so that exciton transfer can resonantly occur. The function $P_{n_i l_i m_i}$ is a distribution function which states the probability of finding a QDot in the initial state $\{n_i, l_i, m_i\}$. Since the transient dipole moments are randomly oriented, it is valid to assume the average of the modulus of the matrix element squared as an approximation. By using equation 2.51, the average value of $|M_{i \rightarrow f}|^2$ is given as¹³:

$$\langle |M_{i \rightarrow f}|^2 \rangle = \frac{2}{3\epsilon_1^2 R^6} |\mathbf{d}_A|^2 |\mathbf{d}_D|^2 \quad (2.53)$$

Using this result on equation 2.52 yields:

$$\gamma_{D \rightarrow A} = \frac{4\pi}{3\hbar\epsilon_1^2 R^6} \sum_{i,f} P_{n_i l_i m_i} \left| \mathbf{d}_A^{(f,g)} \right|^2 \left| \mathbf{d}_D^{(g,i)} \right|^2 \delta \left(E_{n_i l_i}^{(D)} - E_{n_f l_f}^{(A)} \right) \quad (2.54)$$

where we retrieved the notation simplification $\mathbf{d}_A \equiv \mathbf{d}_A^{(f,g)}$ and $\mathbf{d}_D \equiv \mathbf{d}_D^{(g,i)}$, for clarity. Equation 2.54 is the general result for the transfer rate, regardless of the structure of the quantum dots. It shows that the energy transfer rate is not dependent on the

¹³ See Appendix A.3 for the full derivation.

density of optical states, contrary to some previous suggestions, and in agreement with recent theory [54].

2.4 FRET RATE AND THE FÖRSTER RADIUS IN DEXTER'S THEORY

Förster showed that the rate of resonance energy transfer from an electronically excited donor (D) to an acceptor (A) separated by a distance R decreases as R^{-6} , as it follows from equation 2.54. He wrote this relation, as previously presented in Chapter 1.3, in the form [49]

$$\gamma_{D \rightarrow A} = \frac{1}{\tau_D} \left(\frac{R_0}{R} \right)^6, \quad (2.55)$$

where R_0 is the Förster radius, which defines the distance between two quantum dots at which the probability of resonant non-radiative energy transfer is equal to the probability of the internal decay of the donor quantum dot, via radiative or non-radiative decay channels, and τ_D is the isolated donor lifetime, which is defined as the inverse of the donor decay rate, i.e., $\tau_D = 1/\gamma_D$. The value of R_0 sets the length scale of FRET for a given pair of emitters and depends on their spectroscopic properties [49, 71]. The relation is written in numerical form, widely used by experimentalists, as follows

$$R_0^6 = \frac{9000(\ln 10)\kappa^2\phi_f}{128\pi^5 N_A \eta^4} \int_0^\infty F_D(\lambda)\epsilon_A(\lambda)\lambda^4 d\lambda, \quad (2.56)$$

where the integral accounts for the spectral overlap of the normalized donor fluorescence spectrum $F_D(\lambda)$ with the absorption spectrum of the acceptor $\epsilon_A(\lambda)$. The Förster radius also depends on the isolated donor fluorescence quantum yield ϕ_f , in units of area times energy, the refractive index η of the medium in the wavelength range of spectral overlap, the Avogadro's number N_A , and the orientation factor κ^2 , which depends on the angle between the transition dipole moments of the donor (D) and acceptor (A) emitters θ_{DA} , and the angles θ_D and θ_A between each of these dipoles and the vector connecting their centres [49, 71]:

$$\kappa^2 = (\cos(\theta_{DA}) - 3 \cos \theta_D \cos \theta_A)^2. \quad (2.57)$$

For a single D-A pair, the value of κ^2 is in the range between 0 and 4. For an ensemble of D-A pairs, κ^2 is usually preaveraged over the distribution of all orientations to give $\langle \kappa^2 \rangle = 2/3$ if the emitters undergo rotational motion faster than the fluorescence lifetime¹⁴, and $\langle \kappa^2 \rangle = 0.476$ if the dipoles are randomly oriented and do not rotate on the time scale of fluorescence [71]. The expression for the Förster radius in equation 2.56 was firstly proposed for fluorescence molecules. For study of QDots, it is commonly considered the overlap integral of the absorption and emission spectra of QDot ensembles, broadened due to the usual size dispersion of the QDot samples. Moreover, in QDot ensembles a sizeable Stokes shift is present between the emission and absorption spectra, due to QDot aggregates and size broadening. However, all these QDot ensemble effects are irrelevant to the interactions between individual QDots. To understand the energy transfer between individual QDots the derivation of Chapter 2.3 is better suited to study individual QDot interactions, and equation 2.54, from Chapter 2.3.2, describes the energy transfer between a pair of donor and acceptor QDots .

A detailed derivation of equation 2.56, and overall resonant energy transfer mechanism, was performed by Dexter, arriving to the results introduced by Förster and generalizing energy transfer for dipole-quadrupole, quadrupole-quadrupole and higher order interactions of the electromagnetic field in crystals [67]. In Dexter's approach, single electron states describe the initial and final states of the energy transfer, contrary to the exciton picture as considered in chapter 2.3 (see Figure 10). The final states have a bandwidth of energies, $\Delta\omega$.

In the next subchapter a thorough derivation of equation 2.56 in the light of the work of Dexter will be presented. The decay rate $\gamma_{D \rightarrow A}$ will be derived as previously in Chapter 2.3 (see equation 2.54 as the final result), but here accounting for the spectroscopic properties of the donor and acceptor, and interactions with the environment. Afterwards, relating with the phenomenological relation for the FRET rate, equation 2.55, the derivation of formula for the Förster radius is complete.

2.4.1 Derivation of the Dexter expression for the Förster radius

Dexter developed a theory of light emission in crystalline phosphors, where the light is absorbed by an impurity, called absorber, and then the energy is non-radiatively

¹⁴ This factor of 2/3 is the same as presented in equation 2.53 in chapter 2.3.2, as a result of averaging the transition dipoles orientation.

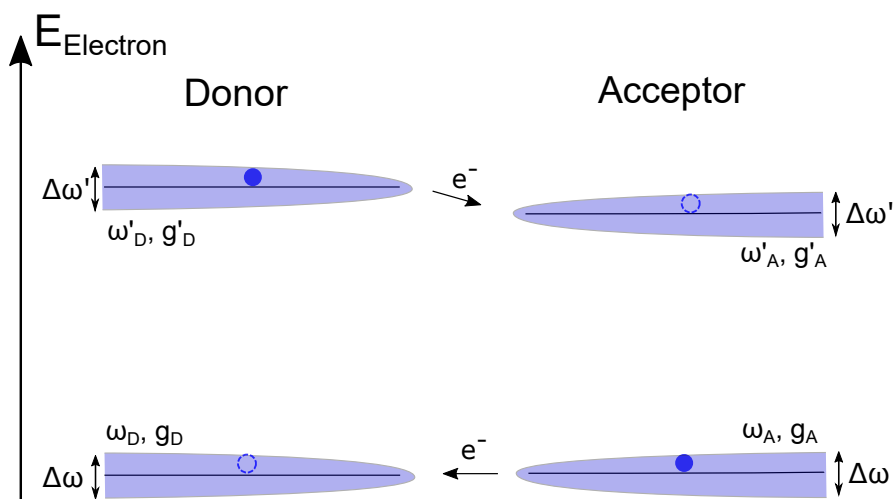


Figure 10: Electronic picture for the FRET mechanism in Dexter's formulation. The horizontal arrows describe the direction of electron transfer. The states are broadened due to molecule interactions with the surrounding medium. It is assumed the same state broadening of the excited ($\Delta\omega'$) and ground ($\Delta\omega$) states for the donor and acceptor.

transferred to another impurity, called emitter, both embedded in an insulating crystal [67]. This theory is equivalent to the initial idea of Förster and the simple quantum-mechanical consideration presented in Chapter 2.3. In our terminology, the absorber impurity is a donor and the emitter impurity is the acceptor. One assumes as well small concentrations of donors and acceptors, such that the transfer probability from one donor to another donor is negligible and the probability of formation of either donor or acceptor clusters is negligible. Therefore, one can consider a single donor-acceptor pair as before, except for admitting a distribution of the electronic state energies for both of them.

In Dexter's theory, the donor and acceptor interact with the environment and their states are broadened, as a consequence. Specifically, they are coupled to the surrounding crystal lattice where a continuum of acoustic phonons exists; consequently, the electronic states also form a continuum with a characteristic width $\Delta\omega$ ¹⁵. Dexter considered FRET in the single-electron picture where the electrons are transferred simultaneously in the opposite directions (See Figure 10).

Let us define the wavefunctions of our system. The initial wavefunction, Ψ_i , describes the configuration where the donor is excited, ψ'_D , with energy ω'_D , and the acceptor is in the ground state, ψ_A , with energy ω_A . The final wavefunction, Ψ_f ,

¹⁵ During this chapter we consider ω has dimension of energy.

corresponds to the configuration where the donor is in the ground state, ψ_D , with energy ω_D , and the acceptor is in the excited state, ψ'_A , with energy ω'_A .

The electronic wavefunctions of continuum states are usually normalised to delta functions. For the unexcited donor and acceptor states, the normalization is as follows

$$\int \psi_D^*(\mathbf{r}_1; \omega_D, j) \psi_D(\mathbf{r}_1; \tilde{\omega}_D, \tilde{j}) d\mathbf{r}_1 = \delta(\omega_D - \tilde{\omega}_D) \delta_{j, \tilde{j}} \quad (2.58a)$$

$$\int \psi_A^*(\mathbf{r}_2; \omega_A, k) \psi_A(\mathbf{r}_2; \tilde{\omega}_A, \tilde{k}) d\mathbf{r}_2 = \delta(\omega_A - \tilde{\omega}_A) \delta_{k, \tilde{k}} \quad (2.58b)$$

where \mathbf{r}_1 and \mathbf{r}_2 stand for the donor and acceptor positions in space, respectively, and indices j and k stand for the j -th and k -th degenerate state of ψ_D and ψ_A , respectively. Similar normalization follows for the excited states labelled by ω'_D and ω'_A .

For transitions to a continuum of finite states, the Fermi's golden rule is written as

$$d\gamma_{D \rightarrow A} = \frac{2\pi}{\hbar} \left| \langle \Psi_i | H_1 | \Psi_f \rangle \right|^2 \delta(E_i - E_f) dv_f \quad (2.59)$$

where $E_i = \omega'_D + \omega_A$ and $E_f = \omega_D + \omega'_A$, and dv_f denotes the interval of values of all quantum numbers necessary for the complete definition of the final states. If these states are degenerate, labelling them just by their energies is not sufficient. In our case, dv_f is equal to $d\omega'_A d\omega_D$ plus a sum over these degenerate states, from 1 to $g_f = g'_A g_D$ such as,

$$\int dv_f = \sum_{k'=1}^{g'_A} \sum_{j=1}^{g_D} \int d\omega'_A \int d\omega_D \quad (2.60)$$

where g'_A corresponds to the degeneracy of the excited acceptor states and g_D to the degeneracy of the lower energy (unexcited) donor states. Also, we will take an average over the initial states, which also form a continuum (see Figure 10), in a similar way by using the following expression

$$\sum_{k=1}^{g_A} \sum_{j'=1}^{g'_D} \int d\omega_A p_A(\omega_A) \int d\omega'_D p'_D(\omega'_D) \frac{1}{g_A g'_D} \quad (2.61)$$

where $p'_D(\omega'_D)$ and $p_A(\omega_A)$ are probability functions which describe the probabilities that the donor is in the particular (excited) energy state denoted by ω'_D and that the acceptor is in energy (ground) state ω_A .

Introducing equations 2.60 and 2.61 in equation 2.59 gives the transition probability integrated over a continuum of finite states as

$$\begin{aligned} \gamma_{D \rightarrow A} = & \frac{2\pi}{\hbar} \frac{1}{g_A g_D'} \sum_{k, j'}^{g_A, g_D'} \sum_{k', j}^{g_A', g_D} \int_0^\infty d\omega_A p_A(\omega_A) \int_0^\infty d\omega_D' p_D'(\omega_D') \int_{\Delta\omega} d\omega_D \int_{\Delta\omega'} d\omega_A' \\ & \times |\langle H_1(\omega_D', j', \omega_A, k; \omega_D, j, \omega_A', k') \rangle|^2 \delta [(\omega_D' - \omega_D) - (\omega_A' - \omega_A)] \end{aligned} \quad (2.62)$$

where $\langle H_1 \rangle$ denotes the dipole-dipole interaction Hamiltonian's matrix element between the initial state $\Psi_i(\mathbf{r}_1, \mathbf{r}_2; \omega_D', j', \omega_A, k)$ and the final state $\Psi_f(\mathbf{r}_1, \mathbf{r}_2; \omega_D, j, \omega_A', k')$ of two uncorrelated electrons¹⁶. The delta function in Equation 2.62 removes one integration, by defining $E \equiv \omega' - \omega$, and we have

$$\begin{aligned} \gamma_{D \rightarrow A} = & \frac{2\pi}{\hbar} \frac{1}{g_A g_D'} \sum_{k, j'}^{g_A, g_D'} \sum_{k', j}^{g_A', g_D} \int_{\Delta E} dE \int_0^\infty d\omega_A p_A(\omega_A) \int_0^\infty d\omega_D' p_D'(\omega_D') \\ & \times |\langle H_1(\omega_D', j', \omega_A, k; \omega_D' - E, j, \omega_A + E, k') \rangle|^2. \end{aligned} \quad (2.63)$$

The interval of integration is the sum of broadenings of the ground and excited levels, $\Delta E = \Delta\omega' + \Delta\omega$; if the broadenings are different for donor and acceptor, the larger one should be taken, in order to integrate over the broadest possible energy range at which there is resonance between the donor and acceptor states.

Dipole-dipole interaction

In the dipole-dipole approximation we assume that the donor has an allowed transition, so that the dipole term for the donor has the largest contribution, compared with higher order interactions. As calculated in Chapter 2.3.1, in the case of discrete levels, the matrix element $\langle H_1 \rangle$ would be equal to

$$\langle H_1 \rangle = \frac{1}{\eta^2 R^3} [(\mathbf{d}_A \cdot \mathbf{d}_D) - 3(\mathbf{d}_A \cdot \mathbf{n})(\mathbf{d}_D \cdot \mathbf{n})] \quad (2.64)$$

¹⁶ This means one can divide the states such as $\Psi_i(\mathbf{r}_1, \mathbf{r}_2; \omega_D', j', \omega_A, k) = \psi_D'(\mathbf{r}_1; \omega_D', j') \otimes \psi_A(\mathbf{r}_2; \omega_A, k)$ and $\Psi_f(\mathbf{r}_1, \mathbf{r}_2; \omega_D, j, \omega_A', k') = \psi_D(\mathbf{r}_1; \omega_D, j) \otimes \psi_A'(\mathbf{r}_2; \omega_A', k')$.

where R is the donor-acceptor distance, $\mathbf{n} = \mathbf{R}/R$, $\eta = \sqrt{\epsilon_1}$ is the refractive index of the medium and \mathbf{d}_A and \mathbf{d}_D are the transient dipole moments of the corresponding discrete transitions.

For the case of continuum, due to the normalization of the wavefunctions, shown in equation 2.58, we replace in equation 2.64:

$$\begin{aligned}\mathbf{d}_A &\rightarrow \mathbf{P}_A^{(k,k')}(\omega_A, \omega_A + E) \\ \mathbf{d}_D &\rightarrow \mathbf{P}_D^{(j',j)}(\omega'_D, \omega'_D - E)\end{aligned}\tag{2.65}$$

where the quantities \mathbf{P} can be interpreted as spectral densities of such dipole moments, because of the wavefunctions have here dimensions of $(\text{energy} \times \text{volume})^{-1/2}$. Angular averaging of $|\langle H_1 \rangle|^2$, as in the case of vectors \mathbf{d}_A and \mathbf{d}_D presented in Chapter 2.3.1, yields:

$$\langle |\langle H_1 \rangle|^2 \rangle = \frac{2}{3\eta^4 R^6} \left| \mathbf{P}_A^{(k,k')}(\omega_A, \omega_A + E) \right|^2 \left| \mathbf{P}_D^{(j',j)}(\omega'_D, \omega'_D - E) \right|^2.\tag{2.66}$$

Substituting equation 2.66 in equation 2.63 yields

$$\begin{aligned}\gamma_{D \rightarrow A} &= \frac{4\pi}{3\hbar\eta^4 R^6} \int_{\Delta E} dE \\ &\times \left\{ \sum_{k=1}^{g_A} \sum_{k'=1}^{g'_A} \int_0^\infty d\omega_A p_A(\omega_A) \left| \mathbf{P}_A^{(k,k')}(\omega_A, \omega_A + E) \right|^2 \right\} \\ &\times \left\{ \sum_{j=1}^{g_D} \sum_{j'=1}^{g'_D} \int_0^\infty d\omega'_D p'_D(\omega'_D) \left| \mathbf{P}_D^{(j',j)}(\omega'_D, \omega'_D - E) \right|^2 \right\}.\end{aligned}\tag{2.67}$$

Now we shall show that the same squared moduli of \mathbf{P}_A and \mathbf{P}_D of equation 2.67 appear in the absorption and emission spectra of the acceptor and donor, respectively.

From equation 2.41 of Chapter 2.1, the spontaneous emission rate of a point emitter located inside a medium with a refractive index η is given by

$$\gamma(E) = \frac{4E^3\eta}{3\hbar^4 c^3} |\mathbf{d}|^2.\tag{2.68}$$

Equation 2.68 is valid in the case of a two-level system, with inter-level distance E . If the levels are broadened, equation 2.68 can be generalized in the same way as equation 2.54, of Chapter 2.3.2, for the FRET rate and we need to introduce the emission spectral density, \mathcal{W}^{em} . Considering the broadened energy bands of the donor emitter, we have:

$$\mathcal{W}_D^{\text{em}}(E) = \frac{1}{g'_D} \sum_{j=1}^{g'_D} \sum_{j'=1}^{g'_D} \frac{4E^3 \eta^3}{3\hbar^4 c^3} \int_0^\infty d\omega'_D p_D(\omega'_D) \left| \mathbf{P}_D^{(j',j)}(\omega'_D, \omega'_D - E) \right|^2. \quad (2.69)$$

Notice that

$$\int \mathcal{W}_D^{\text{em}}(E) dE = \tau_D^{-1}, \quad (2.70)$$

where τ_D is the radiative lifetime of the excited donor.

The absorption cross-section, σ^{abs} , is defined as [72]:

$$\sigma^{\text{abs}} \equiv \frac{W^{\text{abs}}}{|\langle \mathbf{S} \rangle|} \quad (2.71)$$

where W^{abs} is the absorbed power and $\langle \mathbf{S} \rangle$ is the time-averaged Poynting vector of the incident wave, with its the modulus equal to [72]

$$|\langle \mathbf{S} \rangle| = \frac{c\eta}{8\pi} |\mathbf{E}_0|^2 \quad (2.72)$$

where $|\mathbf{E}_0|$ is the field amplitude. For a two-level system, σ^{abs} can be related to the spontaneous emission rate as follows [9]

$$\sigma^{\text{abs}}(E) = \hbar^3 \left(\frac{\pi c}{E\eta} \right)^2 \gamma(E) \delta(\omega' - \omega - E) \quad (2.73)$$

where ω' and ω denote the excited and ground state energies. One can generalize equation 2.73 for a unexcited acceptor with broadened energy bands in a similar way as equation 2.69, as follows

$$\sigma_A^{\text{abs}}(E) = \frac{4\pi^2 E}{3\hbar c \eta} \frac{1}{g_A} \sum_{k=1}^{g_A} \sum_{k'=1}^{g'_A} \int_0^\infty d\omega_A p_A(\omega_A) \left| \mathbf{P}_A^{(k,k')}(\omega_A, \omega_A + E) \right|^2 \quad (2.74)$$

Using the results of equations 2.69 and 2.74 in equation 2.67, we find

$$\gamma_{D \rightarrow A} = \frac{3\hbar^4 c^4}{4\pi R^6 \eta^4} \int_{\Delta E} dE \frac{\mathcal{W}_D^{\text{em}}(E) \sigma_A^{\text{abs}}(E)}{E^4}. \quad (2.75)$$

Following Dexter, we may introduce normalized dimensionless lineshapes of donor emission, such as

$$f_D^{\text{em}}(E) = \tau_D^{-1} \cdot \mathcal{W}_D^{\text{em}}(E) \quad (2.76)$$

so that $\int f_D^{\text{em}}(E)dE = 1$, and

$$F_A^{\text{abs}}(E) = Q^{-1} \cdot \sigma^{\text{abs}}(E) \quad (2.77)$$

where

$$Q = \int \sigma^{\text{abs}}(E)dE \quad (2.78)$$

is the area under the absorption curve of the acceptor. With these lineshapes we get:

$$\gamma_{D \rightarrow A} = \frac{3\hbar^4 c^4 Q}{4\pi R^6 \eta^4 \tau_D} \int dE \frac{f_D^{\text{em}}(E) F_A^{\text{abs}}(E)}{E^4}. \quad (2.79)$$

One can write equation 2.79, by defining the Förster radius, R_0 , in the form

$$\gamma_{D \rightarrow A} = \frac{1}{\tau_D} \left(\frac{R_0}{R} \right)^6 \quad (2.80)$$

with

$$R_0^6 \equiv \frac{3\hbar^4 c^4 Q}{4\pi \eta^4} \int dE \frac{f_D^{\text{em}}(E) F_A^{\text{abs}}(E)}{E^4} \quad (2.81)$$

The formula for R_0 of equation 2.81 it is precisely the form in which it is written in reference [73]. In the case of QDots, however, this formula is of limited use. The individual spectra of single QDots (or a very small number of them) are not obtained in experiments; it is observed the broad emission and absorption spectra of large ensembles of QDots, with size broadening and considerable Stokes energy shift. Thus, the typical Förster radius calculation in QDot ensembles may induce errors and wrong values for the calculated Förster radius.

2.5 FRET IN 3-DIMENSIONAL QDOT ENSEMBLES

Let us assume a system of two quantum dots: a donor QDot at position \mathbf{r}_D and a acceptor QDot at a position \mathbf{r}_A . Let us assume that the donor is at the origin of the coordinate system, i.e, $\mathbf{r}_D = 0$. The rate of resonance energy transfer between donor and acceptor QDots, $\gamma(R_A)$, is given, as seen in Chapter 2.4¹⁷, by

$$\gamma(R_A) = \frac{1}{\tau_D} \left(\frac{R_0}{R_A} \right)^6, \quad (2.82)$$

where $R_A = |\mathbf{r}_A - \mathbf{r}_D| = |\mathbf{r}_A|$, τ_D is the decay time of the isolated donor and R_0 is the Förster radius. The description of FRET in this system relies on the donor survival probability, i.e, the probability of the donor QDot being in its excited state at time t , which is given by [71]:

$$\phi(t, R_A) = \exp[-t \cdot \gamma(R_A)]. \quad (2.83)$$

When N acceptors, for only one donor emitter, are included one introduces N possible donor decay channels. If the acceptors behave independently from each other, then we consider N two-particle systems. The excited donor survival probability is now given by:

$$\begin{aligned} \phi(t; R_1, R_2, \dots, R_N) &= e^{-t\gamma(R_1)} \cdot e^{-t\gamma(R_2)} \cdot \dots e^{-t\gamma(R_N)} \\ &= \prod_{i=1}^N \exp[-t\gamma(R_i)] \end{aligned} \quad (2.84)$$

The number of acceptors for each site i (assuming that the distance between acceptors in each individual site is very small) may vary. For instance, the probability of finding one acceptor at \mathbf{r}_i may be small. Therefore, one must define a distribution function $g(\mathbf{r}_i, j)$, which defines the probability of having j acceptors at a distance \mathbf{r}_i . Since the acceptors behave independently from each other, the distribution function can be described by a Poisson distribution, with a mean equal to the mean number of acceptors $\Delta n_A(\mathbf{r}_i)$ (defined as $\Delta n_A = d\mathbf{r}_i C_A(\mathbf{r}_i)$, where $C_A(\mathbf{r}_i)$ is the number of acceptors per unit volume):

$$g(\mathbf{r}_i, j) = e^{-\Delta n_A(\mathbf{r}_i)} \frac{\Delta n_A^j(\mathbf{r}_i)}{j!}. \quad (2.85)$$

¹⁷ Unlike as it is presented in Chapter 2.4, here $\gamma_{D \rightarrow A} \equiv \gamma$, for notation simplicity.

The donor survival probability with j acceptors at same distance \mathbf{r}_i is given by:

$$\phi_{j,R_i}(t) = \left[e^{-t\gamma(R_i)} \right]^j \quad (2.86)$$

Introducing the distribution function $g(\mathbf{r}_i, j)$ the donor survival probability is rearranged, and it is given by the average of $f(t)$ over all possible j -values, weighted by $g(\mathbf{r}_i, j)$:

$$\begin{aligned} \phi_{R_i}(t) &= \sum_{j=0}^{\infty} g(\mathbf{r}_i, j) \phi_{j,R_i}(t) \\ &= \sum_{j=0}^{\infty} g(\mathbf{r}_i, j) \left[e^{-t\gamma(R_i)} \right]^j \end{aligned} \quad (2.87)$$

Finally, the contribution of all acceptors at different distances yields the donor decay probability as

$$\begin{aligned} \phi(t) &= \prod_{R_i} \phi_{R_i}(t) \\ &= \prod_{R_i} \left(\sum_{j=0}^{\infty} g(\mathbf{r}_i, j) \left[e^{-t\gamma(R_i)} \right]^j \right) \end{aligned} \quad (2.88)$$

Using Poisson's distribution, i.e, equation 2.85, in the equation 2.88 gives

$$\begin{aligned} \phi(t) &= \prod_{R_i} \left\{ e^{-\Delta n_A(\mathbf{r}_i)} \sum_{j=0}^{\infty} \frac{1}{j!} \left[\Delta n_A(\mathbf{r}_i) e^{-t\gamma(R_i)} \right]^j \right\} \\ &= \prod_{R_i} \left\{ e^{-\Delta n_A(\mathbf{r}_i)} e^{\Delta n_A(\mathbf{r}_i) \exp[-t\gamma(R_i)]} \right\} \\ &= \exp \left\{ -\Delta n_A(\mathbf{r}_i) \sum_{R_i} [1 - \exp(-t\gamma(R_i))] \right\} \end{aligned} \quad (2.89)$$

where, in the second step of the derivation the Maclaurin series $e^x = \sum_j x^j / j!$ was used. Considering that the donor is inside a continuous restricted space with volume V , the sum in equation 2.89 can be transformed to an integral form:

$$\phi(t) = \exp \left(- \int_V d\mathbf{r} C_A(\mathbf{r}) \left\{ 1 - \exp[-t\gamma(|\mathbf{r}|)] \right\} \right). \quad (2.90)$$

This integral is performed over the volume of the sample containing acceptors with concentration $C_A(\mathbf{r})$. This donor decay probability will greatly depend on the con-

centration of the acceptors and their distribution over the sample. To describe real systems of colloidal QDots, one must determine the distribution of acceptors, which is usually is not possible, so an assumption has to be made. Here two reasonably possible distributions are presented. Other more complex structures were studied by Farinha et al [71].

2.5.1 Homogeneous Distribution

If we consider a homogeneous concentration of acceptors in 3D space, $C_A(\mathbf{r}) = C_0$, Equation 2.90 can be simplified, using spherical coordinates:

$$\phi(t) = \exp\left(-C_0 \int_{-\pi}^{\pi} d\varphi \int_0^{\pi} d\theta \sin\theta \int_{R_e}^{\infty} dr \{1 - \exp[-\gamma(r)t]\} r^2\right), \quad (2.91)$$

where the lower limit R_e is the donor-acceptor encounter distance, i.e, their minimum approach distance, usually taken to be the sum of the donor and the acceptor van der Waals radii [71]. Here we take the approximation $R_e \rightarrow 0$, assuming a particle ensemble where interaction distances are much bigger than the QDot average radius. Using Equation 2.82, the former equation yields:

$$\begin{aligned} \phi(t) &= \exp\left(-4\pi C_0 \int_0^{\infty} dr \left\{1 - \exp\left[-\left(\frac{R_0}{r}\right)^6 \frac{t}{\tau_D}\right]\right\} r^2\right) \\ &= \exp\left(-\frac{4}{3}\pi^{3/2} C_0 R_0^3 \left(\frac{t}{\tau_D}\right)^{1/2}\right). \end{aligned} \quad (2.92)$$

Using the last equation, the donor decay rate is given by:

$$\begin{aligned} f(t) &= I_0 \exp(-t/\tau_D) \cdot \phi(t) \\ &= I_0 \exp\left(-\frac{t}{\tau_D} - \frac{4}{3}\pi^{3/2} C_0 R_0^3 \left(\frac{t}{\tau_D}\right)^{1/2}\right), \\ &= I_0 \exp\left\{-\left(\frac{t}{\tau_D}\right)^{1/2} \left[\left(\frac{t}{\tau_D}\right)^{1/2} + \sqrt{\pi} N_0\right]\right\}. \end{aligned} \quad (2.93)$$

where I_0 is the amplitude of the donor decay, which depends on the (assumed homogeneous) 3D concentration of donor emitters, and N_0 is the number of acceptors in a homogeneous sphere with Förster radius R_0 . This expression resembles the stretched-exponential decay curve for fixed $\beta = 1/2$ (see chapter 2.6).

2.5.2 "Fixed-shell" Distribution

This distribution places the acceptors in a shell of radius a , with a single donor in the centre of the sphere. Thus, the concentration $C_A(\mathbf{r})$ is defined as

$$C_A(\mathbf{r}) = \frac{N}{4\pi a^2} \delta(r - a), \quad (2.94)$$

where N is the number of acceptors. Introducing equation 2.94 in 2.90, using spherical coordinates, yields

$$\begin{aligned} \phi_{\text{shell}} &= \exp \left(-\frac{N}{4\pi a^2} \int_{-\pi}^{\pi} d\varphi \int_0^{\pi} d\theta \sin \theta \int_0^{\infty} dr \delta(r - a) \left\{ 1 - \exp[-t\gamma(r)] \right\} r^2 \right) \\ &= \exp \left(-N \left\{ 1 - \exp \left[-\left(\frac{R_0}{a} \right)^6 \frac{t}{\tau_D} \right] \right\} \right). \end{aligned} \quad (2.95)$$

The donor total decay function for the fixed-shell distribution is then given by:

$$\begin{aligned} I_D(t) &= I_0 \exp(-t/\tau_D) \cdot \phi_{\text{shell}}(t) \\ &= I_0 \exp \left\{ -\frac{t}{\tau_D} - N \left[1 - \exp \left[-\left(\frac{R_0}{a} \right)^6 \frac{t}{\tau_D} \right] \right] \right\}. \end{aligned} \quad (2.96)$$

If one assumes that, for large volumes, the concentration of acceptors in a shell distribution is approximately equal to the concentration in a homogeneous distribution, one can define the number of acceptors N as

$$N = \frac{4}{3} \pi C_0 a^3,$$

where C_0 is the homogeneous distribution of acceptors, as considered in chapter 2.5.1. With this definition, equation 2.96 can be rewritten as

$$\begin{aligned}
 I_D(t) &= I_0 \exp \left\{ -\frac{t}{\tau_D} - \frac{4}{3} \pi C_0 R_0^3 \left(\frac{R_0}{a} \right)^{-3} \left[1 - \exp \left[- \left(\frac{R_0}{a} \right)^6 \frac{t}{\tau_D} \right] \right] \right\} \\
 &= I_0 \exp \left\{ -\frac{t}{\tau_D} - N_0 \left(\frac{R_0}{a} \right)^{-3} \left[1 - \exp \left[- \left(\frac{R_0}{a} \right)^6 \frac{t}{\tau_D} \right] \right] \right\},
 \end{aligned} \tag{2.97}$$

where N_0 is the number of acceptors in a sphere of radius R_0 , $N_0 = \frac{4}{3} \pi C_0 R_0^3$. These definitions let us relate all parameters of the decay function of the homogeneous distribution and the decay function of the "fixed-shell" distribution, and introduces the parameter a , i.e, the distance of the shell of acceptors to the donor.

2.6 PHOTOLUMINESCENCE DECAY IN QDOTS

After a short laser pulse which excites QDots, they emit light, with decreasing intensity, over a considerable time. This temporal evolution is called photoluminescence decay kinetics. It is determined by the the light emission itself, i.e, the radiative decay, and a number of non-radiative decay mechanisms, of which FRET is an example, because it moves the excitation to another class of emitters, the acceptors. For historical reasons, point emitters (such as QDots or dye molecules) sometimes are called fluorophores.

This chapter reviews the theoretical description of decay kinetics of QDots.

2.6.1 Decay time in fluorophores

A sample containing a fluorophore is excited with a infinitely sharp pulse of light, i.e, a delta function [12]. This yields an initial population n_0 of fluorophores in the excited state. The excited state population decays with a rate $\Gamma + \Gamma_{nr}$ according, in first approximation, to

$$\frac{dn(t)}{dt} = -(\Gamma + \Gamma_{nr})n(t), \tag{2.98}$$

where $n(t)$ is the number of excited QDots at time t after excitation, Γ is the emissive decay rate and Γ_{nr} is the non-radiative decay rate. Emission is a random event, and each excited fluorophore has the same probability of emitting in a given period of time.

The lifetime, i.e., the inverse of the decay rate, is the average time a fluorophore remains in its excited state following excitation. This can be interpreted as the average time in the excited state $\langle t \rangle$, which value is obtained by averaging t over the intensity decay of the fluorophore, $I(t)$, such as:

$$\langle t \rangle = \frac{\int_0^{\infty} tI(t)dt}{\int_0^{\infty} I(t)dt} \quad (2.99)$$

In fluorescence experiments one does not observe the number of excited QDots. Instead one sees the fluorescence intensity $I(t)$. The decay of the fraction of excited emitters $n(t')/n(0)$ at time t' is described with cumulative distribution function $[1 - n(t')/n(0)]$, where $n(0)$ is the concentration of excited emitters at $t' = 0$ [74]. The concentration $n(t')$ for $t' \rightarrow \infty$ tends to zero, so the cumulative function varies between 1 (for $t' \rightarrow \infty$) and 0 (for $t' \rightarrow 0$). The reliability function and the probability function, $g(t)$, the former related with the decay curve, are related as follows:

$$\int_0^{t'} g(t)dt = 1 - \frac{n(t')}{n(0)} \quad (2.100)$$

Equation 2.100 shows that the decrease of the concentration of the excited emitters at time t' is equal to the integral of all previous decay events. So, the fluorescence intensity is not necessarily proportional with the concentration of excited emitters.

2.6.2 Decay models

The decay behaviour of quantum dots may vary and depend on their environment. Different types of QDots will have a different decay rate behaviour as well. Some QDots, such as CdSe, have a single-exponential trend whilst other type of QDots show a multi-exponential, or even non-exponential, decay over time. This will influence the response function $I(t)$.

In the literature there are several proposed decay functions, that include

1. Single-exponential decay;

2. Bi-exponential decay;
3. Log-normal distribution of decay rates;
4. Stretched exponential decay, or Kohlrausch function.

SINGLE-EXPONENTIAL FUNCTION: A single-exponential decay function $I(t)$ is defined as,

$$I(t) = I_0 e^{-\Gamma t}. \quad (2.101)$$

As fitting parameters equation 2.101 has the scaling factor I_0 and the decay rate Γ .

BI-EXPONENTIAL DECAY: The bi-exponential model is written as:

$$I(t) = I_1 e^{-\Gamma_1 t} + I_2 e^{-\Gamma_2 t}, \quad (2.102)$$

containing four fitting parameters, namely the scaling factors I_0 and I_1 and the decay rates Γ_1 and Γ_2 .

It is possible to generalize the behaviour of the last equations to an integral [74] and use a distribution function $\phi(\Gamma)$ to describe the scaling factor for each value of Γ . The expression is given by

$$I(t) = \int_0^{\infty} d\Gamma \phi(\Gamma) e^{-\Gamma t}. \quad (2.103)$$

LOG-NORMAL DISTRIBUTION OF DECAY RATES: The log-normal distribution of decay rates $\phi_{LN}(\Gamma)$ was successfully employed to fit decay decay curves from CdSe quantum dots inside titania inverse opals (same found in PbS QDot suspension in toluene) [13, 74]. The function $\phi_{LN}(\Gamma)$ is defined as

$$\phi_{LN}(\Gamma) = A \exp\left(-\frac{\ln^2(\Gamma/\Gamma_{mf})}{\omega^2}\right), \quad (2.104)$$

where Γ_{mf} is the most frequent decay rate and ω is the dimensionless width parameter which is related to the width of the distribution as its $1/e$ height $\Delta\Gamma$ via:

$$\Delta\Gamma = 2\Gamma_{mf} \sinh(\omega). \quad (2.105)$$

Thus, the decay curve $I_{\text{LN}}(t)$, i.e., the response function, for a log-normal distribution is given by:

$$\begin{aligned} I_{\text{LN}}(t) &= \int_0^{\infty} d\Gamma \phi_{\text{LN}}(\Gamma) e^{-\Gamma t} \\ &= \int_0^{\infty} d\Gamma \exp \left[-\frac{\ln^2(\Gamma/\Gamma_{mf})}{\omega^2} - \Gamma t \right] \end{aligned} \quad (2.106)$$

STRETCHED-EXPONENTIAL FUNCTION Other widely decay model in the literature is the stretched-exponential function, or Kohlrausch function [74, 75], defined as:

$$I(t) = \exp \left(-(\Gamma t)^\beta \right) \exp(-\Gamma t) \quad (2.107)$$

where β is a stretch parameter, which varies between 0 and 1.

2.6.3 Non-exponential decay in QDots

Non-exponential photoluminescence decay profiles may come from the interaction of QDot ensembles with the surrounding environment, which may lead to an infinite distribution of rate constants. One way used to find the underlying probability distribution function of rate constants is to calculate the integral equation for QDot photoluminescence decays. Another approach is by choosing a known mathematical function as the distribution function of rate constants. However, one must carry special attention to the chosen mathematical function since, though it may fit well the experimental decay profile of QDots, it may not show physical significance for the system (log-normal distribution, for example) [75].

As presented in Chapter 2.6.2, one of the most conveniently used mathematical functions for the distribution of rate constants is the Kohlrausch, or stretched exponential, function. The stretched exponential function is reported to have firm grounds in the description of the luminescence intensity decay in condensed matter [75], first derived by Förster from models of luminescence quenching

$$I_D(t) = \exp \left(-\frac{t}{\tau_D} \right) \exp \left[-P \left(\frac{t}{\tau_D} \right)^\beta \right], \quad (2.108)$$

where the first exponential term represents the exponential part of the kinetics, determined by the intrinsic radiative and nonradiative transitions in the species under study, and the second term accounts for the relaxation part, shaped by Förster resonant energy transfer (FRET) or FRET-type mechanisms. In the former equation, equation τ_D is lifetime of the excited state of the donor in the absence of the acceptor (or quencher), β is a stretch parameter, which varies between 0 and 1, and the parameter P is proportional to the concentration of acceptors, and depends on the Förster radius.

Other implemented functions have in consideration the existence of trap states in QDots, which may come from structural defects or dangling bonds. A model was developed by Bodunov et al where a QDot ensemble is surrounded by N identical traps (hole or electron traps) which can trap an electron (or hole) with a finite trapping rate k_1 and released afterwards to the QDot with rate k_2 [75].

A QDot ensemble is characterized by a certain distribution of quantum dot sizes, where the size of the QDs relates with the band gap energy of this semiconductor particles. This distribution can approximately be described by a Gaussian function, such as

$$F(E) = \frac{1}{\sqrt{2\pi}\sigma} \exp\left(-\frac{(E - E_0)^2}{2\sigma^2}\right), \quad (2.109)$$

where E_0 is the average energy of the QDots and σ is the width of the distribution. One may argue that non-radiative transitions in the ensemble occur at a rate k , which is a function of energy E , $k = k(E)$. By averaging the luminescence decay contribution of all QDots leads to a non-exponential behaviour

$$I_{QD}(t) = \int_{-\infty}^{\infty} \exp\left(-\frac{t}{\tau} - k(E)t\right) F(E)dE = \exp\left(-\frac{t}{\tau}\right) I_{QDrel}(t), \quad (2.110)$$

$$I_{QDrel}(t) = \int_{-\infty}^{+\infty} \exp(-k(E)t)F(E)dE.$$

MAIN TECHNIQUES AND EXPERIMENTAL PROCEDURE

3.1 TIME-CORRELATED SINGLE PHOTON COUNTING (TCSPC)

Time-Correlated Single Photon Counting (abbreviated as TCSPC) is a time-resolved technique which fundamentally is based on the detection and timing of single emitted photons. This single photon detection technique uses the fact that the light intensity is so low that the probability of detecting one photon is very small. Thus, it is not necessary to consider the possibility of detecting multiple photons in one signal period, hence the single-photon detection nature of TCSPC [10]. The time from the emission of the photon to the arrival to the detector is recorded and, this way, histograms of counts as a function of the arrival time are produced after repeated photon detection periods (see Figure 11). Since the single-photon probability detection is so low, there is not detected any photon in many photon detection periods. Detection periods with more than one photon are very rare [10]. TCSPC is an effective technique to study photoluminescence properties of QDots. Some other applications of TCSPC are fluorescence microscopy on biological macromolecules and cellular imaging [12].

The heart of this method is a time-to-amplitude converter (TAC), which can be considered as a very fast stopwatch (see Figure 12). The sample is repetitively excited using a pulsed light source, like a pulsed laser or flash lamp¹. Each pulse is optically monitored, using an high-speed photo-diode or photo-multiplier (PMT), to create a start signal that triggers the voltage ramp in the TAC. The voltage ramp is stopped when the first fluorescence photon from the sample is detected. The voltage ramp produced in the TAC is proportional to the time between the start and stop signals². A multichannel analyser (MCA) converts the voltage into a time channel using an

¹ Typical instrumentation for TCSPC uses high repetition rate mode-locked picosecond (ps) or femto-second (fs) pulsed laser sources [12, 10] and pulsed LEDs [12].

² In practice, the start and stop signals can be reversed, since the probability of a detecting an initial laser pulse is much greater than the probability of detecting the single photon, thus guarantees that the counting is stopped at each laser pulse.

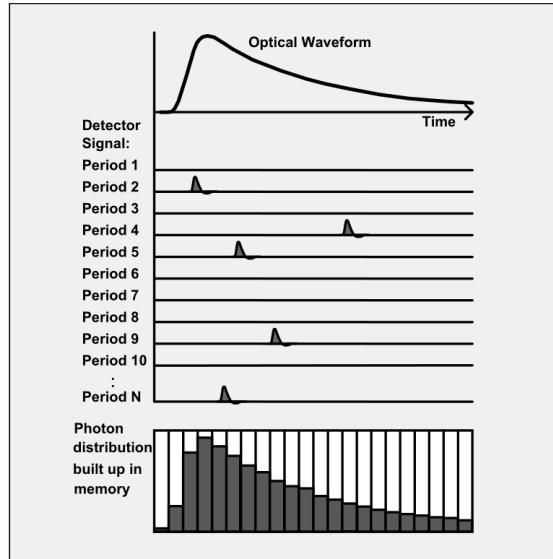


Figure 11: General principle of the Time-Correlated Single Photon Counting technique (TCSPC). Image obtained from reference [10].

analog-to-digital converter (ADC). As summing over many pulses, the MCA produces a probability histogram of counts versus time channels [12].

The signal conversion by the ADC holds the voltage during a period of time at which no other photon can be detected. This is known as the electronic dead time of the detector. The dead time ranges between 10 microseconds in older systems to around 120 nanoseconds in more recent TCSPC electronics [12]. Depending on the desired accuracy, the light intensity must be limited to detect 0.1 to 0.01 photons per signal period [10, 12], since the dead time in the electronics prevents detection of another photon resulting from the same excitation pulse. If many photons arrive at the same time, and only one is counted, the intensity statistics is distorted, which is named "photon pile-up".

Another important feature in TCSPC is the use of the rising edge of the photoelectron pulse, generated in the photomultiplier, for timing. This allows the PMT's phototubes with nanosecond pulse widths to provide sub-nanosecond resolution [12].

There are typically three components associated with an intensity decay. These are:

1. instrument response function $L(t_k)$;
2. sample's response function $N(t_k)$;

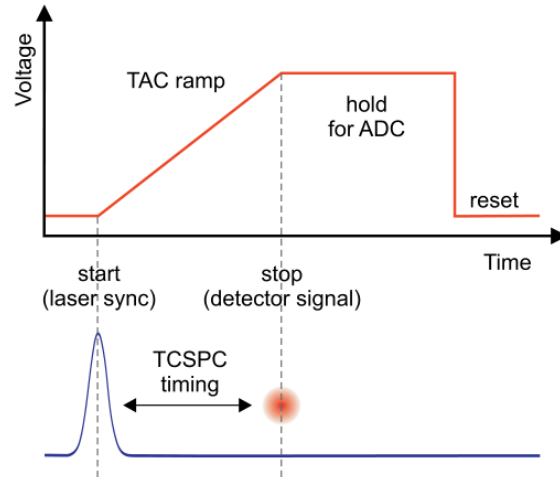


Figure 12: Operation principle of a time-to-amplitude converter (TAC). Image obtained from reference [11].

3. calculated decay function $N_c(t_k)$.

All three functions are described in terms of discrete times (t_k) because the counted photons are collected into channels/bins, each with a known time (t_k) time and width (Δt). The instrument response function $L(t_k)$ is the response of the instrument to a zero-lifetime sample. This curve is typically collected using a dilute scattering solution such as colloidal silica and no emission filter [12]. This decay represents the shortest time profile which can be measured by the instrument. Afterwards, the measured curve is the intensity decay of the sample itself $N(t_k)$, as it is recorded with no prior signal processing. The last curve, $N_c(t_k)$, is calculated data, which is the modelled function. This curve represents a convolution of the instrument response function $L(t_k)$ with the impulse response function $I(t)$, which is the intensity decay law. The fitted function is the time profile expected for a given intensity decay when one considers the form of the instrument response function $L(t_k)$. By choosing the proper impulse response function $I(t)$ one gets the form of $N(t_k)$ as close as possible.

3.1.1 Convolution integral

As mentioned, in TCSPC the measured intensity $N(t_k)$ is a convolution of the instrument response function $L(t_k)$ with the sample's response signature $I(t)$. In reality, most instrument response functions are 0.5 to 2 ns wide [12]. We can consider the

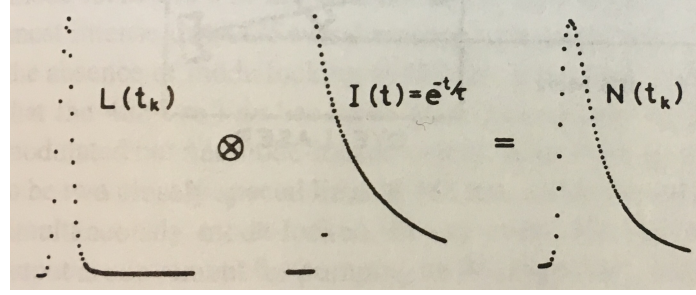


Figure 13: Convolution of an instrument response function $L(t_k)$ with the sample's response signature $I(t)$ to yield the measured data $N(t_k)$. Figure obtained from reference [12].

excitation pulse to be a series of δ -functions with different amplitudes. Each δ -function excitation is assumed to excite an impulse response at t_k , such as:

$$I_k(t) = L(t_k)I(t - t_k)\Delta t, \quad (3.1)$$

where $L(t_k)$ is the instrument response function, $I(t - t_k)$ is the sample response function beginning at $t = t_k$. The measured decay $N(t_k)$ is the sum of the impulse responses created by all the individual δ -function excitation pulses created by all the individual δ -function excitation pulses occurring until t_k ,

$$N(t_k) = \sum_{t=0}^{t=t_k} I_k(t) = \sum_{t=0}^{t=t_k} L(t_k)I(t - t_k)\Delta t \quad (3.2)$$

For small values of Δt , we can re-write the equation as an integral:

$$N(t) = \int_0^t L(t')I(t - t')dt' \quad (3.3)$$

This expression says that the intensity measured experimentally at time t is a sum of the intensities of all δ -function excitation pulse that occur until time t . The important factor now is to find the impulse response function $I(t)$ with best matches the experimental data. In Chapter 2.5 and Chapter 2.6 some theoretical background regarding the adequate fit of impulse functions, or decay functions, for photoexcited colloidal QDots is presented.

3.1.2 Working with near-infrared lasers on quantum dot samples

At near-infrared wavelengths it is useful to find the ratio F_{NIR} between the number of detected quantum dot emission events, N_{QDE} , and the number of excitation pulses, N_E .

Accounting the average background $\langle B \rangle$ for an TCSPC experiment with a measured data set $M(t_i)$, F_{NIR} is defined as [13]

$$F_{NIR} = \frac{N_{QDE}}{N_E} = \frac{\sum_i (M(t_i) - \langle B \rangle)}{N_E}. \quad (3.4)$$

For good signal to noise ratios F_{NIR} should be as large as possible [13]. However, too large values will cause photon pile-up at the dead time of counting module. The upper limit for F_{NIR} is determined by the dynamical behaviour of the system of interest. For PbSe quantum dots, for instance, it was shown that for $F_{NIR} > 1\%$ the goodness of the fit deviates significantly from $\chi_{red}^2 = 1$ [13]. For $F_{NIR} < 1\%$ it was observed that $\chi_{red}^2 \approx 1$.

The χ_{red}^2 is defined as:

$$\chi_{red}^2 \equiv \frac{1}{N-p} \chi^2 = \frac{1}{N-p} \sum_{i=1}^N \frac{(D_f(t_i) - I(t_i))^2}{\sigma_{D_f}^2(t_i)} \quad (3.5)$$

Here, t_i was chosen as the running parameter, N is the number of data point, p is the number of adjustable parameters, $D_f(t_i)$ is the measured data of the i^{th} time bin, $I(t_i)$ is the corresponding value from the fitting model and $\sigma_{D_f}^2(t_i)$ is the variance of the datum at time t_i . If a model $I(t)$ fits the experimental data well, then the equation 3.5 should result in $\chi_{red}^2 = 1$.

3.2 OPTICAL TABLE SETUP FOR TCSPC AND EMISSION SPECTRUM STUDIES

In this chapter is presented a description of the experimental setup used to study the photoluminescence properties of colloidal PbS QDots samples. The experimental setup was made over an optical table, whose goal lied on acquiring sample's emission spectra and produce TCSPC measurements.

MAIN COMPONENTS OF SETUP

1. PicoQuant PL-800B laser driver + PicoQuant LDH-C 690 diode laser head (685 nm laser pulse - NIR spectral range);
2. HP Function Generator;
3. Piezoelectric XYZ stage sample holder;

4. Thorlabs XYZ translation stage;
5. Small NA objective
6. Nikon High NA objective
7. Spectrometer Acton SP500i;
8. 85 grooves/mm blazed diffraction grating = $1.3 \mu\text{m}$;
9. 900 grooves/mm holographic diffraction grating = High IR;
10. PicoQuant PicoHarp300 TCSPC system;
11. Photomultiplier;
12. Liquid nitrogen cooled CCD 1D array detector;

PULSED LASER The pulsed laser beam is generated with the PicoQuant 800-B laser driver with a 685 nm laser head. The laser driver is externally triggered using a function generator, in order to produce pulsed beams with variable repetition rate. In the work made on this report a range of repetition rates from 32 kHz until 200 kHz was used.

ALIGNMENT In the laser setup, the incoming laser beam targets a small NA objective, positioned over a XYZ translation stage, which focus the laser beam into the sample, held on a piezoelectric stage. The emitted light from the sample strikes a collecting high NA objective, which produces a wide beam that strikes the spectrometer. One of the most important stages in the laser setup alignment lies in aligning the small NA objective with the XYZ stage in order to overlap the focus points of the two objectives. The piezoelectric stage lets find the position of the sample where the collected signal is maximum.

The beam collection is made in the spectrometer, using a 900 grooves/mm holographic diffraction grating. This grating has a very small spacing between grooves, and, therefore, most of the incoming light coming in different wavelengths will preferentially be refracted to a specific angle. This way, all light is focused in a small amount of pixels, being easier to detect a signal in the CCD sensor. The incoming data from the CCD sensor is processed on a PC with the software *WinSpec*.

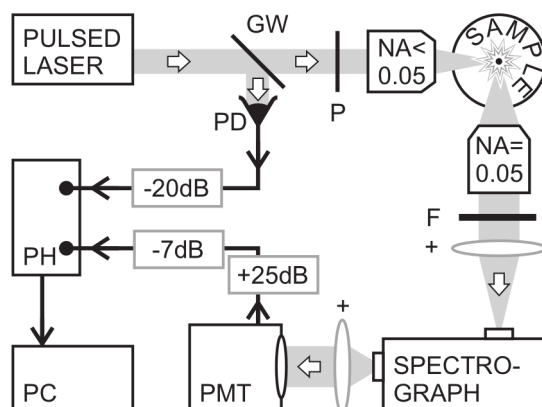


Figure 14: Scheme of the setup for Time Correlated Single Photon Counting (TCSPC) experiments. [13]

EMISSION SPECTRA After alignment of the laser, to detect the emission spectra of the samples it is used a 85 grooves/mm blazed diffraction grating inside the spectrometer. To scan different wavelengths of incoming light the grating rotated tilted. The diffracted wavelengths are targeted into the CCD sensor. Data is transferred into a PC and collected in the software *WinSpec*.

COLLECTION OF TCSPC HISTOGRAMS To produce time-resolved photon counting measurements, the 85 grooves/mm blazed diffraction grating is used inside the spectrometer, with the same procedure as with the collection of emission spectra. A small mirror tilts the diffracted light into a photomultiplier (PMT), producing an 800V amplification signal. The PicoQuant PicoHarp 300 TCSPC system (PH) has the built-in time-to-amplitude converter (TAC), multichannel analyser and the analog-to-digital converter (ADC).

The TCSPC system (see Figure 14) detects a small signal from the initial laser pulse, using a photodiode (PD), which triggers the voltage ramp of the TAC. The signal coming from the PMT stops the voltage ramp, and the TAC translates the voltage ramp into a time gap. The collected data in the TSCPC system is further processed in the software *PicoHarp 300*, proprietary of PicoQuant.

3.3 BINDING OF QUANTUM DOTS VIA MOLECULAR LINKERS

The chemical process of cross-linking QDots, also known as QDot binding, at nanometre distance is of utmost experimental importance for introducing a non-radiative energy transfer mechanism such as FRET into the QDot system. Thus, fundamental

control of the cross-linking process is needed in order to proceed with experimental TCSPC and emission spectra measurements.

The colloidal PbS QDot samples used in the experiments in this thesis are capped with glutathione and were cross-linked with EDC and NHS molecules. Water-soluble glutathione capped PbS QDots were reported by Deng et al [76] to have a high quantum yield ($> 30\%$), favourable storage stability, high photostability and low cytotoxicity, i.e, low toxicity to biological cells. The interaction of EDC and NHS molecules with the glutathione capping produce the QDot binding. In this chapter, a brief description of the interacting molecules, as well as the chemistry procedure used for the PbS QDot binding, are presented.

3.3.1 Interacting molecules

GLUTATHIONE Glutathione (abbreviated as GSH) is an antioxidant in plants, animals, fungi, and some bacteria and archaea. Its molecular formula is $C_{10}H_{17}N_3O_6S$ [77]. It is a tripeptide with a gamma peptide linkage between the carboxyl group of the glutamate side chain and cysteine. The molecular structure of GSH is presented on Figure 15 with highlighted the aminoacids, the amide bond between both aminoacids and the carboxyl groups, which stay on the edges of the molecule chain. These carboxyl groups lay are the main functional groups which interact with neighbouring molecules, along with the amide group.

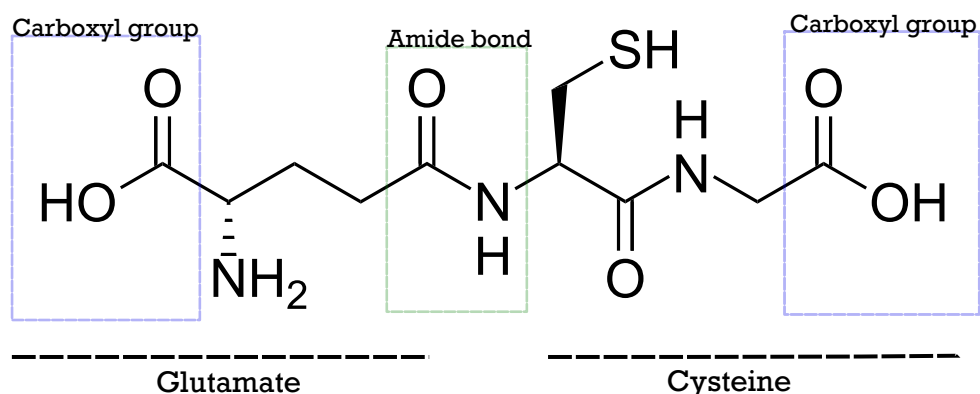


Figure 15: The molecular structure of Glutathione. Figure adapted from reference [14].

EDC AND N-HYDROXYSULFOSUCCINIMIDE (NHS) EDC (1-Ethyl-3-(3-dimethylaminopropyl)carbodiimide) is the most popular, water-soluble, carbodiimide used for conjugating biological substances containing carboxylates and amines [15, 78]. It is

used as a carboxyl activating agent for the coupling of primary amides to yield amide bonds. Its application in particle and surface conjugation goes along with the use of N-Hydroxysuccinimide (abbreviated as NHS). NHS enables the control and modification of carbodiimide crosslinking reactions involving activation of carboxylates ($-\text{COOH}$) for conjugation with primary amines ($-\text{NH}_2$) [16].

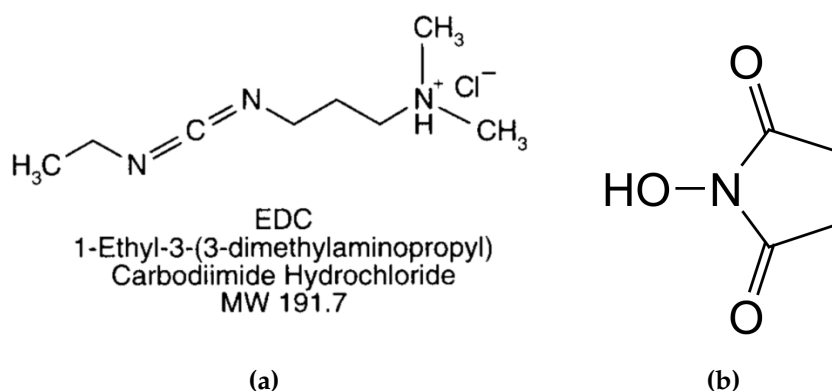


Figure 16: Cross-linker molecules: **a)** 1-Ethyl-3-(3-dimethylaminopropyl) carbodiimide (EDC), and **b)** N-Hydroxysuccinimide (NHS). Figures obtained from references [15, 16].

3.3.2 Covalent binding with carboxyl functionality: EDC/NHS coupling

The covalent conjugation of QDots and molecules appear when there is a reaction of the correspondent functional groups. The most well-studied and easy-to-perform method for attaching QDots together, having a biomolecular shell surrounding them, makes use of the zero-length crosslinker carbodiimide such as EDC. A zero-length crosslinker mediates the conjugation of two molecules by adding no additional atoms [77, 78]. The molecular conjugation can happen by direct formation of an amide bond between amide groups on the QDot, which in this experiment is surrounded with a shell of glutathione, and the carboxyl groups on of another molecule (the EDC molecule). In practice, this chemistry is usually applied in conjunction with the addition of NHS to form a stable active intermediate by converting it in an ester and greatly increase coupling efficiency [78]. This reaction is pH dependent and requires a large excess of EDC due to the latter's extremely rapid competing hydrolysis, i.e., chemical breakdown due to reaction with water.

3.3.3 Chemistry procedure: Inter-particle linking of lead sulfide (PbS) quantum dots via EDC/NHS chemistry

The goal of the chemistry experiments of this report is to perform an inter-particle linking between two quantum dot suspensions. The organic shell on the quantum dots is glutathione (GSH). Via EDC/NHS chemistry the quantum dots are cross-linked. After the activation of the carboxylic acid groups to form the NHS-ester, the ester can nucleophilic attack the amine groups within the glutathione ligand to form the amide. The following experiment protocol here presented was provided by Andreas Schulz MSc and the chemistry experiments were performed, with the essential guidance from Richard Egberink BSc.

CHEMICALS AND QDOT-SUSPENSIONS:

- **A** - PbS-GSH-1100-20 (1072 nm emission max., 10 nmol/L);
- **B** - PbS-GSH-1200-20 (1211 nm emission max., 10 nmol/L);
- **C** - PbS-GSH-1300-20 (1261 nm emission max., 10 nmol/L);
- 1-Ethyl-3-(3-dimethylaminopropyl)carbodiimide (**EDC**), 155.25 g/mol for EDC, and 191.70 g/mol for the Hydrochloride;
- N-Hydroxysuccinimide (**NHS**, 115.09 g/mol).

ANSATZ (EXAMPLE FOR COUPLING OF SUSPENSION A WITH SUSPENSION B)

- $1 \times 100 \text{ }^{-\text{L}}$ of PbS-GSH-1100-20 (1 nmol);
- $1 \times 100 \text{ }^{-\text{L}}$ of PbS-GSH-1200-20 (1 nmol);
- $1 \times 1.9 \text{ mg}$ of EDC;
- $1 \times 1.15 \text{ mg}$ of NHS.

EXPERIMENTAL PROCEDURE From each of the two stock quantum dot suspensions that are used for the coupling, $100 \text{ } \mu\text{L}$ are filled via an Eppendorf-pipette into an Eppendorf-flask ($0.5 \text{ } \mu\text{L}$ total volume capacity). In second flask 1.9 mg of EDC is dissolved in 1 mL degassed milli-Q water and the solution is vortexed until the EDC is completely dissolved. $10 \text{ } \mu\text{L}$ of the EDC solution is added to the flask with the

suspension mixture and is vortexed. In a third flask 1.15 mg of NHS is dissolved and the solution is vortexed until the NHS is completely dissolved. 10 μL of the NHS solution is added to the suspension mixture and is vortexed. The resulting suspension is carefully filled into a $(10 \times 10) \text{ cm}^2$ acrylic cuvette and enclosed with a cuvette cap surrounded by Parafilm.

EXPERIMENTAL RESULTS AND DISCUSSION

To proceed with laboratory experiments, three PbS colloidal QDot samples, bought from the company Mesolight, were used. Each sample was labelled with a corresponding letter, A, B or C. The vendor provided information about the three samples regarding the peak wavelength of the emission spectra and their full width at half maximum (FWHM)¹. These information are given in Table 1, and they serve as a guideline to what to expect from the samples' studies.

Table 1: Info provided by the company Mesolight regarding the emission spectrum peak wavelength and full width at half maximum (FWHM) for each PbS QDot sample used.

	Peak position (nm)	FWHM (nm)
A - Mesolight1071	1071	130
B - Mesolight1211	1211	168
C - Mesolight1261	1261	130

With the obtained samples, several cross-linking experiments were made, using ED-C/NHS coupling, with the method described in Chapter 3.3.3. Using the nomenclature defined in Table 1, the following combined samples were made:

1. A+B
2. A+C
3. B+C
4. B+B

The study of different combinations of QDot samples in cross-linking experiments had the goal to detect the most efficient sample setup for Förster resonance energy transfer

¹ The typical emission spectrum of a well-manufactured QDot sample approximates a Gaussian-shaped curve, resembling the ones presented on Figure 3 of chapter 1.1.

(FRET) studies². Emission spectra³ (presented in Chapter 4.1) and time resolved decay measurements, using TCSPC⁴, (presented in Chapter 4.2) were acquired for samples with and without cross-link chemistry. The cross-linked samples were measured at various QDot aggregation stages, in order to find evidence for FRET in these samples.

4.1 EMISSION SPECTRA

Samples with no cross-linking

The emission spectra of 3 samples of QDots, A, B and C are shown in Figure 17 (see page 61). Information, regarding the used laser average power and the laser repetition rate, is found in the figure. Looking into the spectrum of sample B, i.e., Figure 17b, one clear emission peak is observed. The position of this peak is $\lambda = (1215.300 \pm 0.004) \text{ nm}$ or $\tilde{\nu} = (8228.4 \pm 0.1) \text{ cm}^{-1}$ and the full width at half maximum (FWHM) is $(141 \pm 1) \text{ nm}$. This peak's wavelength and its FWHM are quite similar to the parameters provided in Table 1, thus being in good agreement with the vendor's data, which corresponds to the ground state exciton. Considering these two observations, one can conclude that this sample is in good conditions to proceed cross-linking experiments. Thus, only cross-linked samples based on sample B will be presented, which shall be called as sample B+B. From the spectra of A and C (Figures 17a and 17c respectively), it is noticeable in both spectra the presence of three distinct peaks, which seem to appear in the same position in the frequency spectrum. Recalling the information presented in Table 1, one should have found a single peak for A (at $\lambda = 1071 \text{ nm}$ or $\tilde{\nu} \approx 9337 \text{ cm}^{-1}$) and for C (at $\lambda = 1261 \text{ nm}$ or $\tilde{\nu} \approx 7930 \text{ cm}^{-1}$). Therefore, these spectra do not show the expected behaviour of well-processed QDot samples. Since both spectra A and C are very similar, it is likely that these samples degraded by the time when these experiments were made. Because of this, the study of cross-linking with samples involving samples A and C will not be further discussed, and further cross-linking studies will be focused in sample B. Samples based in the sample B with and without cross-linker will be named as "Only B" and "B+B", respectively, throughout this chapter.

-
- 2 As seen in Chapters 1.3 and 2.4, the necessary condition for FRET is that the donor's emission and acceptor's absorption spectra overlap. The combination of different emission peak wavelength samples in the experiment let us increase the spectral overlap in order to increase FRET efficiency.
 - 3 The technique used for spectra measurements is presented in Chapter 3.2.
 - 4 The Time-Correlated Single Photon Counting technique (TCSPC) is explained in Chapter 3.1 and experimental setup is presented in Chapter 3.2.

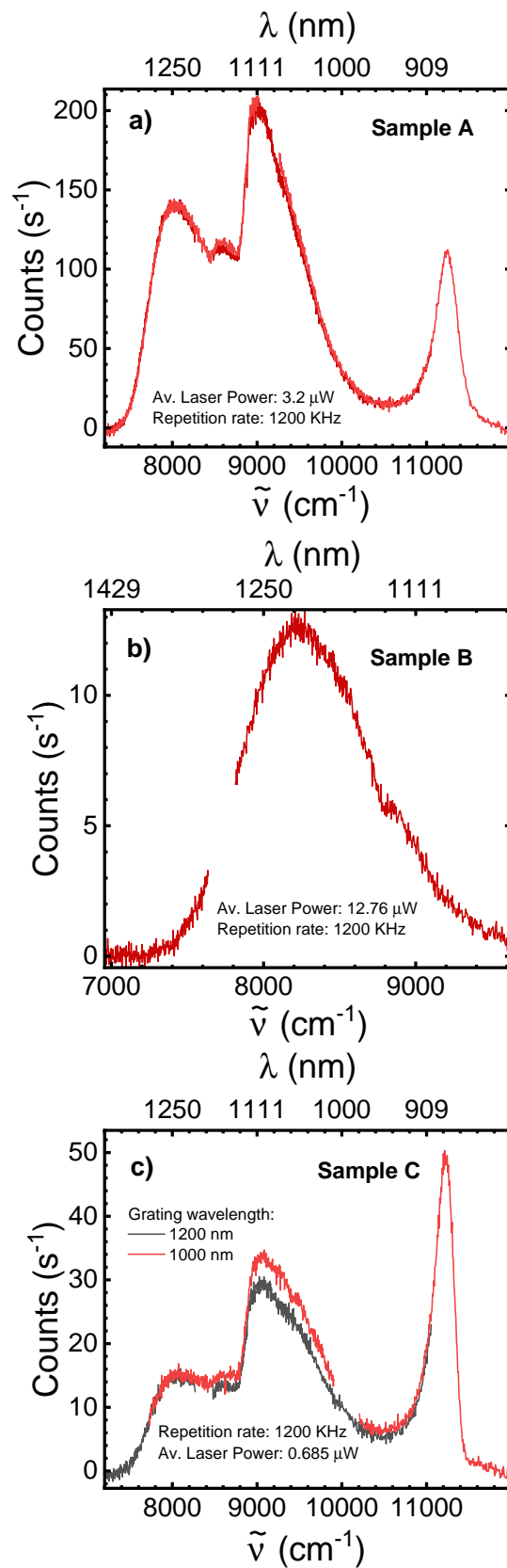


Figure 17: Emission spectra in function of wavenumber, $\tilde{\nu}$, i.e, frequency divided by the speed of light (translated into wavelength, λ , in the top line) of the PbS quantum dot samples studied: **a)** Sample A, **b)** Sample B, **c)** Sample C.

Sample B+B

In Figure 18 (see page 63) emission spectra of a B+B sample (i.e, a sample B with cross-linker), collected at different aggregation times Δt after the start of the binding chemistry, are shown. Two Δt ranges are shown in two distinct graphs - Figure 18a for $\Delta t = [13, 80]$ minutes and Figure 18b for $\Delta t = [80, 900]$ minutes.

Figure 18a shows a consistent decrease in the peak intensity of the spectrum with increasing Δt . Comparing with the trend found in Figure 18b, for Δt higher than 80 minutes, neglecting the spectra for $\Delta t = 900$ minutes, it seems that the emission spectrum of B+B remained stable over the $\Delta t = [80, 114]$ minute range. So, the $\Delta t = [13, 80]$ minute range is of greatest interest.

At $\Delta t = 900$ minutes (see Figure 18b) there is a considerable blue shift of the emission spectrum. The second peak at $\tilde{\nu} \approx 8900 \text{ cm}^{-1}$ becomes the highest emission peak of the spectrum and the overall emission spectra reaches higher counts than before. This may be a sign of sample degradation or secondary effects due to a presumable high QDot agglomeration or even QDot deterioration.

From Figure 18a, it seems that the spectra of the B+B sample got broader for $\Delta t = 80$ minutes, though there is no significant sign of increase of emission for lower wavenumbers. The presence of increasing emission at lower wavenumbers could mean the presence of a non-radiative energy transfer mechanism like FRET, but there is no evidence for such behaviour in these experimental results.

In Figure 19 (see page 64) two spectra of the B+B sample collected at different times Δt are overlapped with the spectrum of sample Only B (i.e, sample B with no cross-linker). Comparing the $\tilde{\nu} = [8200, 9200] \text{ cm}^{-1}$ range, one can find a difference between the spectra accounting for the overall increase in counts for the B+B sample comparing with the Only B sample and a slight increase of the relative intensity of the secondary peak at $\tilde{\nu} \approx 8900 \text{ cm}^{-1}$. For the sample B+B, the main emission peak shows a very slight red-shift, smaller than the length scale of the graph, and a small spectrum broadening for lower frequencies. These very small variations are not reliable to assume a change in QDot behaviour due to the cross-linker. On the other hand, the secondary peak shows a blue-shift with increasing integration time Δt . This shift can be considered as a side effect of the introduction of the cross-linker, due to its interaction with the protecting glutathione cap of the QDots, which could lead to increasing sample deterioration.

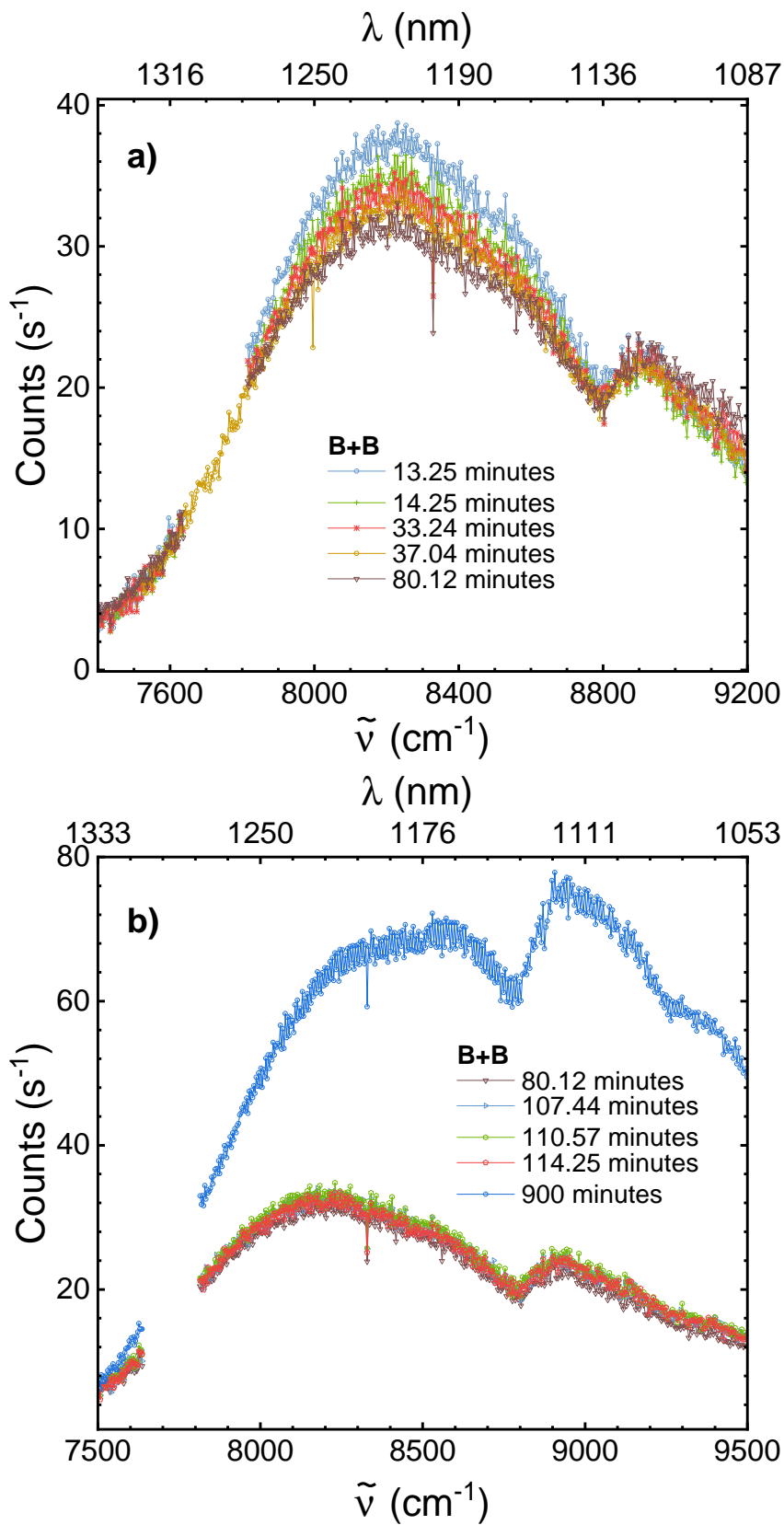


Figure 18: Emission spectra of B+B sample collected at different times Δt after the start of the cross-linking chemistry: a) $\Delta t = [13, 80]$ minutes b) $\Delta t = [80, 900]$ minutes.

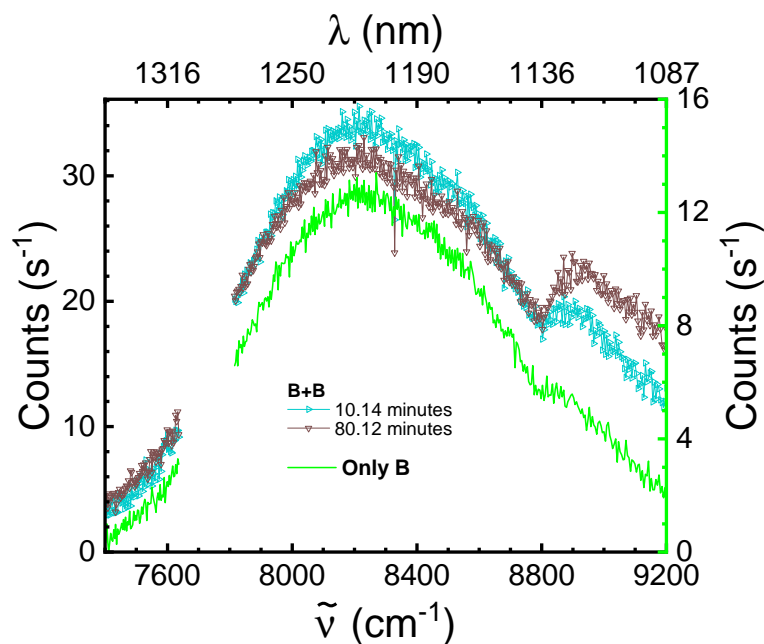


Figure 19: Overlap of B+B Spectra with Sample B with no cross-linking (Only B).

A red-shift in emission spectra could mean an energy transfer related to the FRET mechanism, since it would mean an increasing emission rate from the acceptors, at lower wavenumber, and a luminescence quenching of donors, at higher wavenumber. Figure 20 shows a graph of the wavenumber of the emission peak versus the time Δt , in log-scale. The dashed red lines correspond to the emission peak measured for Only B (See Figure 19), including upper and lower error. For lower Δt the peak wavenumber are in the range of the peak wavenumber of Only B. For higher Δt , the last two data points show a small decrease in peak wavenumber. However, considering the significantly large error bar of the values, arriving from an insufficient signal to noise ratio, the discrepancy is not sufficient to assume a systematic variation and, thus, an evidence of FRET cannot be found with these results.

Concluding, the study of emission spectra shows that the cross-linker did not produce significant and systematic changes in the main emission peak, thus not revealing clear evidences of FRET, in the studied sample. On the other hand, it is observed that the introduction of the cross-linker increases the sample deterioration, increasingly observed for longer aggregation time at higher wavenumbers.

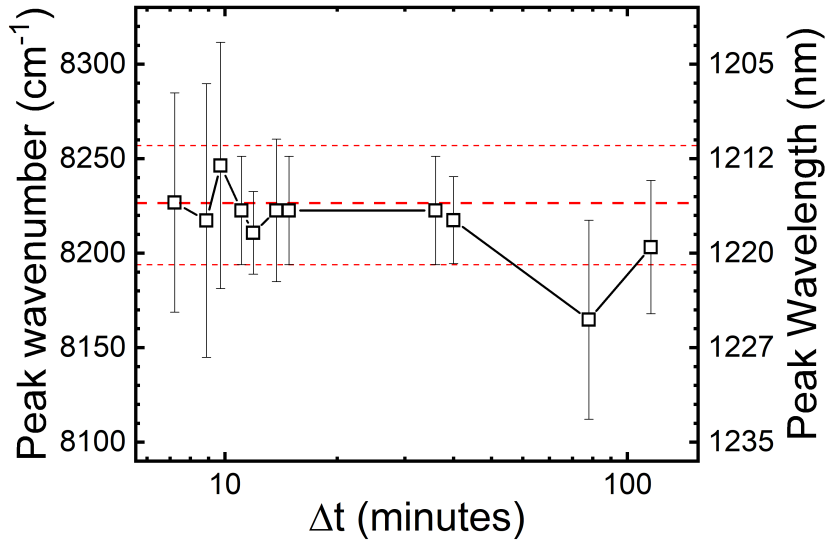


Figure 20: Peak of B+B sample versus time Δt after the start of the cross-linking chemistry. The dashed red lines correspond to the position of the emission peak measured for sample B with no cross-linking - Only B (See Figure 19), including upper and lower error.

4.2 TIME-RESOLVED DECAY: DATA FITTING WITH THEORETICAL DECAY FUNCTIONS

The decay rate observed in photoluminescence kinetics, the type of time-resolved measurements here presented, is related to the total decay rate, which involves all known decay mechanisms of the system [74]. For the cross-linked samples, the FRET decay mechanism, Γ_{FRET} , is a relevant contribution for the total decay rate. Recalling Equation 1.3 from Chapter 1.3, the total decay rate Γ can be written as the sum:

$$\Gamma = \Gamma_{\text{FRET}} + \Gamma_{\text{rad}} + \Gamma_{\text{nr}}, \quad (4.1)$$

and the efficiency for FRET, η_{FRET} , can be written as:

$$\eta_{\text{FRET}} = \frac{\Gamma_{\text{FRET}}}{\Gamma_{\text{FRET}} + \Gamma_{\text{rad}} + \Gamma_{\text{nr}}} = 1 - \frac{\Gamma_{\text{D}}}{\Gamma_{\text{DA}}} \quad (4.2)$$

where Γ_{DA} is the total decay rate of the donor-acceptor sample (here, the cross-linked QDot sample B+B) and Γ_{D} is the total decay rate of the only donor sample (here, the non cross-linked QDot sample Only B), and

$$\Gamma_{\text{FRET}} = \Gamma_{\text{DA}} - \Gamma_{\text{D}}. \quad (4.3)$$

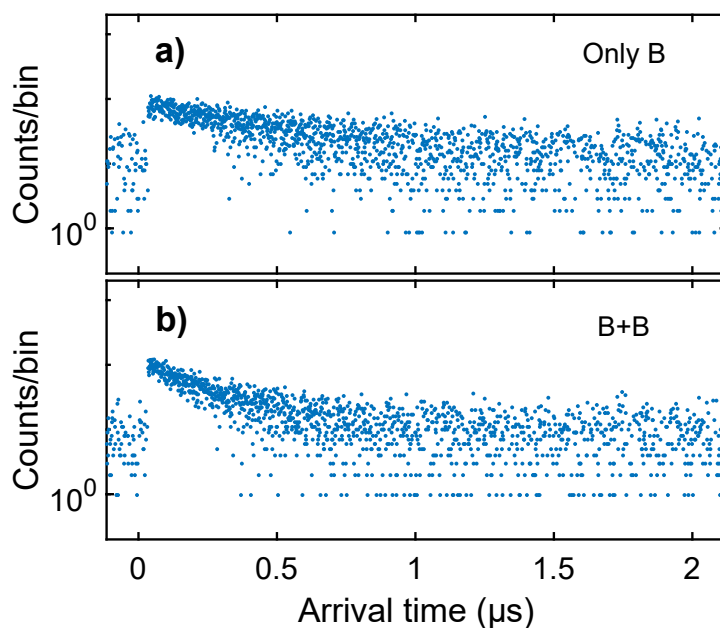


Figure 21: Comparison between experimental photoluminescence kinetics from: **a)** Sample Only B (with no cross-linker), and **b)** Sample B+B (with cross-linker). The y axis, representing the number of single photon counts per bin, is set in the logarithmic scale. Both kinetics were detected at the light wavenumber $\tilde{\nu} = 8333 \text{ cm}^{-1}$.

In order to study the decay rate of the samples Only B (sample B without cross-linker) and B+B (sample B with cross-linker), time-resolved measurements, using the TCSPC technique, were performed. Data were acquired for various wavenumbers $\tilde{\nu}$, close to the emission peak wavenumber of the samples.

A first qualitative study can be done by comparing side-by-side the experimental photoluminescence kinetics of a non-cross-linked QDot sample with a cross-linked one. In Figure 21 it is presented a comparison between the photoluminescence kinetics of sample Only B and sample B+B for the wavenumber $\tilde{\nu} = 8333 \text{ cm}^{-1}$, where the y axis, representing the number of single photon counts per bin, is set in the logarithmic scale. Between the arrival times $0\mu\text{s}$ and $1\mu\text{s}$, it is visible that sample B+B decays faster than sample Only B, at an apparent non-exponential rate. This observation shows that the QDot cross-linking is producing a change in the decay channels for the studied samples, changing an exponential-shaped decay curve into a non-exponential one, and it can be related to a possible presence of a FRET mechanism.

To yield a systematic study of the data, all experimental kinetics were adjusted with a log-normal distribution decay function, using equation 2.104 of Chapter 2.6.2, and a homogeneous acceptor distribution decay function, equation 2.93 of Chapter 2.5.1.

The study of FRET efficiency with the obtained fitting results, by using equation 4.2, lets us find possible evidence of FRET in the cross-linked QDot samples.

4.2.1 Log-normal distribution of decay rates function

Retrieving from Chapter 2.6.2, the log-normal distribution of decay rates decay function, $I_{LN}(t)$, is given by

$$I_{LN}(t) = A \int_0^{\infty} d\Gamma \exp \left[-\frac{\ln^2(\Gamma/\Gamma_{mf})}{\omega^2} - \Gamma t \right] \quad (4.4)$$

where A is a normalization constant, Γ_{mf} is the most frequent decay rate and ω is the dimensionless width parameter which is related to the width of the distribution as its $1/e$ height $\Delta\Gamma$ via:

$$\Delta\Gamma = 2\Gamma_{mf} \sinh(\omega). \quad (4.5)$$

A custom Matlab fitting program was produced in order to find values of A , Γ_{mf} and $\Delta\Gamma$ which match best the experimental kinetics.

In Figure 22 (see page 68) two time-resolved histograms of the number of photon counts in function of the arrival time for the sample B+B are shown, each at different wavenumbers. For $\tilde{\nu} = 8333 \text{ cm}^{-1}$ (Figure 22a) the log-normal distribution matches rather well. At $\tilde{\nu} = 9091 \text{ cm}^{-1}$ (Figure 22b), the model also matches well and the obtained width $\Delta\Gamma$ is very large since the decay is strongly non-exponential. It should be noted that in the emission spectra of B+B (see Figure 18) the secondary peak lies close to the wavelength $\tilde{\nu} = 9091 \text{ cm}^{-1}$. So, one can conclude that this secondary peak doesn't come from well behaved quantum dots.

Regarding the parameters found from the fits in Figure 22 we only consider the range of wavenumbers under $\tilde{\nu} = 9091 \text{ cm}^{-1}$ to avoid complications from the secondary peak. In Figure 23a (see page 69) we plot the most frequent decay rate, Γ_{mf} , as a function of wavenumber, $\tilde{\nu}$, for three different time-spans Δt , i.e. different QDot aggregation stages. These results are compared with the behaviour of the sample Only B. It is observed an overall systematic increase of Γ_{mf} for the cross-linked B+B sample comparing with Only B, as well as an observable trend of increase of the overall decay

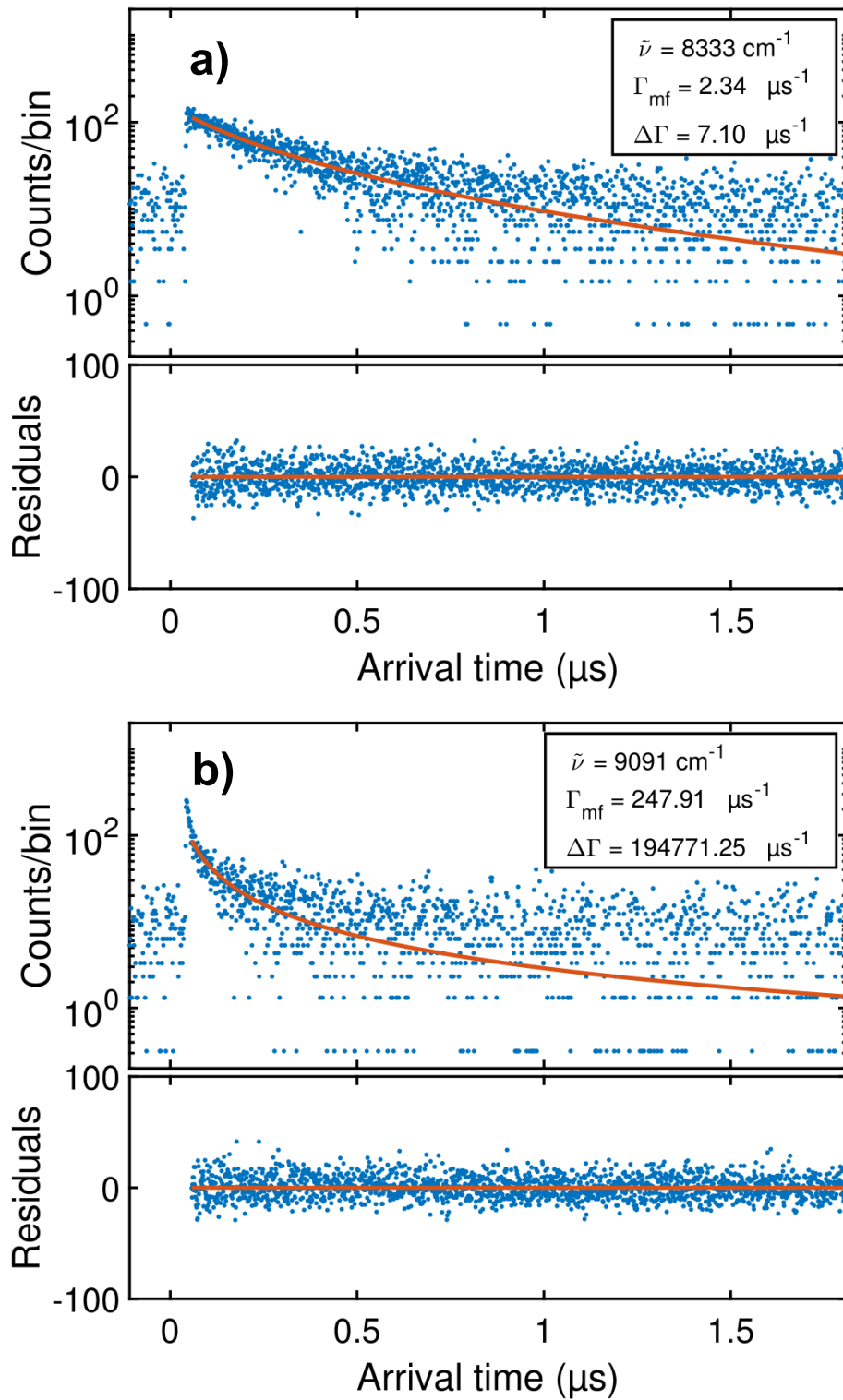


Figure 22: Time correlated measurements of sample B+B for two different wavenumbers: **a)** $\tilde{\nu} = 8333 \text{ cm}^{-1}$ ($\lambda = 1200\text{nm}$) ($\chi^2 \approx 1.04$), **b)** $\tilde{\nu} = 9091 \text{ cm}^{-1}$ ($\lambda = 1100\text{nm}$) ($\chi^2 \approx 1.02$). Log-normal distributions are fitted with red lines.

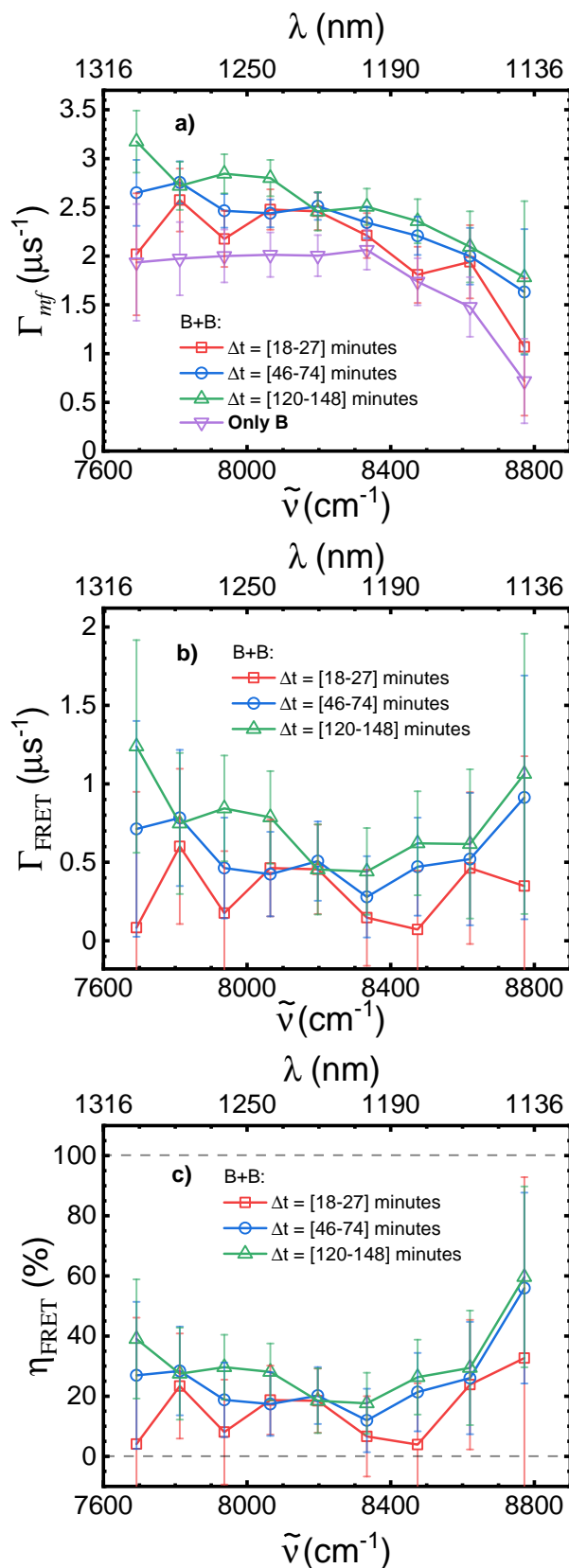


Figure 23: Results from the fitting of the log-normal distribution decay function in kinetics of sample B+B, in function of light wavenumber $\tilde{\nu}$ for three different QDot aggregation stages Δt : **a)** Most frequent decay rate, Γ_{mf} . Here it is compared the behaviour of sample B+B with the sample Only B (in purple); **b)** Measured FRET decay rate, Γ_{FRET} ; **c)** Measured efficiency of FRET, η_{FRET} . The grey horizontal dashed lines indicate the upper and lower bounds of η_{FRET} .

rate for consecutive aggregation stages ⁵. One must carefully argue the nature of this difference between the sample B+B and the sample Only B. The study of FRET decay rate and FRET efficiency, using equations 4.2 and 4.3, helps us understand the experimental data.

In Figures 23b and 23c the FRET rate, Γ_{FRET} , and the FRET efficiency, η_{FRET} , are plotted in function of light wavenumber $\tilde{\nu}$, respectively. Most of the obtained values of Γ_{FRET} range approximately between $0\mu\text{s}^{-1} < \Gamma_{\text{FRET}} < 1\mu\text{s}^{-1}$, and most of the calculated values of η_{FRET} lie over the range of $0 < \eta_{\text{FRET}} < 40\%$. The obtained results show evidences of FRET on the cross-linked samples. They also show, from efficiency results, that FRET efficiency is higher for increasing light wavenumber, which agrees with the idea that FRET occurs from small QDots to big QDots. There is also a noticeable average increase of η_{FRET} with increasing number of acceptors for a single donor aggregation time, Δt , which can indicate that there is a increase acceptors due to increasing QDot aggregation. However, the considerable data upper bound errors, does not let us picture a very clear and precise description of the system. By fitting the data with another decay function one might achieve better results.

4.2.2 Homogeneous acceptor distribution decay function

The homogeneous acceptor distribution decay function is derived in Chapter 2.5.1 by assuming an homogeneous 3D distribution of acceptor QDots in a colloidal sample. It is derived as:

$$\begin{aligned} I_{\text{D}}(t) &= I_0 \exp\left(-\Gamma t - \frac{4}{3}\pi^{3/2}C_0R_0^3(\Gamma t)^{1/2}\right), \\ &= I_0 \exp\left\{-\left(\Gamma t\right)^{1/2}\left[\left(\Gamma t\right)^{1/2} + \sqrt{\pi}N_0\right]\right\}, \end{aligned} \quad (4.6)$$

where Γ is the sample decay rate and $N_0 = 4/3\pi R_0^3 C_0$ is interpreted as the number of acceptors inside a Förster sphere of radius R_0 . A custom Matlab fitting program was produced in order to find values of Γ and N_0 which suit best the experimental

⁵ From Figure 23a it is also observed that the decay rate Γ_{mf} is inversely proportional to the light wavenumber $\tilde{\nu}$, as seen with other experiments with lead chalcogenide QDots [13, 42]. This trend goes against Fermi's golden rule, which predicts a proportional relation. The origin of this phenomenon is undetermined, although one may suggest that the trend can come from complex trap states of the QDots.

kinetics⁶.

In Figure 24 two examples of fitted kinetics for the sample B+B can be found. Figure 24a presents a kinetics fit for light wavenumber $\tilde{\nu} = 8333\text{cm}^{-1}$ and Figure 24b presents a kinetics fit for $\tilde{\nu} = 9091\text{cm}^{-1}$. As shown with the fitting with a log-normal distribution in Figure 22 of Chapter 4.2.1, the fitting with the stretched exponential was unsuccessful for $\tilde{\nu} = 9091\text{cm}^{-1}$, since the error values for Γ and N_0 are higher than the values themselves. Regarding the fitting of the kinetics for $\tilde{\nu} = 8333\text{cm}^{-1}$ (Figure 24a), the fitting of the homogeneous distribution was well implemented, yielding normal values of Γ and N_0 . The same was found over the range of wavenumbers below $\tilde{\nu} = 9091\text{cm}^{-1}$ in the four experiments shown in this work.

The four data sets in comparison are the three measurements of sample B+B at different aggregation times Δt and sample Only B, which results of kinetic fit of decay parameters Γ and N_0 , in function of light wavenumber $\tilde{\nu}$, are presented in Figures 25a and 25b, respectively. First analysing the decay rate results (Figure 25a), the Only B sample, i.e, the purple dotted line, shows consistent smaller values of the decay rate in comparison with the B+B sample at different aggregation times in the range of smaller wavenumbers $\tilde{\nu} =]7692, 8196[\text{cm}^{-1}$, while the opposite is observed in the range of higher wavenumbers $\tilde{\nu} = [8333, 8772] \text{cm}^{-1}$. This change may indicate a change of behaviour of the cross-linked QDots (B+B sample) for higher light wavenumbers.

Plotting the FRET decay rate and FRET efficiency (Figures 25c and 25d, respectively), one observes that, for the region of higher wavenumbers, both Γ_{FRET} and η_{FRET} yield negative values. These values do not hold physical meaning, since there negative values are not defined for FRET. On the other hand, the region for smaller wavenumbers $\tilde{\nu} =]7692, 8196[\text{cm}^{-1}$ has positive Γ_{FRET} and η_{FRET} throughout its range. This may indicate the sample B+B is well behaved only for lower wavenumbers.

It is observed that there is a decreasing of Γ_{FRET} and η_{FRET} with increasing wavenumber. Since FRET efficiency is expected to be higher for higher energy QDots, this result is difficult to interpret. On another hand, values of N_0 for the same wavenumber range (Figure 25b) imply that the number of available acceptors for FRET in a single donor increases with increasing wavenumber. This way, there is a observable contradiction between the results of Figures 25b and 25d, and thus, no clear image of FRET is presented.

⁶ The Matlab code used for fitting the homogeneous acceptor distribution decay function is presented in Appendix C.1.

In conclusion, the results presented throughout this chapter hold interpretation struggles and, therefore, are not conclusive. Firstly, the emission spectra of cross-linked QDots has been shown to lack relevant differences comparing with the emission spectra of non-cross-linked QDots. Secondly, the fitting of theoretical decay curves into photoluminescence kinetics has showed to hold technical issues, mainly regarding the adjustment of the decay curves. Here, the fitting of log-normal distribution function yielded different results, although with greater error, to the ones presented with the fitting of the homogeneous acceptor distribution function. This analysis shows that the fitting of the homogeneous acceptor distribution decay function holds interpretation struggles, however it fitted parameters Γ and N_0 with average lower error than with the log-normal distribution. The study of FRET efficiency has shown an evidence of FRET in the studied samples using the log-normal distribution, however the obtained results hold considerable error fluctuation. An alternative (statistical) analysis is presented on Chapter 5.

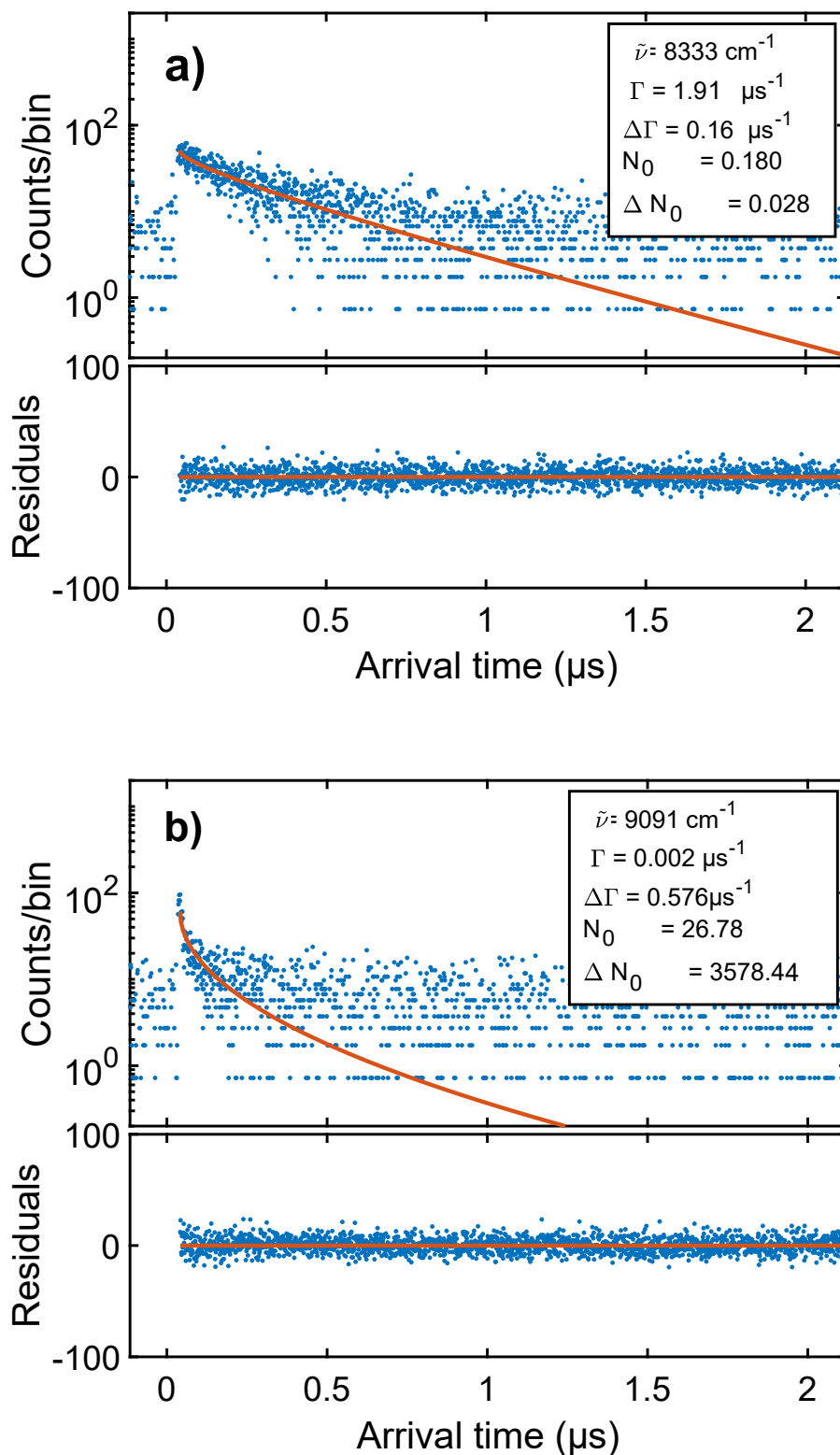


Figure 24: Time correlated measurements of sample B+B for two different wavenumbers: **a)** $\tilde{\nu} = 8333 \text{ cm}^{-1}$ ($\lambda = 1200\text{nm}$) ($\chi^2 \approx 1.03$), **b)** $\tilde{\nu} = 9091 \text{ cm}^{-1}$ ($\lambda = 1100\text{nm}$). Homogeneous distribution decay functions are fitted with red lines. A graph of the residuals of the data fit is shown.

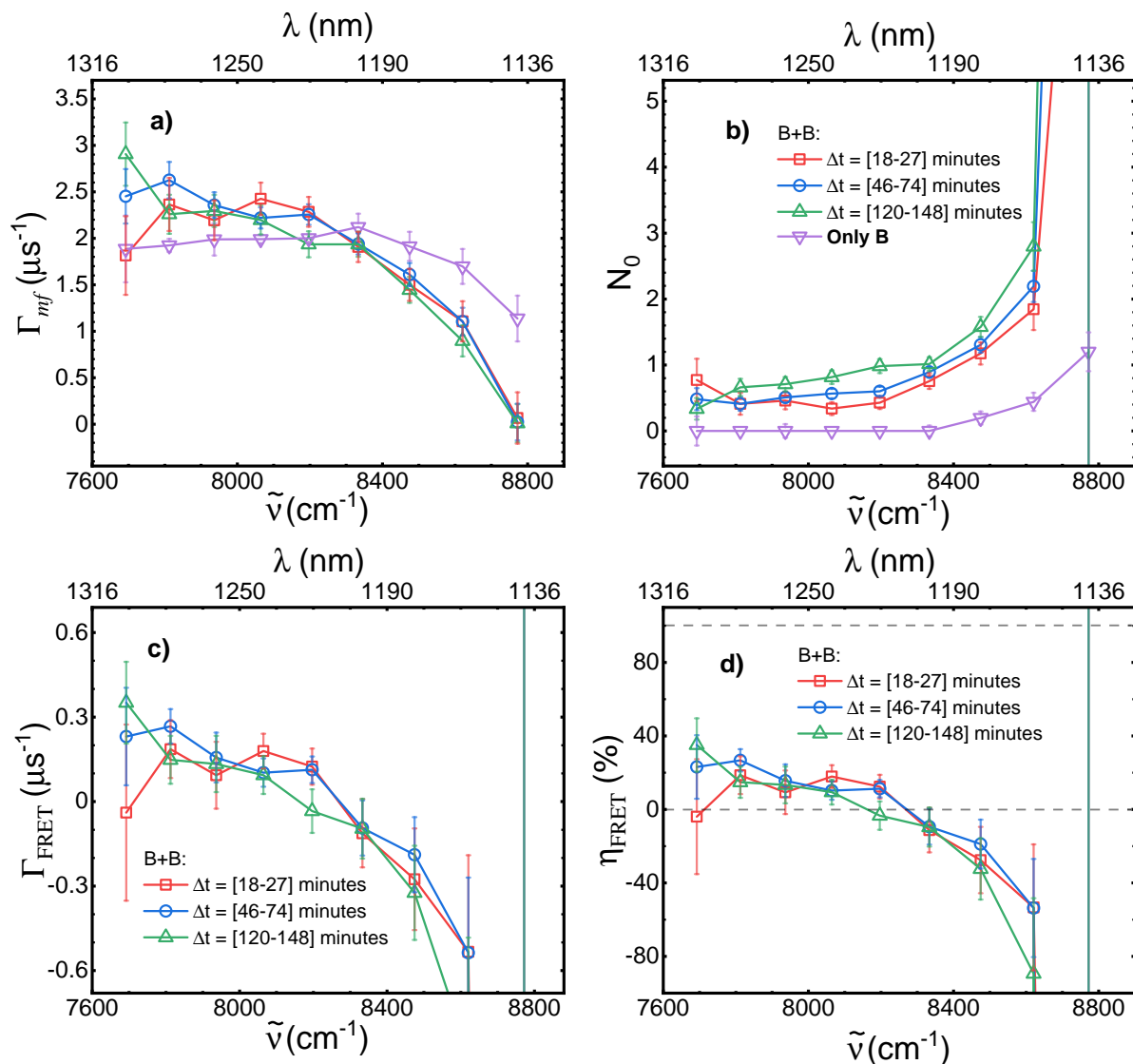


Figure 25: Results from the fitting of the homogenous acceptor distribution decay function in kinetics of sample B+B, in function of light wavenumber $\tilde{\nu}$ for three different QDot aggregation stages Δt : **a)** Most frequent decay rate, Γ_{mf} . Here it is compared the behaviour of sample B+B with the sample Only B (in purple); **b)** Number of acceptor QDots N_0 , inside a sphere of radius R_0 ; **c)** Measured FRET decay rate, Γ_{FRET} ; **d)** Measured efficiency of FRET, η_{FRET} . The grey horizontal dashed lines indicate the upper and lower bounds of η_{FRET} .

STATISTICAL MOMENTS OF QUANTUM DOTS IN PHOTOLUMINESCENCE KINETICS

From the results obtained by fitting a theoretical decay function into experimental photoluminescence kinetics, it has been concluded that the reliability of such fitting is low, for this experimental work; thus no clear evidence of the FRET mechanism has been obtained. As an alternative approach, we shall compare the statistical moments of the photoluminescence decays. The statistical moment of order n is given as:

$$\langle t^n \rangle \equiv \frac{\int_0^\infty f(t) t^n dt}{\int_0^\infty f(t) dt}, \quad (5.1)$$

where $f(t)$ is the measured decay histogram and n must be a positive integer. The first moment $\langle t \rangle$ is known as the average decay time, the second order $\langle t^2 \rangle$ is the mean square-value of the decay, which is related to the second central moment, or variance D , $D = \langle t^2 \rangle - \langle t \rangle^2$ [79]. The third momentum, $\langle t^3 \rangle$, is described as the measure of the skewness, i.e, the measure of asymmetry of the time-resolved distribution, and the fourth moment, $\langle t^4 \rangle$, is interpreted as the kurtosis, i.e, the measure of heaviness of the tail of the distribution compared to the normal distribution of the same variance [80]. Higher order moments are harder to interpret, but they give description of other shape parameters. By studying the moments of the photoluminescence kinetics and finding correlation with the moments of known theoretical decay curves one can attain a more detailed knowledge of the way QDots bind together.

5.1 STATISTICAL MOMENTS OF THEORETICAL DECAY FUNCTIONS

First, a study of the statistical moments of the known analytical decay functions is required, in order to draw a physical intuition of the experimental results. In this

section some of the decay functions discussed throughout this thesis are analysed, namely: the single-exponential function, the homogeneous distribution decay function, the fixed-shell distribution decay function, and the log-normal distribution decay function¹. A relevant quantity to study is the ratio between different moments R_n , defined as:

$$R_n \equiv \frac{\langle t^n \rangle / \langle t^{n-1} \rangle}{\langle t^{n-1} \rangle / \langle t^{n-2} \rangle} = \frac{\langle t^n \rangle \langle t^{n-2} \rangle}{\langle t^{n-1} \rangle^2}, \quad (5.2)$$

where n , $n - 1$ and $n - 2$ are required to be non-negative integers. As will be seen below, this ratio gives a simple trend for each of the mentioned theoretical decay functions, and it will be the main function studied during the hole chapter.

5.1.1 Single exponential function

For the single exponential function ($f(t) = \exp(-t/\tau_D)$), the moment of order n is given by:

$$\begin{aligned} \langle t^n \rangle &= \frac{\int_0^\infty dt \exp\left(-\frac{t}{\tau_D}\right) t^n}{\int_0^\infty dt \exp\left(-\frac{t}{\tau_D}\right)} \\ &= \tau_D^n n! \end{aligned} \quad (5.3)$$

By using equation 5.2, the ratio R_n is simply given by

$$R_n = \frac{n}{n-1}. \quad (5.4)$$

The red line in Figure 26 represents graphically the behaviour of equation 5.4, i.e, the values of R_n in the range $n \in [2, +\infty[$, where n is as a positive integer. In this range, one easily finds that the values of R_n are in the range $R_n \in [2, 1[$, with an asymptote at $R_n = 1$. This result shows that the function R_n for the single-exponential function depends only on the order n , and it does not depend on the decay time, τ_D . Thus, any time-resolved data which is well described by a single-exponential function must show a behaviour of R_n similar to Figure 26.

¹ The homogeneous distribution and fixed-shell distribution decay functions are derived in Chapter 2.5, and the single exponential and log-normal distribution decay functions are presented in Chapter 2.6.2.

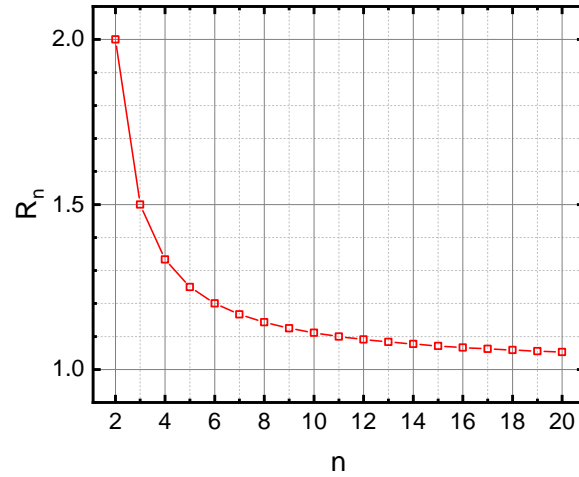


Figure 26: Ratio of moments R_n for the single exponential function.

5.1.2 Homogeneous distribution decay function

In Chapter 2.5.1 a decay function for which it assumes a homogeneous spatial distribution of acceptors around a donor was derived:

$$I(t) = I_0 \exp \left[-\frac{t}{\tau_D} - \sqrt{\pi} N_0 \left(\frac{t}{\tau_D} \right)^{1/2} \right],$$

where N_0 is the number of acceptors in a sphere of Förster radius R_0 and I_0 is the amplitude of the function. This expression is similar to the one found in the literature, known as the stretched-exponential function, with fixed $\beta = 1/2$ (see Chapter 2.6). The moment of order n , $\langle t^n \rangle$ is given by:

$$\langle t^n \rangle = \frac{\int_0^\infty dt \exp \left[-\left(\frac{t}{\tau_D} \right) - \sqrt{\pi} N_0 \left(\frac{t}{\tau_D} \right)^{1/2} \right] t^n}{\int_0^\infty dt \exp \left[-\left(\frac{t}{\tau_D} \right) - \sqrt{\pi} N_0 \left(\frac{t}{\tau_D} \right)^{1/2} \right]}. \quad (5.5)$$

Analysing the integral in the nominator in equation 5.5 (here it is assumed $P = \sqrt{\pi} N_0$):

$$\begin{aligned}
& \int_0^\infty dt \exp \left[- \left(\frac{t}{\tau_D} \right) - P \left(\frac{t}{\tau_D} \right)^{1/2} \right] t^n \\
&= \exp \left(\frac{P^2}{4} \right) \int_0^\infty dt \exp \left\{ - \left[\left(\frac{t}{\tau_D} \right)^{1/2} + \frac{P}{2} \right]^2 + \frac{P^2}{4} \right\} t^n \\
&= 2\tau_D^{n+1} \exp \left(\frac{P^2}{4} \right) \int_{P/2}^\infty du \left(u - \frac{P}{2} \right)^{2n+1} \exp(-u^2) \\
&= 2^{2n-1} \Gamma(2n+2) U \left(n+1, \frac{1}{2}, \frac{P^2}{4} \right),
\end{aligned}$$

where the substitution $u = (t/\tau_D)^{1/2} + P/2$ was used, $\Gamma(z)$ is the Euler gamma function and $U(a, b, z)$ is the confluent hypergeometric function [81]. Since the denominator of equation 5.5 is the same for $\langle t^n \rangle$, $\langle t^{n-1} \rangle$ and $\langle t^{n-2} \rangle$, the ratio R_n for the homogeneous distribution decay function is simply given by:

$$R_n(N_0) = \frac{\Gamma(2n-2)\Gamma(2n+2) U \left(n-1, \frac{1}{2}, \frac{(\sqrt{\pi}N_0)^2}{4} \right) U \left(n+1, \frac{1}{2}, \frac{(\sqrt{\pi}N_0)^2}{4} \right)}{\Gamma(2n)^2 U \left(n, \frac{1}{2}, \frac{(\sqrt{\pi}N_0)^2}{4} \right)^2} \quad (5.6)$$

This equation can be simplified further noting that the Euler gamma function $\Gamma(s)$, where s is a positive integer, can be written as $\Gamma(s) = (s-1)!$. Thus, the ratio R_n is rewritten as

$$R_n(N_0) = \left[\left(1 + \frac{2}{2n-1} \right) \frac{U \left(n-1, \frac{1}{2}, \frac{(\sqrt{\pi}N_0)^2}{4} \right) U \left(n+1, \frac{1}{2}, \frac{(\sqrt{\pi}N_0)^2}{4} \right)}{U \left(n, \frac{1}{2}, \frac{(\sqrt{\pi}N_0)^2}{4} \right)^2} \right] \frac{n}{n-1}. \quad (5.7)$$

As for the single-exponential function, the quantity R_n for this decay function does not depend on the decay time τ_D . On the other hand, this function depends on the variable N_0 , related with the number of acceptors in a sphere of Förster radius R_0 . The ratio R_n for the homogeneous distribution function is proportional to the ratio R_n of the single exponential, equation 5.4, and for $N_0 = 0$ the R_n ratio coincides with that for the single exponential function. Since the confluent hypergeometric function

is a complicated function to analytically interpret, numerical calculations were used to understand the influence of the variable N_0 on the quantity R_n . In Figure 27a and Figure 27b (see page 81) one can observe that the increase of N_0 leads to a stretch of the function R_n . However, the stretch saturates for values higher than $N_0 = 30$.

5.1.3 Fixed-Shell distribution decay function

In Chapter 2.5.2, a decay function which assumes a distribution of acceptors on a fixed-radius shell around a donor was derived:

$$\begin{aligned} I_D(t) &= I_0 \exp \left\{ -\frac{t}{\tau_D} - N_0 \left(\frac{R_0}{a} \right)^{-3} \left[1 - \exp \left[- \left(\frac{R_0}{a} \right)^6 \frac{t}{\tau_D} \right] \right] \right\} \\ &= I_0 \exp \left\{ -\Gamma t - N_0 \alpha^{-3} \left[1 - e^{-\alpha^6 \Gamma t} \right] \right\}, \end{aligned}$$

where N_0 again is the number of acceptors in a sphere of Förster radius R_0 , a is the radius of the acceptor shell, $\Gamma = 1/\tau_D$ and $\alpha = R_0/a$. In this model, since the variable α is dependent of the ratio between R_0 and a , the experimental data fitting and the study of statistical moments with this function can directly determine the average interaction distance between a donor and a acceptor in a sample.

The statistical moment of order n for this function is given by:

$$\langle t^n \rangle = \frac{\int_0^\infty dt t^n \exp \left\{ -\Gamma t - N_0 \alpha^{-3} \left[1 - e^{-\alpha^6 \Gamma t} \right] \right\}}{\int_0^\infty dt \exp \left\{ -\Gamma t - N_0 \alpha^{-3} \left[1 - e^{-\alpha^6 \Gamma t} \right] \right\}}. \quad (5.8)$$

The integral in the nominator cannot be calculated analytically. Therefore, numerical integration was used by setting certain values of the constants Γ , N_0 and α , in order to study the ratio of moments R_n . Let us study each parameter mentioned, in order to understand its influence on equation 5.8.

In Figures 27c and 27d (see page 81), the ratio of moments R_n for varying number of acceptors N_0 , from $N_0 = 0$ to $N_0 = 40$, is plotted. Other parameters remained constant, $\alpha = 1$ and $\Gamma = 2 \mu s^{-1}$ ². For $N_0 = 0$ one observes that the R_n coincides with that for the single exponential function, as it is expected for a QDot system with no acceptors. For $N_0 \leq 5$ (see Figure 27c) the left tail of the function increases

² The value of $\Gamma = 2 \mu s^{-1}$ is close to the decay rate of PbS QDots, thus it was the value chosen to test the function. For the obtained values of Γ see Figure 23a and Figure 25a in Chapter 4.2.

exponentially with the increase of N_0 , whereas the right hand side of the function, that is, for $n \geq 8$ does not vary considerably. Direct comparison with the homogeneous distribution function can be made by looking at Figure 27a, where one can observe that there is an overall increase of R_n with increasing N_0 . For $N_0 > 5$, a peak emerges, lying over higher values of n and with increasing amplitude, by the increase of N_0 . Its behaviour is considerably different from the R_n function for the homogeneous acceptor distribution decay function, for the same values of N_0 (see Figure 27b).

In order to study the α parameter influence, the variation of R_2 with varying α was calculated. In Figure 28 it can be seen that R_2 has a sharp peak around $\alpha \approx 1$. To the same end, relevant data, which can show intense presence of FRET, should lie around values of $\alpha = 1$ (remember that $\alpha = R_0/a$, where a is the distance between a donor and a acceptor QDot). Therefore, with this conclusion, the R_n function has been studied for values around $\alpha = 1$.

In Figure 29 graphs of the ratio of moments R_n for different values of $\alpha \in [0.80, 1.20]$, with fixed N_0 and $\Gamma = 2\mu s^{-1}$ for each graph, are plotted. It can be seen that the change of α yields different results for different values of N_0 . For $N_0 = 5$, (see Figure 29a and Figure 29b) the change of α leads to a change of the left tail of the function. On the other hand, for $N_0 = 10$ and $N_0 = 20$ (Figures 29c, 29d, 29e and 29f), the value of α determines the position and the amplitude of the emerged peak of R_n for intermediate values of n . For higher values of α , the peak position lies at lower values of n and the peak amplitude is increased.

Concluding, the parameters N_0 and α both influence the R_n function for the shell distribution in terms of the amplitude and peak position. However, the increase of α leads to an inverse effect compared to that of N_0 , in terms of peak position. A careful choice of the values of α and N_0 is required to fit experimental data. Notice that this R_n is independent of the decay rate Γ ³.

5.1.4 Log-normal distribution decay function

The theoretical decay curve of the log-normal distribution is the following:

$$f(t) = \int_0^\infty d\Gamma \exp\left(-\frac{\ln^2(\Gamma/\Gamma_{mf})}{\omega^2}\right) \exp(-\Gamma t), \quad (5.9)$$

³ Such observation comes from several trial numerical calculations performed with different values of Γ .

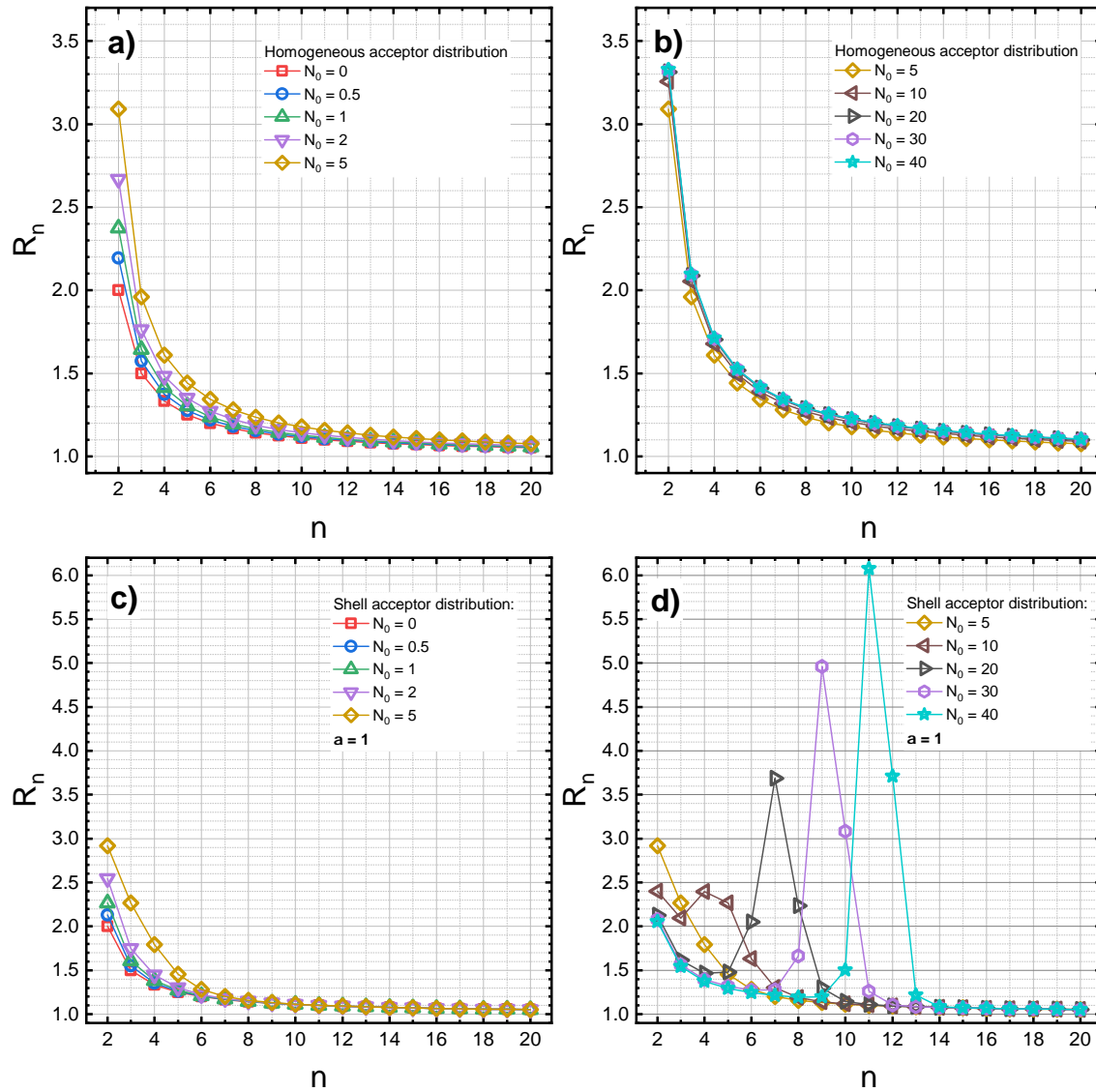


Figure 27: Ratio of moments R_n , with varying number of acceptors N_0 inside a sphere of Förster radius R_0 , for two theoretical acceptor distributions: the homogeneous and fixed-shell ones.

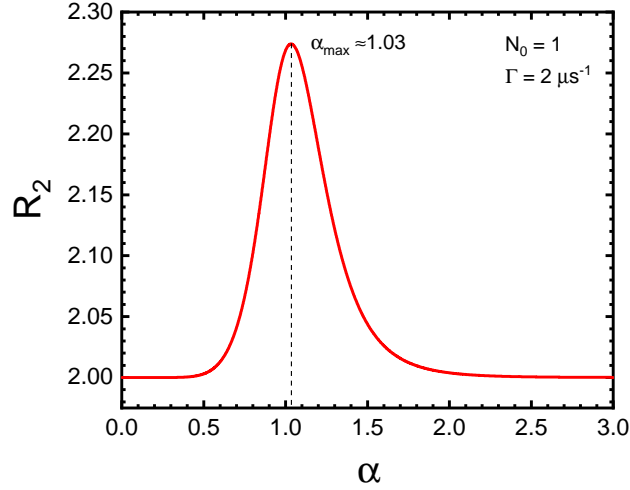


Figure 28: Variation of the ratio of moments R_2 in function of the parameter α , with $N_0 = 1$ and $\Gamma = 2\mu\text{s}^{-1}$.

where the integral is over different decay rates Γ and Γ_{mf} is the most frequent decay rate. The equation for the n -th order statistical moment of the log-normal distribution is:

$$\langle t^n \rangle = \frac{\int_0^\infty d\Gamma \exp\left(-\frac{\ln^2(\Gamma/\Gamma_{mf})}{\omega^2}\right) \left[\int_0^\infty dt \exp(-\Gamma t) t^n \right]}{\int_0^\infty d\Gamma \exp\left(-\frac{\ln^2(\Gamma/\Gamma_{mf})}{\omega^2}\right) \left[\int_0^\infty dt \exp(-\Gamma t) \right]}. \quad (5.10)$$

The integrals in the denominator of equation 5.10 give the following result:

$$\begin{aligned} \int_0^\infty d\Gamma \exp\left(-\frac{\ln^2(\Gamma/\Gamma_{mf})}{\omega^2}\right) \left[\int_0^\infty dt \exp(-\Gamma t) \right] &= \int_0^\infty d\Gamma \exp\left(-\frac{\ln^2(\Gamma/\Gamma_{mf})}{\omega^2}\right) \cdot \frac{1}{\Gamma} \\ &= \int_{-\infty}^{+\infty} dx \exp\left(-\frac{x^2}{\omega^2}\right) \\ &= \omega\sqrt{\pi} \end{aligned}$$

where, in the second step of the derivation, the change of variable $x = \ln(\Gamma/\Gamma_{mf})$ was performed. The integrals in the nominator yield:

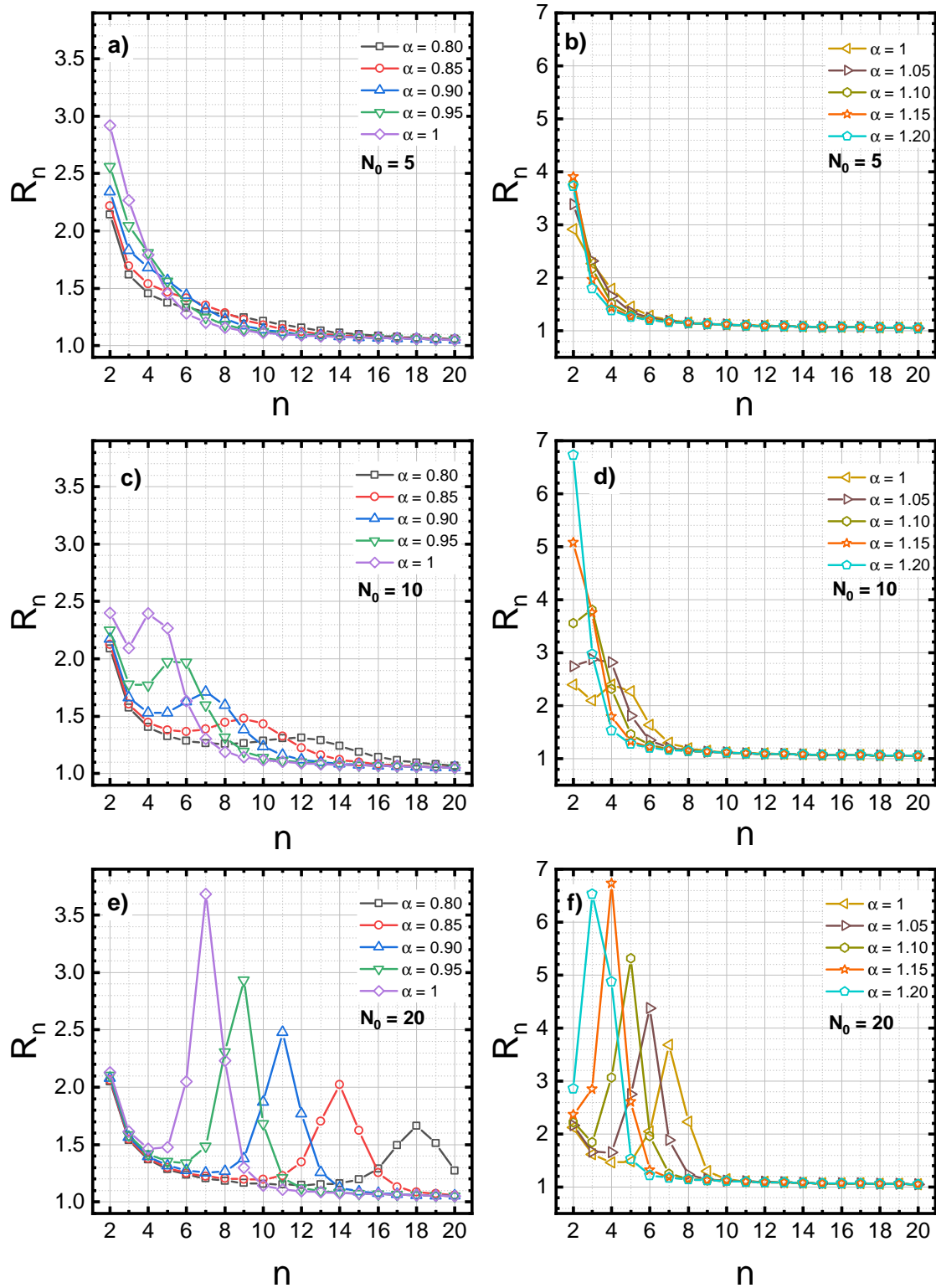


Figure 29: Ratio of moments R_n for the fixed-shell distribution decay function, for values of α in the range $\alpha \in [0.80, 1.20]$

$$\begin{aligned}
& \int_0^\infty d\Gamma \exp\left(-\frac{\ln^2(\Gamma/\Gamma_{mf})}{\omega^2}\right) \left[\int_0^\infty dt \exp(-\Gamma t) t^n \right] \\
&= \int_0^\infty d\Gamma \exp\left(-\frac{\ln^2(\Gamma/\Gamma_{mf})}{\omega^2}\right) \left[\frac{d^n}{d\Gamma^n} \int_0^\infty dt (-1)^n \exp(-\Gamma t) \right] \\
&= n! \int_0^\infty d\Gamma \exp\left(-\frac{\ln^2(\Gamma/\Gamma_{mf})}{\omega^2}\right) \frac{1}{\Gamma^{n+1}} \\
&= n! \frac{1}{\Gamma_{mf}^n} \int_{-\infty}^{+\infty} dx \exp\left(-\frac{x^2}{\omega^2}\right) \exp(-nx) \\
&= \omega\sqrt{\pi} \left[n! \Gamma_{mf}^{-n} \exp\left(\frac{\omega^2 n^2}{4}\right) \right]
\end{aligned}$$

where the same change of variable as for the denominator, $x = \ln(\Gamma/\Gamma_{mf})$, was used. This way, the moment of order n for the log-normal distribution is given by:

$$\langle t^n \rangle = \Gamma_{mf}^{-n} \exp\left(\frac{\omega^2 n^2}{4}\right) n! \quad (5.11)$$

By inserting equation 5.11 into equation 5.2, one finds the ratio R_n for the log-normal distribution, given by

$$\begin{aligned}
R_n &= \frac{\Gamma_{mf}^{-n} \Gamma_{mf}^{(-n+2)}}{\Gamma_{mf}^{(-2n+2)}} \exp\left\{ \frac{\omega^2}{4} \left[n^2 + (n-2)^2 - 2(n-1)^2 \right] \right\} \frac{n}{n-1} \\
&= \exp\left(\frac{\omega^2}{2}\right) \frac{n}{n-1}
\end{aligned} \quad (5.12)$$

In Figure 30 the ratio R_n versus the order n for equation 5.12 is plotted for multiple values of width ω . One can observe that an increase in ω leads to an overall exponential positive shift in the ratio R_n , which is equivalent to a shift of the R_n ratio for the single exponential function. By comparing equation 5.3 with equation 5.12 one sees the latter equation is equivalent to eq. 5.3 multiplied by $\exp(\omega^2/2)$.

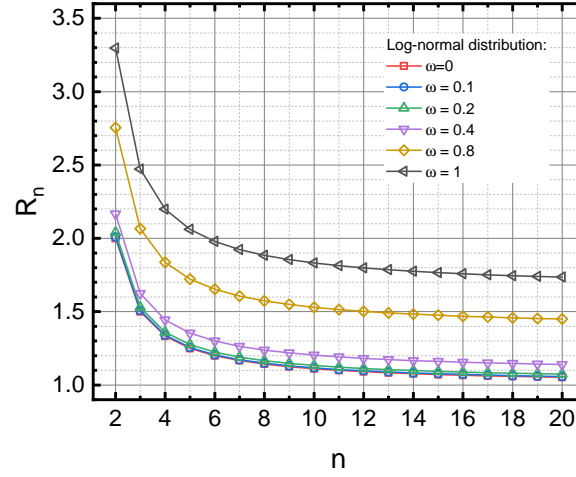


Figure 30: Ratio of moments R_n for the log-normal distribution decay function, for different values of the width parameter ω .

5.2 STUDY OF STATISTICAL MOMENTS OF EXPERIMENTAL DATA SETS

For data sets, the range of integration for equation 5.1 lies between the initial time bin t_0 , e.g., the time for which the number of arriving photons is maximum, and the final time bin t_f , which is the maximum resolution of the experiment. So, equation 5.1 is treated regarding its range of integration and assuming that $f(t)$ is now a data set of histogram counts in discrete instants of time:

$$\langle t^n \rangle = \frac{\int_{t_0}^{t_f} f(t) t^n dt}{\int_{t_0}^{t_f} f(t) dt}, \quad (5.13)$$

A way to calculate integrals in equation 5.13 is by using numerical integration via Simpson's rule, which approximates the function $f(t)$ by a quadratic polynomial over pairs of sub-intervals [82]. A custom Matlab code was implemented in order to proceed with the numerical integration of the statistical moments using Simpson's rule (See Appendix C.2) and those results were used to calculate the ratio of moments R_n by using equation 5.2 (see Appendix C.3). In the following section, a discussion of the results of calculating the R_n ratio for the experimental decay measurements will be presented.

5.3 DISCUSSION OF THE STATISTICAL MOMENTS ANALYSIS' RESULTS

5.3.1 Best fit distribution

In this sub-chapter, two of the PbS QDot samples will be studied and compared regarding their statistical moments. The two samples are Only B (PbS QDots with no cross-linking) and B+B (PbS QDots with chemical linker), for three different aggregation times Δt ⁴. Thus, four sets of data are to be compared. Four different emission wavelengths were studied in this work: 1140 nm, 1160 nm, 1200 nm and 1240 nm (see Figure 31)⁵. For each wavelength, statistical moments were calculated for each experiment using the respective time-resolved experimental data and applying the numerical integration method described in Chapter 5.2.

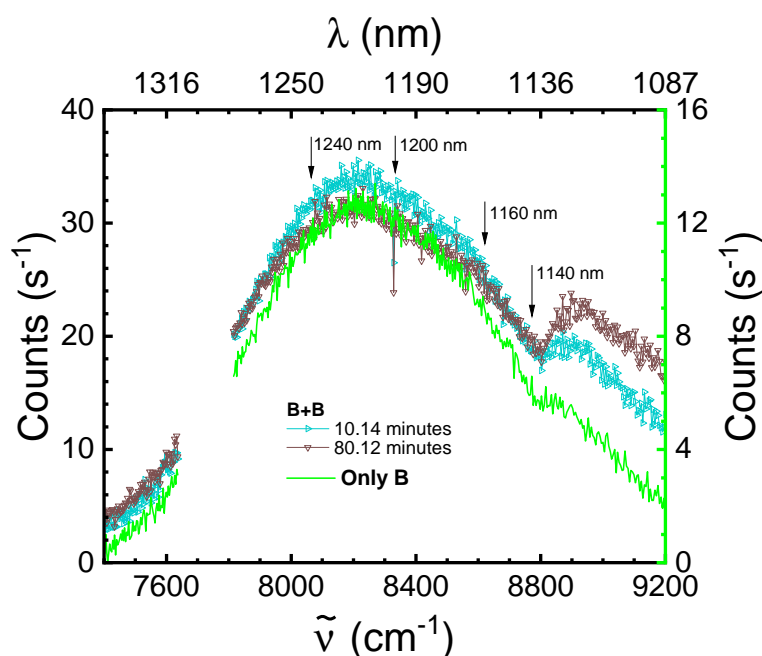


Figure 31: Emission spectra for the two samples studied - Only B and B+B - as shown in the previous chapter. Here the four arrows mark four different regions of the spectra for which statistical moments were calculated.

Figure 32 presents the ratio R_n based on the four experimental results for the four different wavelengths. In red, blue and green dotted lines are presented the values of R_n for the B+B sample for different aggregation times, $\Delta t = [18 - 27]$ minutes,

⁴ See Chapter 4 for the sample's nomenclature description.

⁵ Opposite to the study of the emission spectra and photoluminescence kinetics in Chapter 4, light wavelength was preferred to light wavenumber in the description of the samples' spectra.

$\Delta t = [46 - 74]$ minutes and $\Delta t = [120 - 148]$ minutes, respectively. The purple dotted lines present the values of R_n for the sample Only B.

Let us analyse each graph carefully. In Figure 32a, for wavelength 1140 nm, integration works well until $n = 7$, yielding negative values for bigger n . The reason for this negative integral values is unclear. For small n , the values of R_n of the B+B sample are consistently higher comparing with the Only B sample. This rise correlates with the increase of the number of acceptor molecules available for FRET, described by the homogeneous acceptor distribution decay function. On the other hand, the appearance of a small peak at $n = 5$ for the red dotted data can only be related to the behaviour of the shell-type acceptor distribution function.

In Figure 32b, for wavelength 1160 nm, integration of data works well besides for the red line between values of $n \in [6, 8]$. The dotted lines related with the B+B sample display higher values of R_n for $n \in [2, 4]$ comparing with the Only B data, although the same behaviour cannot be seen for higher n , where the sample Only B shows a slight convexity and overall higher value of R_n for $n \in [5, 10]$. The only studied function that can explain this appearance is the shell-type distribution decay function, which might mean that some energy transfer indeed have been occurring at this wavelength for the studied sample.

In Figure 32c, for wavelength 1200 nm, since it lies closer to the peak emission of the samples, one could expect more consistent results. It can be observed that the experimental values of R_n lie over the minimum value of $R_n = 1$, which is the same trend found for the theoretical distributions studied. It can be seen as well that the Only B data lies within the range $R_n \in [1, 2]$. This is a sign that the Only B results can be approximately described by a single-exponential function, which means that there is no relevant energy transfer before introducing the chemical linker. As in the Figures 32a and 32b, sample B+B shows considerably higher values of R_n for small n ($n \in [2, 4]$) comparing with the values for the Only B sample, while the opposite is observed for higher n ($n \in [5, 10]$). This change for higher n could be explained for the shell-type acceptor distribution function, which might indicate a change of donor-acceptor distance. The blue and green dotted lines, $\Delta t = [46 - 74]$ minutes and $\Delta t = [120 - 148]$ minutes respectively, are considerably overlapped through the whole range of n , which might indicate that the linked QDot system did not considerably evolve during the interval between the two aggregation times, for this particular wavelength.

In Figure 32d, for wavelength 1240 nm, it is noticeable a convexity on the red dotted

line, sample B+B for $\Delta t = [18 - 27]$ minutes, for values of $n \in [4, 10]$. As before, the shell-type acceptor distribution function is suitable to explain such maximum. Let us focus on the blue and green dotted lines, which refer to two different aggregation times of sample B+B. The green dotted line shows higher R_n comparing with the blue dotted line, for $n \in [2, 3]$, while the opposite is observed for $n \in [4, 10]$. The reason could be that the acceptor distribution might have changed over time. In the top right corner of Figure 33 a comparison between the theoretical functions is presented, with $N_0 = 3$, where an intersection can be observed. Another possibility could be that the donor-acceptor distance, which alters the parameter α , has changed over time. As it can be seen in Figure 33, the change of α promoted an intersection between different R_n plots.

From the previous qualitative analysis regarding Figure 32, one can select one of the theoretical functions, analysed in Chapter 5.1, which best describes the ratio R_n experimental results. The single exponential decay corresponds to a function of R_n which does not depend on other parameters and only lies in the range $R_n \in [2, 1[$ for $n \in [2, +\infty[$. In the majority of the studied situations, this function was better suited to describe the data for the Only B sample (i.e, without QDot cross-linker). In Figure 33 one example is shown, where we can observe that the single exponential function compares well with the purple dotted line, for the Only B sample. The homogeneous acceptor distribution decay function can explain the stretch of the R_n function, although it cannot model the maximum seen in some experimental data for the B+B sample. On the other hand, the shell-type acceptor distribution function can predict the appearance of this new peak, alongside with the stretch of the left tail of the R_n function and the intersection of two "experimental" R_n curves. Finally, the log-normal distribution has a function of R_n which introduces an exponential positive upward shift with the increasing width parameter ω , shifting the position of the asymptote $n = 1$. Such an effect is not present in the obtained data.

Therefore, here it is concluded that the shell acceptor distribution decay function is the only one among the considered theoretical functions that can describe most of the experimental results. It is adjustable, since it has two parameters, α and N_0 , and allows for a clear physical interpretation. It is also the only studied function that models the peak in the R_n function for higher number of acceptors, N_0 . In Figure 34 the shell-type distribution function was adjusted to reproduce the experimental data, which had a maximum (the same data as the red dotted line in Figure 32d), and the same experimental trend was found, on the contrary to what was observed with

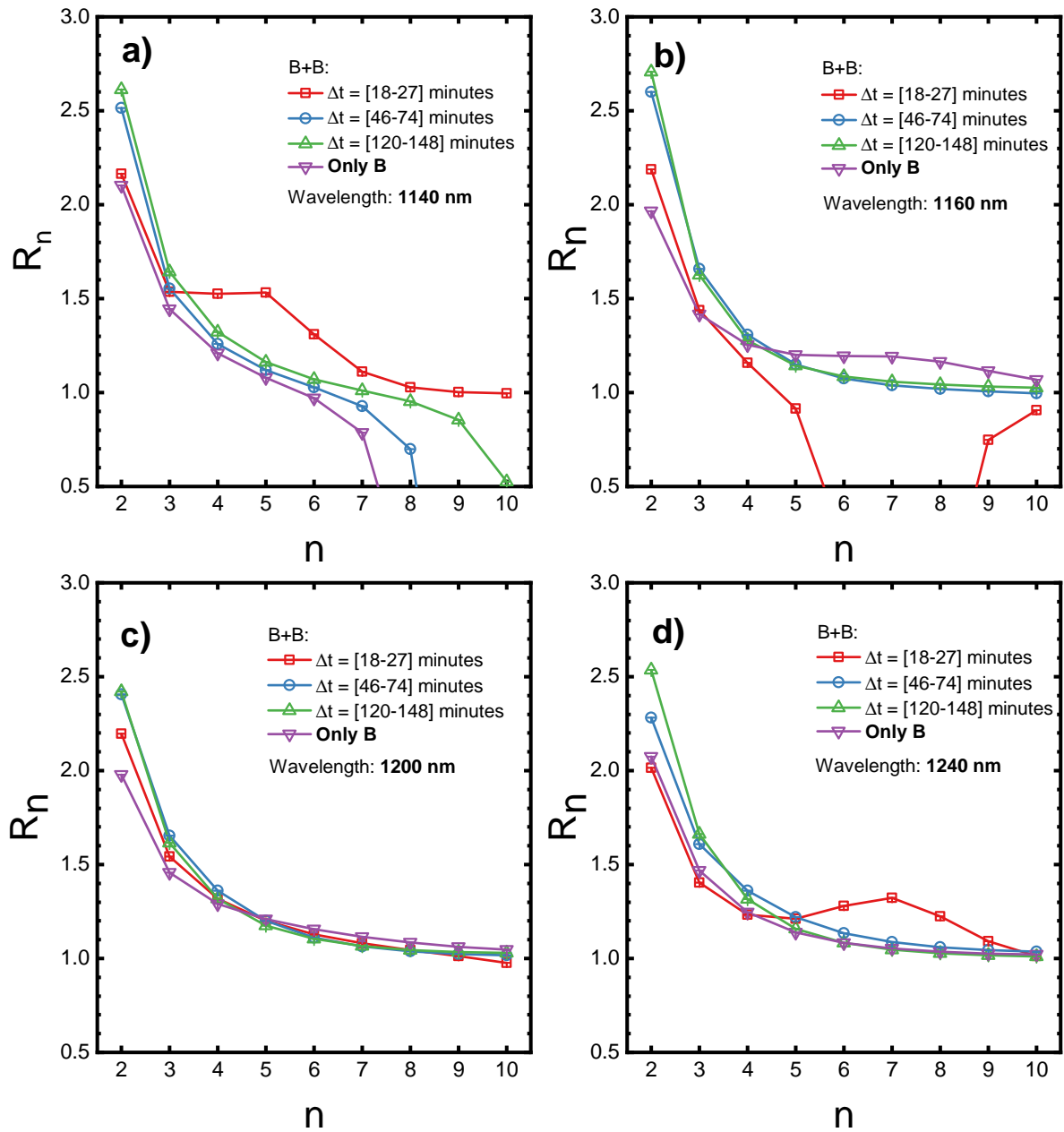


Figure 32: Calculated R_n for four different emission wavelengths: **a)** 1140 nm, **b)** 1160 nm, **c)** 1200 nm and **d)** 1240 nm. Error bars, though proportionally small to the values of R_n , are presented in each dot. In figure b), for $n \in [6, 8]$ the red curve presents negative values, which are not presented in the plot.

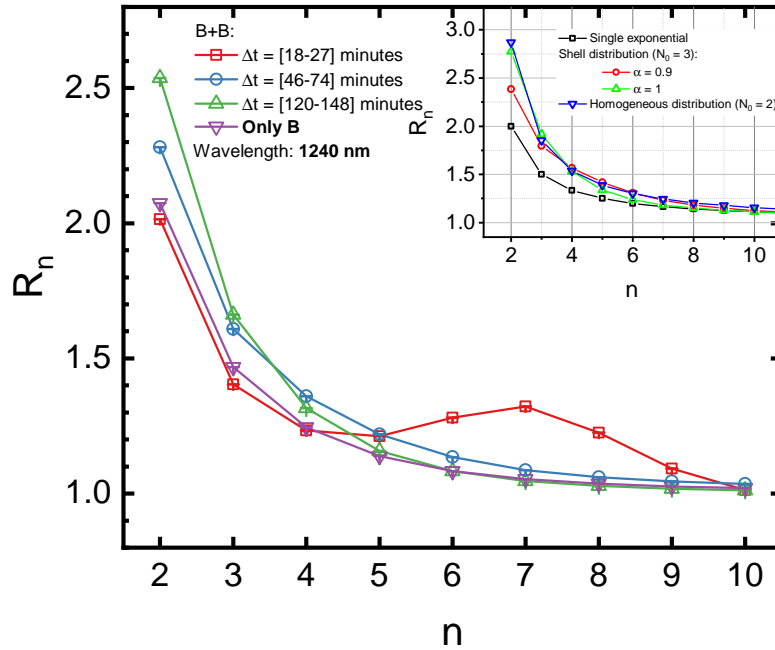


Figure 33: Experimental results for the ratio R_n for $\lambda = 1240\text{nm}$. In the top right corner some R_n functions based on theoretical decay functions are presented.

the homogeneous acceptor distribution function, for the same number of acceptors, N_0 . By finding suitable values of α and N_0 one can track the average donor-acceptor distance and the acceptor concentration at the time-stages of the experiment. Knowing that $N_0 = 4/3\pi C_0 R_0^3$ and $\alpha = R_0/a$, where C_0 is the acceptor concentration per unit volume, the Förster radius R_0 and the donor-acceptor distance a can be calculated as

$$R_0^3 = \frac{3}{4\pi C_0} N_0 \quad \text{and} \quad a = \frac{R_0}{\alpha}. \quad (5.14)$$

In order to find the values of R_0 and a , one has to estimate first the acceptor concentration C_0 on the QDot system, which will be done in the next sub-section.

5.3.2 Determining the experimental Förster radius and the average donor-acceptor distance

From the information provided in Chapter 3.3.3 regarding the purchased solution of PbS QDots, one can determine the concentration of PbS QDots of the stock sample C_i :

$$C_i = \frac{1\text{nmol}}{100\mu\text{L}} = \frac{10^{-9} \cdot 6 \times 10^{23}}{10^{-7}\text{m}^3} = 6 \times 10^{21} \text{ m}^{-3} \quad (5.15)$$

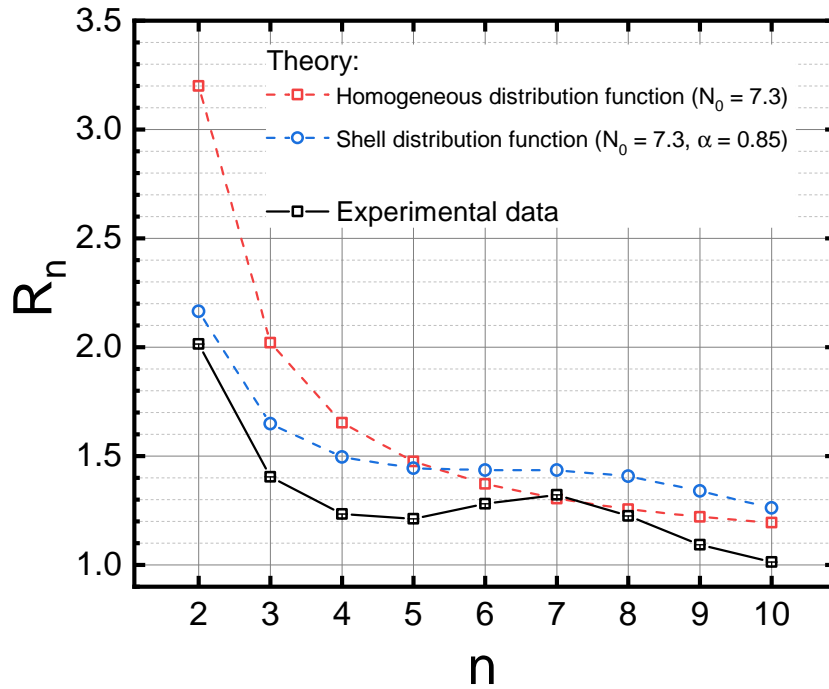


Figure 34: Comparison of data curve obtained from experimental results with theoretical decay models.

Due to the addition of the EDC and NHS chemicals, the solution was 10 % diluted. Thus the concentration of PbS QDots C_{PbS} is

$$C_{\text{PbS}} = \frac{C_i}{1.1} \simeq 5.5. \times 10^{21} \text{ m}^{-3} \quad (5.16)$$

Of course, not all of these QDots can serve as acceptors for a given donor QDots. Only the QDots that resonantly match the donor's emission spectrum can effectively participate in FRET. For a single donor QDot of radius R_D , QDots of a certain range of radius, ΔR_A , are suitable acceptors matching the exciton transition energy of the donor. The centre of this interval is slightly shifted to larger R due to the Stokes shift between the emission and absorption, although this shift is not very large for an individual QDot. The acceptor range ΔR_A can be estimated in the following way:

$$\Delta R_A = \left| \frac{dE}{dR} \right|^{-1} \Bigg|_{R=\bar{R}_A} \Delta E, \quad (5.17)$$

where E is the QDot exciton energy, $\Delta E = \Delta E_D + \Delta E_A$ is the width of the energy interval where the donor emission spectra and the acceptor emission spectrum overlap

and \bar{R}_A is the centre of the interval of the size range of suitable acceptors, ΔR_A . E is given by

$$E(R) = E_g + \frac{\hbar^2}{2\mu}R^{-2} - \beta R^{-1}, \quad (5.18)$$

where E_g is the bulk band-gap energy, μ is the exciton's reduced effective mass and β is a constant. The last term represents the electron-hole Coulomb interaction⁶. \bar{R}_A can be defined as

$$\bar{R}_A = R_D + \left. \left| \frac{dE}{dR} \right|^{-1} \right|_{R=R_D} \Delta E_s \quad (5.19)$$

where ΔE_s is the Stokes shift for the donor QDot.

The acceptor concentration, C_0 , can be evaluated as

$$C_0 = C_{\text{PbS}} \cdot f(R_D) \Delta R_A, \quad (5.20)$$

where $f(R_D)$ is the normalized distribution function of QDot radius. The Gaussian function approximates this distribution, and it is defined as

$$f(R) = \frac{1}{\sqrt{2\pi\sigma_R^2}} \exp \left[-\frac{1}{2} \left(\frac{R - \bar{R}}{\sigma_R} \right)^2 \right], \quad (5.21)$$

where σ_R is the QDot size dispersion, i.e, standard deviation and \bar{R} is the most probable QDot radius, which determines the absorption peak.

A rough estimate of C_0 can be performed. Neglecting the last term in Equation 5.18⁷, one has:

$$\frac{dE}{dR} = -\frac{\hbar^2}{\mu R^3} = \frac{2}{R} [E_g - E(R)]. \quad (5.22)$$

⁶ The exciton effective mass was defined by assuming $m_e^* = m_h^*$, as seen for PbS QDots. See Chapter 2.1 for the derivation of the elements of Equation 5.18.

⁷ In Chapter 2.1 it was affirmed that PbS QDots lie on the strong confinement regime. Thus, neglecting the exciton Coulomb interaction is a valid approximation.

If the Stokes shift is also neglected, one has from Equation 5.19 that $\bar{R}_A \simeq R_D$. Using the result of Eq. 5.22 in Eq. 5.17 assuming negligible Stokes shift, one has that

$$\begin{aligned} \frac{\Delta R_A}{\bar{R}_A} &\simeq \frac{\Delta R_A}{R_D} = \left\{ \frac{2}{R_D} [E_g - E(R_D)] \right\}^{-1} \Delta E \cdot \frac{1}{R_D} \\ &= \frac{\Delta E}{2 [E_g - E(R_D)]} \end{aligned} \quad (5.23)$$

This ratio depends on the excitation wavelength, which determines R_D . Using Eqs. 5.21 and 5.23 in Eq. 5.20 defines the acceptor concentration C_0 as

$$C_0 = \eta(R_D) C_{PbS} \quad (5.24)$$

where

$$\eta(R) = \frac{R_D}{\sqrt{2\pi\sigma_R^2}} \exp \left[-\frac{1}{2} \left(\frac{R - \bar{R}}{\sigma_R} \right)^2 \right] \frac{\Delta E}{2 [E(R_D) - E_g]}. \quad (5.25)$$

For instance, for donors being the most probable sized QDots, $R_D = \bar{R}$. Thus, from Eq. 5.25,

$$\eta(\bar{R}) = \frac{\bar{R}}{\sqrt{2\pi\sigma_R^2}} \frac{\Delta E}{2 [E(\bar{R}) - E_g]} \quad (5.26)$$

Now, one has to estimate the values of \bar{R} , $E(\bar{R})$ and σ_R from experimental data, namely for sample Only B. Assuming $\Delta E \approx 1\text{meV}$ we find that $\eta \approx 10^{-2}$ and, therefore, $C_0 \approx 10^{-2} C_{PbS} \simeq 5.5 \times 10^{-8} \text{nm}^{-3}$ ⁸. This value means that the average distance between uniformly distributed QDot acceptors (and also their typical distance from a donor) is $r_0 \sim C_0^{-1/3} \simeq 263\text{nm}$, which is too large to have non-radiative energy transfer such as FRET in the QDot system. This is expected in a sample of homogenous dispersed colloidal QDots (e.g. the sample Only B, studied in this chapter). The average distance, r_0 , is reduced with the aggregation of QDots, stimulated by adding the chemical linker (e.g. the sample B+B, studied in this chapter). Such an aggregate (or cluster) must have a size large enough to include N QDots, of which about $\eta N_{QD} \approx 5 \times 10^{-3} N$ will be suitable acceptors for the donor dot located in the centre of the sphere (see Figure 35). In this case, of course, the donor-acceptor separations are not the same for all acceptors in the cluster, but, if the aggregate is compact, typical donor-acceptor distances, $R_A = |\mathbf{r}_A - \mathbf{r}_D|$, are of the order of the cluster radius, a_c .

⁸ The calculation of η can be found in Appendix B.1.

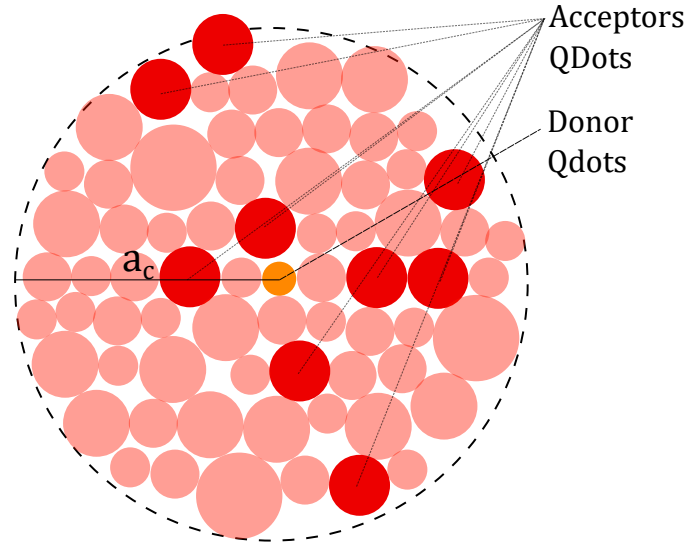


Figure 35: 2-dimensional schematic of a QDot spherical cluster, with radius a_c . In the centre of the sphere, in an orange circle, lies the donor QDot and, surrounding this donor, in vivid red circles, are presented several acceptor QDots.

Indeed, we can calculate the average donor-acceptor distance, $\langle R_A \rangle$, in a spherical cluster of volume $V_c = \frac{4}{3}\pi a_c^3$ as

$$\begin{aligned} \langle R_A \rangle &= \frac{\int_{V_c} R_A dV_c}{V_c} \\ &= \frac{\int_0^{a_c} R_A^3 dR_A}{a_c^3/3} = \frac{3}{4}a_c \end{aligned} \quad (5.27)$$

Since, from Eq. 5.27, $\langle R_A \rangle$ is of the range of the cluster radius, the fixed-shell model can still be used in our estimates.

Based on the fixed-shell acceptor distribution function, in a sphere of radius $a_c = R_0/\alpha$ there should be

$$N = \frac{N_0}{\eta} \quad (5.28)$$

QDots (where η is given by equation 5.26), of which N_0 will be suitable acceptors for the donor located in the centre of the sphere. Here it is assumed the interpretation of Figure 35, where a_c is now the typical QDot cluster size. We can write N as all the QDots packed inside a sphere of radius a_c as it follows:

$$N = \frac{\frac{4\pi}{3}a_c^3}{\frac{4\pi}{3}\bar{R}^3} \cdot \text{FF} \quad (5.29)$$

where FF is the filling factor, which describes the volume fraction occupied by QDots in an agglomerate. For instance, for hexagonal close packing of spheres (assuming spherical QDots), $FF = 0.74$. Combining Eqs. 5.28 and 5.29 we have that

$$a_c = \bar{R}^3 \sqrt[3]{\frac{N_0}{\eta FF}}. \quad (5.30)$$

By using $\eta \approx 10^{-2}$, the value of $N_0 = 7.3$ and $\alpha = 0.85$, found with the fit of the shell acceptor distribution function (presented in Figure 34) and assuming $\bar{R} \simeq 2.1\text{nm}$ (calculated in Appendix B.1) gives an estimate of the cluster radius of $a_c \simeq 21\text{nm}$. From the result of Eq. 5.27, the average acceptor distance is estimated as $\langle R_A \rangle \simeq 16\text{nm}$. Since $R_0 = \alpha a_c$, the estimated Förster distance for the PbS QDot sample is around $R_0 \simeq 18\text{nm}$.

One can compare this estimate with values of R_0 reported in the literature. Clark et al [83] estimated the Förster radius of $(8.0 \pm 0.7)\text{nm}$ and a QDot separation distance around 5 – 6nm in oleic acid capped PbS QDots tightly packed into glass films. Bose et al [84] estimated the Förster radius of 12 – 13nm for a QDot separation distance of 10nm in PbS QDots solids over silicon wafers. Both estimates, as the authors affirm, were calculated based on QDot absorption and emission spectra and using the formula presented in equation 2.56 of Chapter 2.4. The estimate here presented for the Förster radius in colloidal PbS QDots is just slightly higher than the ones found by Clark et al and Bose et al. Further studies on statistical moments of photoluminescence kinetics of QDot aggregates should consider a modification of the fixed-shell distribution function in order to increase the accuracy of the obtained parameter values.

Further study of this experimental data could also include the fitting of the (modified) fixed-shell distribution function onto the remaining data presented on Figure 32, including other stages of the QDot binding process, in order to detect with detail the fluctuation of cluster size and the influence of FRET with increasing aggregation time. However, one can observe from the results that FRET is more efficient during the stage of aggregation $\Delta t = [18 - 27]$ minutes, due to the presence of a R_n peak, which is strongly correlated with a greater number of acceptors at a distance $R \leq R_0$ from the donor, N_0 . For further aggregation stages, the efficiency of FRET is considerably lower, related with a decrease of N_0 .

CONCLUSION

This research project had the goal to detect the evidence of FRET mechanism in a colloidal solution of cross-linked PbS quantum dots, which emit light in the infrared range of the light's spectrum. The experiments here described are one of the first known attempts to study this non-radiative energy transfer mechanism in an infrared system of colloidal quantum dots.

Measurements of emission spectra of three PbS quantum dot samples, with different QDot size distributions, from company Mesolight, labeled here as samples A, B, and C, showed a rather broad emission band with the broadening related with particle size dispersion (the results are presented in Chapter 4.1). This broadening was high enough to conclude that there was contamination in samples A and C. Further study was focused on sample B that showed a single exciton band in its emission spectrum, and it was used to produce cross-linked QDot samples using NHS/EDC Chemistry.

For the cross-linked QDot samples, numerous emission spectra were collected at different QDot aggregation times Δt , which results are presented in Chapter 4.1. The evolution of the sample with increasing Δt showed fluctuating peak intensities, which might have come from slight density fluctuations in the sample spectra, and a negligible change in the peak position of the spectra. The FRET mechanism would represent an energy redistribution of the emitted light, since larger gap smaller sized QDots would transfer their energy to smaller gap larger sized ones by dipole-dipole coupling mechanism, which would produce a red-shift in the emission spectrum. Therefore, the FRET mechanism is not readily observable in our steady-state emission spectra.

The fit of the samples' luminescence kinetics (see Chapter 4.2) has shown different results by using two different theoretical decay functions. The fitting of data with a

phenomenological log-normal distribution of decay rates showed an increased decay rate for the cross-linked QDot sample compared with the non-cross-linked sample. From this result the FRET efficiency, η_{FRET} , was estimated in the range of values $0\% < \eta_{\text{FRET}} < 40\%$, for several light wavenumbers studied. This result indicates an evidence of FRET in the cross-linked QDot sample, and presented increasing FRET efficiency for longer aggregation times. However, a considerable error fluctuation of the measured efficiency caused reasonable uncertainty in the obtained results. The fit with a homogeneous acceptor distribution decay function (the stretched exponential function), which function was derived in Chapter 2.5.1, produced fitted values of decay rate with overall smaller error fluctuation. However, for light wavenumbers, the FRET efficiency yielded negative values, which result does not hold physical meaning. Including other contradicting results from this decay function fit, the overall obtained picture of FRET in the cross-linked samples is unclear, which increases doubt concerning the data obtained by the fitting of the luminescence kinetics.

Yet, it seems to have been possible to get a evidence of FRET processes taking place in the studied system, where the QDot cross-linking introduces correlations in spatial positions of QDots, and some of these correlated dots may form donor-acceptor pairs. The developed analysis of statistical moments of the emission decay kinetics, applied to several model functions (such as single- and stretched-exponential decays) and also to the experimental data, allowed for showing, in Chapter 5, that the linking does affect the emission decay kinetics. The found changes in the distribution of the statistical moments of the experimental is compatible, at a certain stage of QDot cross-linking, with the formation of a small cluster of acceptors around a donor QDot, approximately reproduced by a shell model. With this decay model, further understanding of the QDot system has been found including estimates of the average donor-acceptor distance and the Förster radius. While from the decay function fitting a clear picture of FRET was not found, the study of statistical moments of the decay kinetics proved to be a promising alternative data treatment approach as demonstrated in the study of cross-linked PbS colloidal QDots performed in this thesis.

Some considerations and suggestions for future experiments can be pointed out. A possible cause for low evidence of FRET is the excitation laser wavelength used (685 nm red laser), since the incoming light is strongly absorbed for virtually all sizes of PbS quantum dots of the solution. This way, in the cross-linked QDot system, both donor and acceptor can be in excited states. This may reduce the possibility to observe

the FRET mechanism. Embedding PbS QDots in films of multiple layers (as described by C.Blum et al [85]) could be a better strategy to excite selectively the donor quantum dots and increase the likelihood to observe the FRET mechanism. Other limitation from the experiment might have been the option of cross-linking QDots only from one sample with a specific QDot size distribution. Due to Stokes' shift, the overlap of the emission spectrum and absorption spectrum might not have been optimal in the experiments performed, which might have lowered the efficiency of the FRET mechanism.

Regarding the cross-linked sample production, different concentrations of the used linker (EDC/NHS) could be studied, in order to better understand the linker's role on the change of the emission spectra of the samples and on the number of decay channels of the QDot aggregates. Other studies can be made by placing PbS QDots at higher density media, for instance on a substrate. From the data analysis perspective, further studies of the statistical moments of photoluminescence kinetics can be made by considering decay functions related with different donor-acceptor geometries.

Appendices

A

DERIVATION OF SOME THEORETICAL RELATIONS USED IN THE THESIS

A.1 DESCRIPTION OF ELECTRIC FIELD NORMAL MODES IN TERMS OF GREEN FUNCTION DYADICS

This derivation aims to describe the partial local density of states in terms of the Green's function $\overset{\leftrightarrow}{\mathbf{G}}$. This function, applied on electric fields, gives the electric field at position \mathbf{r} due to a point dipole (described by a delta function) at position \mathbf{r}_0 [63]. Thereafter, this expression is used to describe the spontaneous decay rate γ of a two-level quantum emitter in terms of a Green dyadic¹. From chapter 2.2, the spontaneous decay is expressed as

$$\gamma = \frac{4\pi^2\omega}{3\hbar\epsilon_1} |\mathbf{d}|^2 \rho_p(\mathbf{r}_0, \mathbf{n}_d, \omega_0), \quad (\text{A.1})$$

where ρ_p is the partial local density of states, defined as:

$$\rho_p(\mathbf{r}_0, \mathbf{n}_d, \omega_0) = 3 \sum_{\mathbf{k}} \left[\mathbf{n}_d \cdot (\mathbf{u}_{\mathbf{k}} \otimes \mathbf{u}_{\mathbf{k}}^*) \cdot \mathbf{n}_d \right] \delta(\omega_{\mathbf{k}} - \omega_0), \quad (\text{A.2})$$

where \mathbf{n}_d is the unit vector of the transition dipole moment \mathbf{d} , and $\mathbf{u}_{\mathbf{k}}$ are the normal modes of the electric field $\mathbf{E}_{\mathbf{k}}$. In this appendix the relation between these normal modes and its Green's function will be derived.

The electric field's normal modes \mathbf{n}_p are position and frequency dependent, and they satisfy the wave equation:

$$\nabla \times \nabla \times \mathbf{u}_{\mathbf{k}}(\mathbf{r}, \omega_{\mathbf{k}}) - \frac{\omega_{\mathbf{k}}^2}{c^2} \mathbf{u}_{\mathbf{k}}(\mathbf{r}, \omega_{\mathbf{k}}) = 0, \quad (\text{A.3})$$

¹ A dyad is a second order tensor.

and they fulfil the orthogonality relation

$$\int_V d\mathbf{r} \mathbf{u}_{\mathbf{k}} \mathbf{u}_{\mathbf{k}'}^* = \delta_{\mathbf{k},\mathbf{k}'} \quad (\text{A.4})$$

where the integration runs over all mode's volume V and $\delta_{\mathbf{k},\mathbf{k}'}$ is the Kronecker delta. One can expand the Green's function $\overset{\leftrightarrow}{\mathbf{G}}$ in terms of the normal modes [9]:

$$\overset{\leftrightarrow}{\mathbf{G}}(\mathbf{r}, \mathbf{r}', \omega) = \sum_{\mathbf{k}} \mathbf{A}_{\mathbf{k}}(\mathbf{r}', \omega) \mathbf{u}_{\mathbf{k}}(\mathbf{r}, \omega_{\mathbf{k}}), \quad (\text{A.5})$$

where \mathbf{r}' is the electric field source position and \mathbf{r} is the position where is measured the electric field. The vectorial coefficients $\mathbf{A}_{\mathbf{k}}$ are still to be determined. The definition of the Green function is given by the Helmholtz equation [9, 63]:

$$\nabla \times \nabla \times \overset{\leftrightarrow}{\mathbf{G}}(\mathbf{r}, \mathbf{r}'; \omega) - \frac{\omega^2}{c^2} \overset{\leftrightarrow}{\mathbf{G}}(\mathbf{r}, \mathbf{r}'; \omega) = \overset{\leftrightarrow}{\mathbf{I}} \delta(\mathbf{r} - \mathbf{r}'), \quad (\text{A.6})$$

where $\overset{\leftrightarrow}{\mathbf{I}}$ is the unit dyad. Introducing the expansion of equation A.5 into equation A.6 gives:

$$\begin{aligned} \sum_{\mathbf{k}} \mathbf{A}_{\mathbf{k}}(\mathbf{r}', \omega) \left[\nabla \times \nabla \times \mathbf{u}_{\mathbf{k}}(\mathbf{r}, \omega_{\mathbf{k}}) - \frac{\omega^2}{c^2} \mathbf{u}_{\mathbf{k}}(\mathbf{r}, \omega_{\mathbf{k}}) \right] &= \overset{\leftrightarrow}{\mathbf{I}} \delta(\mathbf{r} - \mathbf{r}') \\ \Rightarrow \sum_{\mathbf{k}} \mathbf{A}_{\mathbf{k}}(\mathbf{r}', \omega) \left[\frac{\omega_{\mathbf{k}}^2}{c^2} - \frac{\omega^2}{c^2} \right] \mathbf{u}_{\mathbf{k}}(\mathbf{r}, \omega_{\mathbf{k}}) &= \overset{\leftrightarrow}{\mathbf{I}} \delta(\mathbf{r} - \mathbf{r}'), \end{aligned} \quad (\text{A.7})$$

where in the last step the relation of equation A.3 was used. Multiplying both sides of the equation by $\mathbf{u}_{\mathbf{k}'}^*(\mathbf{r}', \omega_{\mathbf{k}'})$ and integrating over the whole mode volume gives:

$$\sum_{\mathbf{k}} \mathbf{A}_{\mathbf{k}}(\mathbf{r}', \omega) \left[\frac{\omega_{\mathbf{k}}^2}{c^2} - \frac{\omega^2}{c^2} \right] \int d\mathbf{r} \mathbf{u}_{\mathbf{k}'}^*(\mathbf{r}', \omega_{\mathbf{k}'}) \mathbf{u}_{\mathbf{k}}^*(\mathbf{r}, \omega_{\mathbf{k}}) = \overset{\leftrightarrow}{\mathbf{I}} \int d\mathbf{r} \delta(\mathbf{r} - \mathbf{r}') \mathbf{u}_{\mathbf{k}'}^*(\mathbf{r}, \omega_{\mathbf{k}'}) \quad (\text{A.8})$$

By making use of the orthogonality relations, i.e, using equation A.4, the coefficients $\mathbf{A}_{\mathbf{k}}(\mathbf{r}', \omega)$ can be defined as:

$$\mathbf{A}_{\mathbf{k}'}(\mathbf{r}', \omega) = c^2 \frac{\mathbf{u}_{\mathbf{k}'}^*(\mathbf{r}', \omega_{\mathbf{k}'})}{\omega_{\mathbf{k}'}^2 - \omega^2}. \quad (\text{A.9})$$

One can use the result of equation A.9 in equation A.5 by substituting $\mathbf{k}' \equiv \mathbf{k}$, and it yields

$$\begin{aligned} \overleftrightarrow{\mathbf{G}}(\mathbf{r}, \mathbf{r}'; \omega) &= \sum_{\mathbf{k}} c^2 \frac{\mathbf{u}_{\mathbf{k}}^*(\mathbf{r}', \omega_{\mathbf{k}}) \mathbf{u}_{\mathbf{k}}(\mathbf{r}, \omega_{\mathbf{k}})}{\omega_{\mathbf{k}}^2 - \omega^2} \\ &= \sum_{\mathbf{k}} \frac{c^2}{2\omega_{\mathbf{k}}} \mathbf{u}_{\mathbf{k}}^*(\mathbf{r}', \omega_{\mathbf{k}}) \mathbf{u}_{\mathbf{k}}(\mathbf{r}, \omega_{\mathbf{k}}) \left(\frac{1}{\omega_{\mathbf{k}} - \omega} + \frac{1}{\omega_{\mathbf{k}} + \omega} \right) \end{aligned} \quad (\text{A.10})$$

One can introduce an imaginary part with positive modulus value η in the frequency, i.e, $\omega \equiv \omega + i\eta$, and set the Green function as the limit to which η goes to zero, as follows

$$\overleftrightarrow{\mathbf{G}}(\mathbf{r}, \mathbf{r}'; \omega) = \lim_{\eta \rightarrow 0} \sum_{\mathbf{k}} \frac{c^2}{2\omega_{\mathbf{k}}} \mathbf{u}_{\mathbf{k}}^*(\mathbf{r}', \omega_{\mathbf{k}}) \mathbf{u}_{\mathbf{k}}(\mathbf{r}, \omega_{\mathbf{k}}) \left(\frac{1}{\omega_{\mathbf{k}} - \omega - i\eta} + \frac{1}{\omega_{\mathbf{k}} + \omega + i\eta} \right) \quad (\text{A.11})$$

To proceed one uses the following mathematical identity, named as the Sokhotski-Plemelj formula, which can be proved by complex integration [86]:

$$\lim_{\eta \rightarrow 0} \left(\frac{1}{x \pm i\eta} \right) = P \left(\frac{1}{x} \right) \mp i\pi\delta(x) \quad (\text{A.12})$$

where $P(1/x)$ is the Cauchy principal value and η is a positive real number. With this formula one can divide the Green function of equation A.11 into two parts: real-valued part and the imaginary-valued part of the Green function. Thus, using equation A.12 in equation A.11 one can obtain the imaginary part of the Green function as

$$\text{Im } \overleftrightarrow{\mathbf{G}}(\mathbf{r}, \mathbf{r}'; \omega) = \sum_{\mathbf{k}} \frac{\pi c^2}{2\omega_{\mathbf{k}}} \mathbf{u}_{\mathbf{k}}^*(\mathbf{r}', \omega_{\mathbf{k}}) \mathbf{u}_{\mathbf{k}}(\mathbf{r}, \omega_{\mathbf{k}}) [\delta(\omega - \omega_{\mathbf{k}}) + \delta(\omega + \omega_{\mathbf{k}})]. \quad (\text{A.13})$$

In the previous equation, the Dirac delta restricts all values of $\omega_{\mathbf{k}}$ to ω , which let us remove the $\omega_{\mathbf{k}}$ of the denominator out of the sum. If only assuming positive mode frequencies the $\delta(\omega + \omega_{\mathbf{k}})$ terms is not considered, and equation A.13 reduces to

$$\text{Im } \overleftrightarrow{\mathbf{G}}(\mathbf{r}, \mathbf{r}'; \omega) = \frac{\pi c^2}{2\omega} \sum_{\mathbf{k}} \mathbf{u}_{\mathbf{k}}^*(\mathbf{r}', \omega_{\mathbf{k}}) \mathbf{u}_{\mathbf{k}}(\mathbf{r}, \omega_{\mathbf{k}}) \delta(\omega - \omega_{\mathbf{k}}). \quad (\text{A.14})$$

Now one has to relate equation A.14 with the partial local density of states in equation A.2. If the Green function is evaluated at the origin of the source, i.e, for $\mathbf{r} = \mathbf{r}' = \mathbf{r}_0$, and $\omega = \omega_0$:

$$\frac{6\omega_0}{\pi c^2} \text{Im } \overset{\leftrightarrow}{\mathbf{G}}(\mathbf{r}_0, \mathbf{r}_0; \omega_0) = 3 \sum_{\mathbf{k}} \mathbf{u}_{\mathbf{k}}^*(\mathbf{r}_0, \omega_{\mathbf{k}}) \mathbf{u}_{\mathbf{k}}(\mathbf{r}_0, \omega_{\mathbf{k}}) \delta(\omega_{\mathbf{k}} - \omega_0). \quad (\text{A.15})$$

Therefore the partial local density of states can be rewritten as function of the imaginary part of the Green function, which gives the final result:

$$\rho_{\text{p}}(\mathbf{r}_0, \omega_0) = \frac{6\omega_0 \eta^2}{\pi c^2} \left[\mathbf{n}_{\text{p}} \cdot \left\{ \text{Im } \overset{\leftrightarrow}{\mathbf{G}}(\mathbf{r}_0, \mathbf{r}_0; \omega_0) \right\} \cdot \mathbf{n}_{\text{p}} \right], \quad (\text{A.16})$$

where c is redefined as $c \equiv c/\eta$, where η is the refractive index of the propagating medium.

A.2 ENERGY TRANSFER MATRIX ELEMENT DERIVATION

This derivation is reproduced from the dissertation of Filipa Peres, reference [66]. From chapter 2.3.1 we have the energy transfer matrix element, $M_{i \rightarrow f}$, given by

$$M_{i \rightarrow f} = \sum_{\mathbf{k}, \lambda} \left\{ \frac{\langle f | \hat{H}_{QD}^{(\mathbf{r}=\mathbf{r}_A)} | I_1 \rangle \langle I_1 | \hat{H}_{QD}^{(\mathbf{r}=\mathbf{r}_D)} | i \rangle}{E_{n_i l_i}^{(D)} - \hbar \omega_{\mathbf{k}}} - \frac{\langle f | \hat{H}_{QD}^{(\mathbf{r}=\mathbf{r}_D)} | I_2 \rangle \langle I_2 | \hat{H}_{QD}^{(\mathbf{r}=\mathbf{r}_A)} | i \rangle}{E_{n_i l_i}^{(D)} + \hbar \omega_{\mathbf{k}}} \right\}, \quad (\text{A.17})$$

where \mathbf{r}_A and \mathbf{r}_D are the acceptor QDot and donor QDot positions, respectively, $\hat{H}_{QD}^{(\mathbf{r}=\mathbf{r}_A)}$ and $\hat{H}_{QD}^{(\mathbf{r}=\mathbf{r}_D)}$ indicate the position where the Hamiltonian is interacting with the virtual photon. The initial and final states, $|i\rangle$ and $|f\rangle$ respectively, and the virtual states, $|I_1\rangle$ and $|I_2\rangle$, are defined as

$$\begin{aligned} |i\rangle &= |D_{n_i l_i m_i}\rangle |A_{\text{ground}}\rangle |N_{\mathbf{k}, \lambda}\rangle; \\ |f\rangle &= |D_{\text{ground}}\rangle |A_{n_f l_f m_f}\rangle |N_{\mathbf{k}, \lambda}\rangle; \\ |I_1\rangle &= |D_{\text{ground}}\rangle |A_{\text{ground}}\rangle |N_{\mathbf{k}, \lambda} + 1\rangle; \\ |I_2\rangle &= |D_{n_i l_i m_i}\rangle |A_{n_f l_f m_f}\rangle |N_{\mathbf{k}, \lambda} + 1\rangle. \end{aligned} \quad (\text{A.18})$$

The Hamiltonian is defined as in equation 2.44 of chapter 2.3.1 as

$$\hat{H}_{QD}^{\mathbf{r}} \equiv -\hat{\mathbf{d}}_{QD} \cdot \hat{\mathbf{E}}_{\mathbf{k}, \lambda}(\mathbf{r}), \quad (\text{A.19})$$

where $\hat{\mathbf{d}}_{QD}$ is the electric dipole momentum operator, induced on the quantum dot by the electric field measured in position \mathbf{r} , $\hat{\mathbf{E}}_{\mathbf{k}, \lambda}(\mathbf{r})$, which can be rewritten with the construction and annihilation harmonic oscillators, $\hat{a}_{\mathbf{k}, \lambda}^\dagger$ and $\hat{a}_{\mathbf{k}, \lambda}$ respectively, as

$$\hat{\mathbf{E}}_{\mathbf{k}, \lambda}(\mathbf{r}) \equiv i \left(\frac{2\pi \hbar \omega_{\mathbf{k}}}{V \epsilon_1} \right)^{1/2} \left\{ \mathbf{e}_{\mathbf{k}, \lambda} \hat{a}_{\mathbf{k}, \lambda} e^{i(\mathbf{k} \cdot \mathbf{r} - \omega_{\mathbf{k}} t)} - \mathbf{e}_{\mathbf{k}, \lambda}^* \hat{a}_{\mathbf{k}, \lambda}^\dagger e^{-i(\mathbf{k} \cdot \mathbf{r} - \omega_{\mathbf{k}} t)} \right\}, \quad (\text{A.20})$$

where $\mathbf{e}_{\mathbf{k}}$ and $\mathbf{e}_{\mathbf{k}}^*$ are the electromagnetic radiation polarization vectors, ϵ_1 is the effective dielectric constant of the surrounding medium and V is an arbitrary quantization volume.

Let us develop the bra-kets from equation A.17 using the definition of the Hamiltonian in equation A.19 with the electric field operator defined in equation A.20. The bra-ket $\langle f | \hat{H}_{QD}^{(\mathbf{r}=\mathbf{r}_A)} | I_1 \rangle$ yields

$$\langle f | \hat{H}_{QD}^{(\mathbf{r}=\mathbf{r}_A)} | I_1 \rangle = -i \left(\frac{2\pi\hbar\omega_{\mathbf{k}}}{V\epsilon_1} \right)^{1/2} \langle f | \hat{\mathbf{d}}_A \cdot \left\{ \mathbf{e}_{\mathbf{k},\lambda} \hat{a}_{\mathbf{k},\lambda} e^{i(\mathbf{k}\cdot\mathbf{r}_A - \omega_{\mathbf{k}}t)} - \mathbf{e}_{\mathbf{k},\lambda}^* \hat{a}_{\mathbf{k},\lambda}^\dagger e^{-i(\mathbf{k}\cdot\mathbf{r}_A - \omega_{\mathbf{k}}t)} \right\} | I_1 \rangle \quad (\text{A.21})$$

In the previous equation, the operator $\hat{\mathbf{d}}_A$ only operates on the partial states $|A_{\text{ground}}\rangle$ and $|A_{n_i l_i m_i}\rangle$. The ladder operators, $\hat{a}_{\mathbf{k},\lambda}$ and $\hat{a}_{\mathbf{k},\lambda}^\dagger$ operate on the partial photon states $|N_{\mathbf{k},\lambda}\rangle$ such as $\hat{a}_{\mathbf{k},\lambda} |N_{\mathbf{k},\lambda}\rangle = \sqrt{N_{\mathbf{k},\lambda}} |N_{\mathbf{k},\lambda} - 1\rangle$ and $\hat{a}_{\mathbf{k},\lambda}^\dagger |N_{\mathbf{k},\lambda}\rangle = \sqrt{N_{\mathbf{k},\lambda} + 1} |N_{\mathbf{k},\lambda} + 1\rangle$. This way, equation A.21 is rewritten as

$$\begin{aligned} \langle f | \hat{H}_{QD}^{(\mathbf{r}=\mathbf{r}_A)} | I_1 \rangle &= -i \left(\frac{2\pi\hbar\omega_{\mathbf{k}}}{V\epsilon_1} \right)^{1/2} \langle A_{n_f l_f m_f} | \hat{\mathbf{d}}_A | A_{\text{ground}} \rangle \cdot \\ &\cdot \left\{ \mathbf{e}_{\mathbf{k},\lambda} e^{i(\mathbf{k}\cdot\mathbf{r}_A - \omega_{\mathbf{k}}t)} \langle N_{\mathbf{k},\lambda} | \hat{a}_{\mathbf{k},\lambda} | N_{\mathbf{k},\lambda} + 1 \rangle - \dots \right. \\ &\left. - \mathbf{e}_{\mathbf{k},\lambda}^* e^{-i(\mathbf{k}\cdot\mathbf{r}_A - \omega_{\mathbf{k}}t)} \langle N_{\mathbf{k},\lambda} | \hat{a}_{\mathbf{k},\lambda}^\dagger | N_{\mathbf{k},\lambda} + 1 \rangle \right\} \end{aligned} \quad (\text{A.22})$$

Only the first term of the curly brackets is non-zero. As in chapter 2.3.1, let us assume, without losing generality, that $N_{\mathbf{k},\lambda} = 0$. Defining, as well, $\mathbf{d}_A^{(f,g)} \equiv \langle A_{n_f l_f m_f} | \hat{\mathbf{d}}_A | A_{\text{ground}} \rangle$, equation A.22 is written as follows

$$\langle f | \hat{H}_{QD}^{(\mathbf{r}=\mathbf{r}_A)} | I_1 \rangle = -i \left(\frac{2\pi\hbar\omega_{\mathbf{k}}}{V\epsilon_1} \right)^{1/2} \left(\mathbf{d}_A^{(f,v)} \cdot \mathbf{e}_{\mathbf{k},\lambda} \right) e^{i(\mathbf{k}\cdot\mathbf{r}_A - \omega_{\mathbf{k}}t)} \quad (\text{A.23})$$

A similar procedure is taken for the remaining bra-kets of equation A.17. Thus, this equation is rewritten as

$$\begin{aligned} M_{i \rightarrow f} &= \frac{2\pi}{V\epsilon_1} \sum_{\mathbf{k},\lambda} \hbar\omega_{\mathbf{k}} \left\{ \frac{\left(\mathbf{d}_A^{(f,v)} \cdot \mathbf{e}_{\mathbf{k},\lambda} \right) \left(\mathbf{d}_D^{(v,i)} \cdot \mathbf{e}_{\mathbf{k},\lambda}^* \right)}{E_{n_i l_i}^{(D)} - \hbar\omega_{\mathbf{k}}} e^{i\mathbf{k}\cdot\mathbf{R}} - \dots \right. \\ &\left. - \frac{\left(\mathbf{d}_D^{(v,i)} \cdot \mathbf{e}_{\mathbf{k},\lambda} \right) \left(\mathbf{d}_A^{(f,v)} \cdot \mathbf{e}_{\mathbf{k},\lambda}^* \right)}{E_{n_i l_i}^{(D)} - \hbar\omega_{\mathbf{k}}} e^{i\mathbf{k}\cdot\mathbf{R}} \right\}, \end{aligned} \quad (\text{A.24})$$

where $\mathbf{d}_D^{(v,g)} \equiv \langle D_{\text{ground}} | \hat{\mathbf{d}}_D | D_{n_i l_i m_i} \rangle$ and $\mathbf{R} = \mathbf{r}_A - \mathbf{r}_D$. The matrix elements $\mathbf{d}_D^{(g,i)}$ and $\mathbf{d}_A^{(f,g)}$ will be further written as \mathbf{d}_D and \mathbf{d}_A , respectively, for notation simplicity. The sum over all polarizations is given by [5]

$$\sum_{\lambda} (\mathbf{d}_A \cdot \mathbf{e}_{\mathbf{k},\lambda}) (\mathbf{d}_D \cdot \mathbf{e}_{\mathbf{k},\lambda}^*) = \sum_{\alpha,\beta} (\delta_{\alpha\beta} - \hat{k}_{\alpha}\hat{k}_{\beta}) d_A^{\alpha} d_D^{\beta} \quad (\text{A.25})$$

where $\hat{k}_{\alpha,\beta} = k_{\alpha,\beta}/k$ and $\{\alpha, \beta\} \equiv x, y, z$. Introducing this result into equation A.24 yields

$$M_{i \rightarrow f} = \frac{2\pi}{V\epsilon_1} \sum_{\mathbf{k}} \hbar\omega_{\mathbf{k}} \left\{ \frac{e^{i\mathbf{k}\cdot\mathbf{R}}}{E_{n_i l_i}^{(D)} - \hbar\omega_{\mathbf{k}}} - \frac{e^{-i\mathbf{k}\cdot\mathbf{R}}}{E_{n_i l_i}^{(D)} + \hbar\omega_{\mathbf{k}}} \right\} \sum_{\alpha,\beta} (\delta_{\alpha\beta} - \hat{k}_{\alpha}\hat{k}_{\beta}) d_A^{\alpha} d_D^{\beta}. \quad (\text{A.26})$$

The sum over \mathbf{k} can be transformed into a volume integral over the wavevector space, as follows

$$\sum_{\mathbf{k}} \rightarrow \frac{V}{(2\pi)^3} \int d\mathbf{k}. \quad (\text{A.27})$$

Using the dispersion relation, $\omega_{\mathbf{k}} \equiv k \frac{c}{\sqrt{\epsilon_1}}$, equation A.26 is now rewritten as

$$M_{i \rightarrow f} = \frac{1}{(2\pi)^2 \epsilon_1} \int d\mathbf{k} \frac{\hbar c}{\sqrt{\epsilon_1}} k \left\{ \frac{e^{i\mathbf{k}\cdot\mathbf{R}}}{E_{n_i l_i}^{(D)} - \frac{\hbar c}{\sqrt{\epsilon_1}} k} - \frac{e^{-i\mathbf{k}\cdot\mathbf{R}}}{E_{n_i l_i}^{(D)} + \frac{\hbar c}{\sqrt{\epsilon_1}} k} \right\} \sum_{\alpha,\beta} (\delta_{\alpha\beta} - \hat{k}_{\alpha}\hat{k}_{\beta}) d_A^{\alpha} d_D^{\beta} \quad (\text{A.28})$$

If one takes that the vector \mathbf{R} is aligned along the z axis, one has that $\mathbf{k} \cdot \mathbf{R} = Rk \cos \theta$. One can also make the change of variable $-\cos \theta = z$ and define the constant $q = \frac{\sqrt{\epsilon_1}}{\hbar c} E_{n_i l_i}^{(D)}$. This way, the matrix element is equal to

$$\begin{aligned} M_{i \rightarrow f} &= \frac{1}{(2\pi)^2 \epsilon_1} \int_0^{2\pi} \int_{-1}^1 \int_0^{\infty} d\phi dz dk k^3 \left\{ \frac{e^{ikRz}}{q - k} - \frac{e^{-ikRz}}{q + k} \right\} \sum_{\alpha,\beta} (\delta_{\alpha\beta} - \hat{k}_{\alpha}\hat{k}_{\beta}) d_A^{\alpha} d_D^{\beta} \\ &= \frac{1}{\pi \epsilon_1} \int_0^{\infty} dk \frac{k^4}{q^2 - k^2} \int_{-1}^1 dz e^{ikRz} \sum_{\alpha,\beta} (\delta_{\alpha\beta} - \hat{k}_{\alpha}\hat{k}_{\beta}) d_A^{\alpha} d_D^{\beta} \end{aligned} \quad (\text{A.29})$$

The integral calculation of equation A.29 can be divided into two integrals,

$$\begin{aligned}
 I_1 &= \frac{1}{\pi\epsilon_1} \int_0^\infty dk \frac{k^4}{q^2 - k^2} \int_{-1}^1 dz e^{ikRz} \sum_{\alpha,\beta} \delta_{\alpha\beta} d_A^\alpha d_D^\beta \\
 &= -\frac{\mathbf{d}_A \cdot \mathbf{d}_D}{\epsilon_1} q^3 \frac{1}{qR} e^{iqR},
 \end{aligned} \tag{A.30}$$

and

$$\begin{aligned}
 I_2 &= -\frac{1}{\pi\epsilon_1} dk \frac{k^4}{q^2 - k^2} \int_{-1}^1 dz e^{ikRz} \sum_{\alpha,\beta} \hat{k}_\alpha \hat{k}_\beta d_A^\alpha d_D^\beta \\
 &= -\frac{q^3}{\epsilon_1} \left\{ \mathbf{d}_A \cdot \mathbf{d}_D \left(\frac{i}{(qR)^2} - \frac{1}{(qR)^3} \right) + d_A d_D \cos A \cos D \left(-\frac{1}{qR} - \frac{3i}{(qR)^2} + \frac{3}{(qR)^3} \right) \right\} e^{iqR}
 \end{aligned} \tag{A.31}$$

where A and D are the angles between the vector \mathbf{R} and the dipole moment matrix element of the acceptor QDot, d_A , and of the donor QDot, d_D , respectively. Summing the results from the two integrals, the energy transfer matrix element is in shorthand written as

$$\mathbf{M}_{i \rightarrow f} = \frac{1}{\epsilon_1} \mathbf{d}_A \mathbf{T} \mathbf{d}_D, \tag{A.32}$$

where the tensor \mathbf{T} is defined as,

$$\mathcal{T}_{\alpha\beta} \equiv -q^3 \left[A(qR) \delta_{\alpha\beta} + B(qR) n_\alpha n_\beta \right] e^{iqR}, \tag{A.33}$$

with $A(x) = \frac{1}{x} + \frac{i}{x^2} - \frac{1}{x^3}$, $B(x) = -\frac{1}{x} - \frac{3i}{x^2} + \frac{3}{x^3}$, $q = \frac{\sqrt{\epsilon_1}}{\hbar c} E_{nl}$ and $n_{\alpha,\beta} = R_{\alpha,\beta}/R$ is the unit vector of \mathbf{R} , i.e., $\mathbf{n} = \mathbf{R}/R$.

A.3 AVERAGE OF THE ENERGY TRANSFER MATRIX ELEMENT

From equation 2.51 of Chapter 2.3.1, the resonant energy transfer matrix element between a donor and acceptor in the near-field approximation is given by

$$M_{i \rightarrow f} = \frac{1}{\epsilon_1 R^3} \{ (\mathbf{d}_A \cdot \mathbf{d}_D) - 3(\mathbf{d}_A \cdot \mathbf{n})(\mathbf{d}_D \cdot \mathbf{n}) \}. \quad (\text{A.34})$$

where \mathbf{d}_D and \mathbf{d}_A are the donor and acceptor transition dipole moments, respectively, R is the donor-acceptor distance, \mathbf{n} is the unit vector of \mathbf{R} , such that $\mathbf{n} = \mathbf{R}/R$, and ϵ_1 is the dielectric constant of the surrounding medium. One assumes that the dipole moments \mathbf{d}_D and \mathbf{d}_A are randomly oriented in space. This is true for QDots made of an isotropic or highly symmetric material. Consequently, in order to calculate $|M_{i \rightarrow f}|^2$ it is usually considered the average term $\langle |M_{i \rightarrow f}|^2 \rangle$, as follows

$$\langle |M_{i \rightarrow f}|^2 \rangle = \frac{1}{\epsilon_1^2 R^6} \langle |(\mathbf{d}_A \cdot \mathbf{d}_D) - 3(\mathbf{d}_A \cdot \mathbf{n})(\mathbf{d}_D \cdot \mathbf{n})|^2 \rangle \quad (\text{A.35})$$

In this appendix we calculate the average in the right hand side of equation A.35. By expanding the squared modulus term, one has

$$\begin{aligned} & \langle |(\mathbf{d}_A \cdot \mathbf{d}_D) - 3(\mathbf{d}_A \cdot \mathbf{n})(\mathbf{d}_D \cdot \mathbf{n})|^2 \rangle = \\ & = \left\langle [(\mathbf{d}_A \cdot \mathbf{d}_D) - 3(\mathbf{d}_A \cdot \mathbf{n})(\mathbf{d}_D \cdot \mathbf{n})] \cdot [(\mathbf{d}_A^* \cdot \mathbf{d}_D^*) - 3(\mathbf{d}_A^* \cdot \mathbf{n})(\mathbf{d}_D^* \cdot \mathbf{n})] \right\rangle \\ & = \langle (\mathbf{d}_A \cdot \mathbf{d}_D)(\mathbf{d}_A^* \cdot \mathbf{d}_D^*) \rangle - 3\langle (\mathbf{d}_A^* \cdot \mathbf{n})(\mathbf{d}_D^* \cdot \mathbf{n})(\mathbf{d}_A \cdot \mathbf{d}_D) \rangle \\ & \quad - 3\langle (\mathbf{d}_A \cdot \mathbf{n})(\mathbf{d}_D \cdot \mathbf{n})(\mathbf{d}_A^* \cdot \mathbf{d}_D^*) \rangle + 9\langle (\mathbf{d}_A \cdot \mathbf{n})(\mathbf{d}_A^* \cdot \mathbf{n})(\mathbf{d}_D \cdot \mathbf{n})(\mathbf{d}_D^* \cdot \mathbf{n}) \rangle \end{aligned} \quad (\text{A.36})$$

As in Appendix A.2, it is assumed the vector \mathbf{R} (and, therefore the unit vector \mathbf{n}) is aligned with the z axis. The same vector \mathbf{R} makes an angle A with \mathbf{d}_A and an angle D with \mathbf{d}_D . The angle between both dipoles \mathbf{d}_A and an angle D with \mathbf{d}_D is γ (See Figure 36).

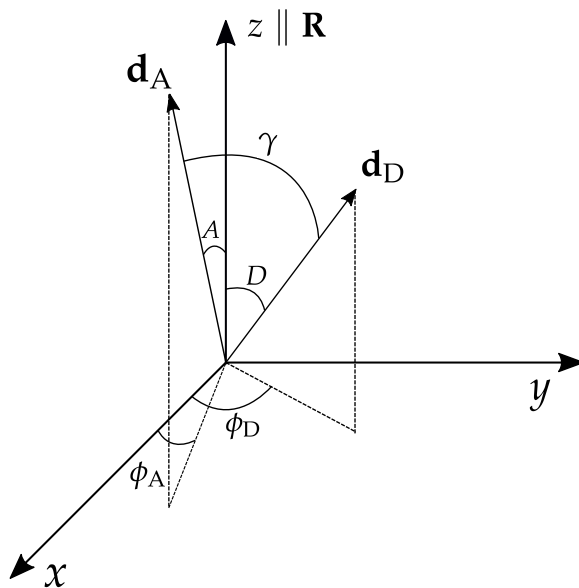


Figure 36: Schematic for the orientation of the transition dipole moments \mathbf{d}_A and \mathbf{d}_D in relation to the donor-acceptor distance vector \mathbf{R} , aligned with the z axis.

Let us calculate all individual average terms that contribute to equation A.36. The first term gives

$$\begin{aligned} \langle (\mathbf{d}_A \cdot \mathbf{d}_D)(\mathbf{d}_A^* \cdot \mathbf{d}_D^*) \rangle &= |\mathbf{d}_A|^2 |\mathbf{d}_D|^2 \langle (\cos \gamma)^2 \rangle \\ &= |\mathbf{d}_A|^2 |\mathbf{d}_D|^2 \frac{1}{4\pi} \int_0^{2\pi} d\phi_\gamma \int_0^\pi d\gamma (\cos \gamma)^2 \sin \gamma d\gamma = \frac{1}{3} |\mathbf{d}_A|^2 |\mathbf{d}_D|^2 \end{aligned} \quad (\text{A.37})$$

and the last term gives

$$\begin{aligned} \langle (\mathbf{d}_A \cdot \mathbf{n})(\mathbf{d}_A^* \cdot \mathbf{n})(\mathbf{d}_D \cdot \mathbf{n})(\mathbf{d}_D^* \cdot \mathbf{n}) \rangle &= |\mathbf{d}_A|^2 |\mathbf{d}_D|^2 \langle (\cos A)^2 \rangle \langle (\cos D)^2 \rangle \\ &= |\mathbf{d}_A|^2 |\mathbf{d}_D|^2 \left(\frac{1}{3} \times \frac{1}{3} \right) \\ &= \frac{1}{9} |\mathbf{d}_A|^2 |\mathbf{d}_D|^2 \end{aligned} \quad (\text{A.38})$$

The two middle terms $\langle(\mathbf{d}_A^* \cdot \mathbf{n})(\mathbf{d}_D^* \cdot \mathbf{n})(\mathbf{d}_A \cdot \mathbf{d}_D)\rangle$ and $\langle(\mathbf{d}_A \cdot \mathbf{n})(\mathbf{d}_D \cdot \mathbf{n})(\mathbf{d}_A^* \cdot \mathbf{d}_D^*)\rangle$ yield the same average value and, in order to relate γ with the angles A and D , we have the relation [61]

$$\cos \gamma = \cos A \cos D + \sin A \sin D \cos(\phi_A - \phi_D). \quad (\text{A.39})$$

This way, using the relation in equation A.39, each middle term yields

$$\begin{aligned} \langle(\mathbf{d}_A^* \cdot \mathbf{n})(\mathbf{d}_D^* \cdot \mathbf{n})(\mathbf{d}_A \cdot \mathbf{d}_D)\rangle &= |\mathbf{d}_A|^2 |\mathbf{d}_D|^2 \langle \cos \gamma \cos A \cos D \rangle \\ &= |\mathbf{d}_A|^2 |\mathbf{d}_D|^2 \left\{ \langle (\cos A)^2 (\cos D)^2 \rangle + \langle \cos A \sin A \cos D \sin D \cos(\phi_A - \phi_D) \rangle \right\} \\ &= |\mathbf{d}_A|^2 |\mathbf{d}_D|^2 \left(\frac{1}{9} + 0 \right) \\ &= \frac{1}{9} |\mathbf{d}_A|^2 |\mathbf{d}_D|^2. \end{aligned} \quad (\text{A.40})$$

Using results of equations A.37, A.38 and A.40 in equation A.36 gives

$$\begin{aligned} \langle |(\mathbf{d}_A \cdot \mathbf{d}_D) - 3(\mathbf{d}_A \cdot \mathbf{n})(\mathbf{d}_D \cdot \mathbf{n})|^2 \rangle &= |\mathbf{d}_A|^2 |\mathbf{d}_D|^2 \left(\frac{1}{3} - \frac{6}{9} + 1 \right) \\ &= \frac{2}{3} |\mathbf{d}_A|^2 |\mathbf{d}_D|^2. \end{aligned} \quad (\text{A.41})$$

Using the result of equation A.41 in equation A.35 gives the final result

$$\langle |M_{i \rightarrow f}|^2 \rangle = \frac{2}{3\epsilon_1^2 R^6} |\mathbf{d}_A|^2 |\mathbf{d}_D|^2. \quad (\text{A.42})$$

B

CALCULATIONS FROM EXPERIMENTAL DATA

B.1 CALCULATION OF THE ACCEPTOR CONCENTRATION AND THE AVERAGE QDOT SIZE IN COLLOIDAL QDOT SAMPLE "ONLY B"

Here we present the calculation of the ratio of acceptors QDots and the total number of QDots, described by the function η , for the sample Only B. From Chapter 5.3.2, the ratio η , assuming the donor radius as being the most probable QDot radius, \bar{R} , related with absorption peak, is given by

$$\eta(\bar{R}) = \frac{\bar{R}}{\sqrt{2\pi\sigma_R^2}} \frac{\Delta E}{2 [E(\bar{R}) - E_g]} \quad (\text{B.1})$$

where σ_R is the QDot size dispersion, i.e, standard deviation, ΔE is the width of the energy interval where the donor emission spectra and the acceptor emission spectrum overlap, $E(\bar{R})$ is the exciton energy for the most probable QDot radius and E_g is the bulk band-gap energy.

The ratio \bar{R}/σ_R is equivalent to find the ratio \bar{k}/σ_k , where k is the wavenumber, as found on the experimental spectrum of sample Only B. In Figure 37 it is presented the position of the peak wave number \bar{k} and values of k_1 and k_2 such that the full width at half maximum, FWHM, is given by $\text{FWHM} = |k_2 - k_1|$. The FWHM is related with the standard deviation as $\text{FWHM} = 2\sqrt{2\ln(2)}\sigma_k$. The estimated values of these values are $\bar{k} \approx 8220\text{cm}^{-1}$, $k_1 \approx 7800\text{cm}^{-1}$ and $k_2 \approx 8760\text{cm}^{-1}$. This way the ratio \bar{k}/σ_k is valued as

$$\frac{\bar{k}}{\sigma_k} = \frac{8220\text{cm}^{-1}}{(8760 - 7800)\text{cm}^{-1}} 2\sqrt{2\ln(2)} \simeq 20.2 \quad (\text{B.2})$$

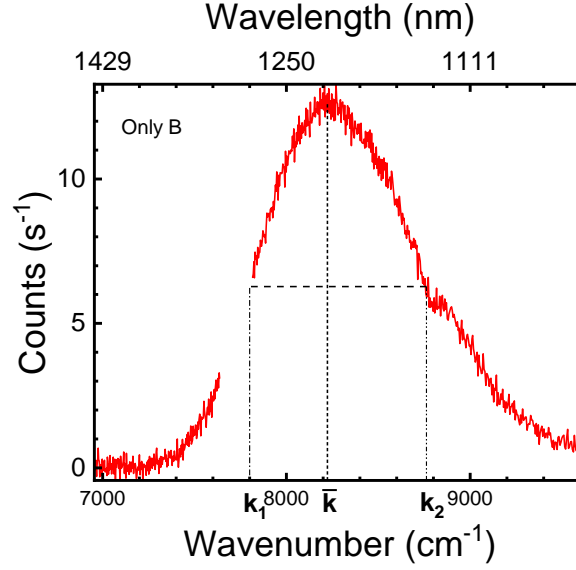


Figure 37: Estimation of the full width at half maximum and peak centre of the spectrum of the PbS sample Only B.

The calculation of $E(\bar{R})$ is equivalent to the calculation of $E(\bar{k})$, and it is given, in eV, by

$$E(\bar{k}) = \frac{1240}{10^7 \bar{k}^{-1}} = \frac{1240}{10^7 \times (8220 \text{cm}^{-1})^{-1}} \simeq 1.02 \text{eV} \quad (\text{B.3})$$

Using the results of Equations B.2 and B.3 into Equation B.1, assuming $\Delta E \approx 10^{-3} \text{eV}$ and $E_g = 0.41 \text{eV}$, i.e, the bulk PbS band-gap energy, we find the ratio η is estimated as

$$\eta = \frac{20.2 \times 10^{-3}}{2\sqrt{2\pi}(1.02 - 0.41)} \simeq 0.007 \approx 10^{-2}. \quad (\text{B.4})$$

The calculation of \bar{R} is possible by using the experimental sizing curve presented in Equation 1.2 in Chapter 1.2, defined as

$$E(d) = 0.41 + \frac{1}{0.0252 d^2 + 0.283 R'} \quad (\text{B.5})$$

where $d = 2R$, is the QDot diameter. Assuming $E(\bar{d}) = E(\bar{k})$ is known, \bar{R} is calculated by solving the quadratic formula

$$0.0252 \bar{d}^2 + 0.283 \bar{d} - \frac{1}{E(\bar{k}) - 0.41} = 0, \quad (\text{B.6})$$

where, from Equation B.3, $E(\bar{k}) \simeq 1.02\text{eV}$. Solving Equation B.6 gives only one real positive value which is

$$\bar{R} = \frac{d}{2} \simeq 2.1 \text{ nm} \quad (\text{B.7})$$

COMPUTATIONAL WORK

C.1 MATLAB CODE FOR FITTING PHOTOLUMINESCENCE KINETICS

```
function output = homFit(counts, us_bin, start_bin, end_bin)

% I(t) = A exp[-(B*t)^(1/2)*((B*t)^(1/2)+4/3*pi*D)] + C
% A - Amplitude
% B - Decay rate of donor emitter
% C - Background constant
% D - C_0 * R_0^3 (should give the number of acceptors at the Forster
    radius distance
% Formula used as derived in the thesis

% Generating array for all recorded time bins
time = (0:(end_bin - start_bin))*us_bin;

% Find number of analysed kinetics in a single run of the code, defined as N
if iscell(counts)
N = length(counts);
else
N = 1;
counts = {counts}; % Convert array to cell, easier to loop
end

% Generating matrices for all parameters and confidence interval bounds
amplitude = zeros(N, 1); % A parameter
damlplitude = zeros(N, 1); % A parameter 95% C.I.
```

```

gam = zeros(N, 1); % B parameter
dgam = zeros(N, 1); % B parameter 95% C.I.
tau = zeros(N, 1); % 1/B parameter
dtau = zeros(N, 1); % 1/B parameter 95% C.I.
background = zeros(N, 1); % C parameter
dbackground = zeros(N, 1); % C parameter 95% C.I.
NA = zeros(N, 1); % D parameter
dNA = zeros(N, 1); % D parameter 95% C.I.
chi2 = zeros(N, 1); % Chi reduced squared (fit quality)
coef = cell(N, 1); % All parameters [A, B, C]
conf = cell(N, 1); % All 95% C.I. for [A, B, C]
initials = cell(N, 1); % Initial fit parameters [A, B, C]
fit_out = cell(N, 1); % Output of fit function (debugging)
fit_gof = cell(N, 1); % Gof of fit function (debugging)
fit_fitobject = cell(N, 1); % Fitobject of fit function (debugging)
fprintf('Fitting %d datasets:\n', N);

for i = 1:N
% Cutting counts by start and end bin
fit_counts = counts{i}(start_bin:end_bin);
n_background = round((end_bin - start_bin - 1)/10);
background_guess = mean(fit_counts(end - n_background:end));

%The code has two fitting stages: At first the B and D parameters are
    fitted, and then all variables are fitted.

%Setting up initial parameters
Dinit = 4;
Cinit = background_guess; % First value of counts should be arround
    the value of background
Binit = 1; % Initial one microsecond assumption
Ainit = mean(fit_counts(1:20)) - Cinit; % Peak amplitude above noise

%Setting options for the 1st fit
fo_init = fitoptions('Method', 'NonlinearLeastSquares',...
' startPoint', [Binit, Dinit], ...
' Lower', [0,0], ... % Important!
' DiffMinChange', 1e-8, ...

```

```

'TolX', 1e-6, ...
'TolFun', 1e-6, ...
'MaxFunEvals', 500, ...
'MaxIter', 1000);
ft_init = fittype(@(B, D, x)
    Ainit.*exp(-((B.*x).^(0.5).*((B.*x).^(0.5)+(4/3)*pi*D))) + Cinit,
    'options', fo_init);

%Fitting
fitobject_init = fit(time, fit_counts, ft_init);

%Setting the fit results equal to the initial parameters
Binit = fitobject_init.B;
Dinit = fitobject_init.D;

if Binit > 20
Binit = 1;
end

% Adding initials to output
initials{i} = [Ainit, Binit, Cinit, Dinit];

% Fit options and equation for second and final fit
fo = fitoptions('Method', 'NonlinearLeastSquares', ...
'StartPoint', [Ainit, Binit, Cinit, Dinit], ...
'Lower', [0,0,0,0], ... % Important!
'DiffMinChange', 1e-8, ...
'TolX', 1e-6, ...
'TolFun', 1e-6, ...
'MaxFunEvals', 500, ...
'MaxIter', 1000);
ft = fittype(@(A, B, C, D, x)
    A.*exp(-((B.*x).^(0.5).*((B.*x).^(0.5)+(4/3)*pi*D))) + C, 'options',
    fo);

% Fitting
[fitobject, gof, out] = fit(time, fit_counts, ft);

```

```

coef{i} = coeffvalues(fitobject);
conf{i} = confbounds(fitobject);

% Calculating chi squared.
chi2(i) = sum((fit_counts - fitobject(time)).^2./fit_counts)/...
(length(fit_counts) - length(coef{i}));

% Adding readable parameters
amplitude(i) = coef{i}(1);
damplitude(i) = conf{i}(1);
gam(i) = coef{i}(2);
dgam(i) = conf{i}(2);
NA(i) = coef{i}(4);
dNA(i) = conf{i}(4);
tau(i) = 1/gam(i);          % tau = 1/B
dtau(i) = tau(i)^2*dgam(i); % dtau = (1/B)^2*dB
background(i) = coef{i}(3);
dbackground(i) = conf{i}(3);

% Adding fitting output for debugging purposes
fit_out{i} = out;
fit_gof{i} = gof;
fit_fitobject{i} = fitobject;

% Increasing progress counter
fprintf('Fitted dataset %d/%d.\n', i, N)
end

% Adding parameters to output struct
output.amplitude = amplitude;
output.damplitude = damplitude;
output.gamma = gam;
output.dgamma = dgam;
output.tau = tau;
output.dtau = dtau;
output.NA = NA;
output.dNA = dNA;
output.background = background;

```

```
output.dbackground = dbackground;
output.chi2 = chi2;
output.coef = coef;
output.conf = conf;
output.initials = initials;
output.fit_out = fit_out;
output.fit_gof = fit_gof;
output.fit_fitobject = fit_fitobject;
```

```
function cibounds = confbounds(fun, level)
%CONFBOUNDS Confidence interval bounds for the coefficients of a fit result
    object.
% CIBOUNDS = CONFBOUNDS(FITRESULT) returns 95% confidence bounds for the
% coefficient estimates, e.g. A = COEFFS(1) +- CIBOUNDS(1)
%
% CIBOUNDS = CONFBOUNDS(FITRESULT,LEVEL) specifies the confidence level.
% LEVEL must be between 0 and 1, and has a default value of 0.95.

% Copyright 2001-2008 The MathWorks, Inc. Modified by Matthijs Velsink,
% COPS, University of Twente.

if nargin < 2
    level = 0.95;
end

if length(level) ~= 1 || ~isnumeric(level) || level <= 0 || level >= 1
    error(message('curvefit:confint:invalidConfLevel'));
end

ci = confint(fun, level);
cibounds = (ci(2, :) - ci(1, :))/2;
```

C.2 NUMERICAL INTEGRATION OF EXPERIMENTAL DATA

Using the Simpson's rule, the integration of the function $f(t)$, over a range t_0 to t_f , is approximated in the following way:

$$\int_{t_0}^{t_f} f(t)dt = \frac{h}{3} [f_0 + 4(f_1 + f_3 + f_5 + \dots + f_{2n-1}) + 2(f_2 + f_4 + \dots + f_{2n-2}) + f_{2n}]. \quad (\text{C.1})$$

The truncation error of the numerical integral I , ΔI , i.e, the error due to the implicit approximation with the Simpson's rule is given by:

$$\Delta I \leq (t_f - t_0)h^4M/180, \quad (\text{C.2})$$

where h is the width of the sub-intervals and M is the upper bound of the fourth derivative of the function $|f^{(iv)}(t)|$, in which t must be in the range t_0 to t_f .

The following Matlab code describes the manual implementation of the Simpson's rule in the experimental data, including the calculation of the truncation error of equation C.2.

```
function output =simpsInt(X,Y)
%Manual implentation of Simpson's rule to numerical integration
%
%Simpson's rule is based on using a quadratic polynomial approximation to
    the function f(x) over a pair of subintervals.
%
% Joao Martins 10/2019

if size(X)~= size(Y)
error('Dimensions should be the same!');
end

m=size(X,1)-1; %size of fit must have an odd number of values
if (m/2)~=floor(m/2)
error('Value of m must be even!');
end

h=(X(end)-X(1))/m;
c=ones(1,size(Y,1));
c(2:2:size(c,2)-1)=4;
```

```

c(3:2:size(c,2)-2)=2;
I=h/3*c*Y;
%Calculate maximum bound error
M=max(gradient(gradient(gradient(gradient(Y))))));
Ierror=(X(end)-X(1))*h.^4*M/180;

output.I = I;
output.Ierror = Ierror;

```

C.3 STATISTICAL MOMENT CALCULATION OF EXPERIMENTAL DATA

```

function output = MomentFit(counts, us_bin, start_bin, end_bin,n)

if iscell(counts)
N = length(counts);
else
N = 1;
counts = {counts}; % Convert array to cell, easier to loop
end

time = (0:(end_bin-start_bin))'*us_bin;
decays = zeros(N,2*n);

for i=1:N
fits = counts {i}(start_bin:end_bin);

n_background = round((end_bin - start_bin - 1)/10);
background_guess = mean(fits(end - n_background:end));
fits = fits - background_guess;
for j=1:n
numerator = fits.*(time.^j);
denominator = fits;

%Using manually implemented Simpson rule to numerical integration (see code
    simpsInt)

int_num = simpsInt(time,numerator);

```



```

int_den = simpsInt(time,denominator);

decays(i,j) = int_num.I/int_den.I;
decays(i,n+j) = decays(i,j)*sqrt((int_num.Ierror/int_num.I)^2 +
    (int_den.Ierror/int_den.I)^2); %error
end
end

output.gamma = decays;
output.decay = time;

```

The use of the Simpson's rule on the studied experimental data over simpler methods of numerical integration, such as the trapezoidal rule, showed a very significant increase in accuracy in calculating the ratio of moments R_n , which was found to be of great importance when calculating higher order moments (see Figure 38).

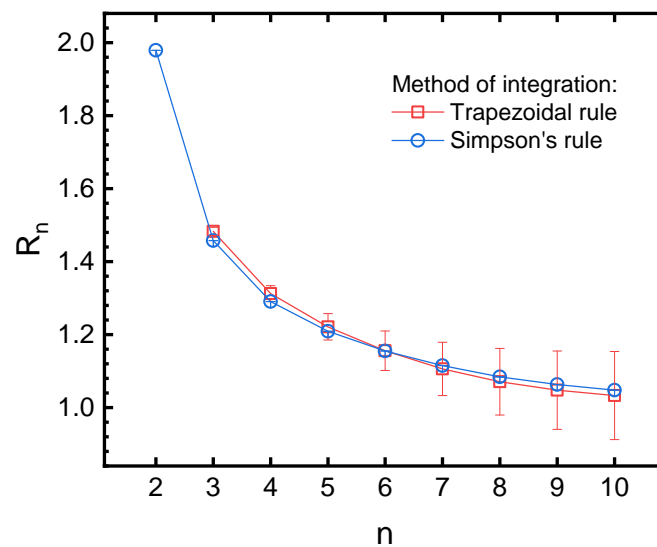


Figure 38: Comparison of results for the ratio R_n of an experimental decay curve for two types of numerical integration: trapezoidal rule (in red) and Simpson's rule (in blue). The use of the Simpson rule for higher moments n shows a clear advantage to the use of the trapezoidal rule, since it increases the accuracy of the numerical integration.

BIBLIOGRAPHY

- [1] M. Grundmann, *The Physics of Semiconductors*. Graduate Texts in Physics, Berlin, Heidelberg: Springer Berlin Heidelberg, 2010.
- [2] A. L. Rogach, *Semiconductor Nanocrystal Quantum Dots: Synthesis, Assembly, Spectroscopy and Applications*. Wien: Springer, 2008.
- [3] Y. Pathak and D. Thassu, *Drug Delivery Nanoparticles Formulation and Characterization*, vol. 191. 2016.
- [4] C. B. Murray, C. R. Kagan, and M. G. Bawendi, "Synthesis and Characterization of Monodisperse Nanocrystals and Close-Packed Nanocrystal Assemblies," *Annual Review of Materials Science*, vol. 30, pp. 545–610, Aug 2000.
- [5] G. D. Scholes and D. L. Andrews, "Resonance energy transfer and quantum dots," *Physical Review B - Condensed Matter and Materials Physics*, vol. 72, no. 12, pp. 1–8, 2005.
- [6] "Wikipedia page regarding Förster Resonance Energy Transfer."
https://en.wikipedia.org/wiki/F%C3%B6rster_resonance_energy_transfer.
Last visited on 28/07/2020.
- [7] C. Wang, M. S. Kodaimati, G. C. Schatz, and E. A. Weiss, "The photoluminescence spectral profiles of water-soluble aggregates of PbS quantum dots assembled through reversible metal coordination," vol. 53, no. 12, pp. 1981–1984, 2017.
- [8] I. Moreels, K. Lambert, D. Smeets, and D. De Muynck, "Size-Dependent Optical Properties of Colloidal PbS Quantum Dots," *Acs Nano*, vol. 3, no. 10, pp. 3023–3030, 2009.
- [9] L. Novotny and B. Hecht, *Principle of Nano Optics*. Cambridge, 2nd ed., 2012.
- [10] W. Becker, *Advanced Time-Correlated Single Photon Counting Techniques*. Springer Berlin Heidelberg, 2005.

- [11] M. Wahl, "Technical note for Time-Correlated Single Photon from company PicoQuant GmbH." https://www.picoquant.com/images/uploads/page/files/7253/technote_tcspc.pdf, 2014. Last visited on 28/07/2020.
- [12] J. R. Lakowicz, *Principles of Fluorescence Spectroscopy*, vol. 10. Springer, 3rd ed., 2018.
- [13] B. H. Husken, *Spontaneous emission lifetimes of infrared quantum dots controlled with photonic crystals*. PhD thesis, Jun 2009.
- [14] "Wikipedia page regarding the Glutathione molecule." <https://en.wikipedia.org/wiki/Glutathione>. Last visited on 28/07/2020.
- [15] G. T. Hermanson, *Bioconjugate Techniques*. Elsevier Inc., 2nd ed., 2008.
- [16] "Thermo Fisher Scientific user guide for the use of N-hydroxysuccinimide (NHS) and N-hydroxysulfosuccinimide (sulfo-NHS)." https://assets.thermofisher.com/TFS-Assets/LSG/manuals/MAN0011309_NHS_SulfoNHS_UG.pdf.
- [17] "Wikipedia page regarding Semiconductor Quantum Dots." https://en.wikipedia.org/wiki/Quantum_dot.
- [18] D. Bera, L. Qian, T. K. Tseng, and P. H. Holloway, "Quantum dots and their multimodal applications: A review," *Materials*, vol. 3, no. 4, pp. 2260–2345, 2010.
- [19] M. I. Vasilevskiy and I. C. Ferreira, *Física dos Semicondutores - Fundamentos, Aplicações e Nanoestruturas*. Almedina, 2006.
- [20] D. Bimberg, M. Grundmann, and N. N. Ledentsov, *Quantum Dot Heterostructures*. John Wiley & Sons, 1999.
- [21] V. K. LaMer and R. H. Dinegar, "Theory, Production and Mechanism of Formation of Monodispersed Hydrosols," *Journal of the American Chemical Society*, vol. 72, pp. 4847–4854, Nov 1950.
- [22] C. Burda, X. Chen, R. Narayanan, and M. A. El-Sayed, *Chemistry and properties of nanocrystals of different shapes*, vol. 105. 2005.
- [23] B. J. M. Klostranec and W. C. W. Chan, "Quantum Dots in Biological and Biomedical Research : Recent Progress and Present Challenges," pp. 1953–1964, 2006.

- [24] S. Brkić, "Applicability of Quantum Dots in Biomedical Science Applicability of Quantum Dots in Biomedical Science," 2017.
- [25] P. Patnaik, *Handbook of inorganic chemicals*, vol. 40. McGraw-Hill, 2003.
- [26] Y. Wang, A. Suna, W. Mahler, and R. Kasowski, "PbS in polymers. From molecules to bulk solids," *The Journal of Chemical Physics*, vol. 87, no. 12, pp. 7315–7322, 1987.
- [27] M. A. Hines and G. D. Scholes, "Colloidal PbS Nanocrystals with Size-Tunable Near-Infrared Emission: Observation of Post-Synthesis Self-Narrowing of the Particle Size Distribution," *Advanced Materials*, vol. 15, no. 21, pp. 1844–1849, 2003.
- [28] K. K. Nanda, F. E. Kruis, H. Fissan, and S. N. Behera, "Effective mass approximation for two extreme semiconductors: Band gap of PbS and CuBr nanoparticles," *Journal of Applied Physics*, vol. 95, no. 9, pp. 5035–5041, 2004.
- [29] Y. Wang, A. Suna, W. Mahler, and R. Kasowski, "PbS in polymers. From molecules to bulk solids," vol. 87, no. 12, pp. 7315–7322, 1987.
- [30] I. Moreels, G. Allan, B. De Geyter, L. Wirtz, C. Delerue, and Z. Hens, "Dielectric function of colloidal lead chalcogenide quantum dots obtained by a Kramers-Krönig analysis of the absorbance spectrum," *Physical Review B - Condensed Matter and Materials Physics*, vol. 81, no. 23, pp. 1–7, 2010.
- [31] J. H. Song and S. Jeong, "Colloidal quantum dot based solar cells: from materials to devices," *Nano Convergence*, vol. 4, no. 1, pp. 1–8, 2017.
- [32] R. S. Kane, R. E. Cohen, and R. Silbey, "Theoretical study of the electronic structure of PbS nanoclusters," *Journal of Physical Chemistry*, vol. 100, no. 19, pp. 7928–7932, 1996.
- [33] D. Kumar, S. Chaudhary, and D. K. Pandya, "Fabrication of PbS quantum dots and their applications in solar cells based on ZnO nanorod arrays," *AIP Conference Proceedings*, vol. 1953, pp. 1–5, 2018.
- [34] F. W. Wise, "Lead salt quantum dots: The limit of strong quantum confinement," *Accounts of Chemical Research*, vol. 33, no. 11, pp. 773–780, 2000.

- [35] Y. Liu, D. Kim, O. P. Morris, D. Zhitomirsky, and J. C. Grossman, "Origins of the Stokes Shift in PbS Quantum Dots: Impact of Polydispersity, Ligands, and Defects," *ACS Nano*, vol. 12, no. 3, pp. 2838–2845, 2018.
- [36] O. Voznyy, L. Levina, F. Fan, G. Walters, J. Z. Fan, A. Kiani, A. H. Ip, S. M. Thon, A. H. Proppe, M. Liu, and E. H. Sargent, "Origins of Stokes Shift in PbS Nanocrystals," *Nano Letters*, vol. 17, no. 12, pp. 7191–7195, 2017.
- [37] T. Walsh, J. Miloszewski, U. Aeberhard, and S. Tomić, "Electronic states of elongated PbSe/PbS Core/shell quantum dots," *Journal of Physics: Conference Series*, vol. 526, no. 1, 2014.
- [38] I. Kang and F. W. Wise, "Electronic structure and optical properties of PbS and PbSe quantum dots," *Journal of the Optical Society of America B*, vol. 14, no. 7, p. 1632, 1997.
- [39] I. Moreels, K. Lambert, D. De Muynck, F. Vanhaecke, D. Poelman, J. C. Martins, G. Allan, and Z. Hens, "Composition and size-dependent extinction coefficient of colloidal PbSe quantum dots," *Chemistry of Materials*, vol. 19, no. 25, pp. 6101–6106, 2007.
- [40] M. D. Leistikow, A. P. Mosk, E. Yeganegi, S. R. Huisman, A. Lagendijk, and W. L. Vos, "Inhibited spontaneous emission of quantum dots observed in a 3D photonic band gap," *Physical Review Letters*, vol. 107, no. 19, pp. 1–5, 2011.
- [41] B. H. Husken, A. F. Koenderink, and W. L. Vos, "Angular redistribution of near-infrared emission from quantum dots in three-dimensional photonic crystals," *Journal of Physical Chemistry C*, vol. 117, no. 7, pp. 3431–3439, 2013.
- [42] Elahe Yeganegi, *Controlling emission and propagation of light with photonic band gap crystals*. PhD thesis, University of Twente, 2014.
- [43] C. Barth, S. Roder, D. Brodoceanu, T. Kraus, M. Hammerschmidt, S. Burger, and C. Becker, "Increased fluorescence of PbS quantum dots in photonic crystals by excitation enhancement," *Applied Physics Letters*, vol. 111, no. 3, 2017.
- [44] H. Lee, H. C. Leventis, S. J. Moon, P. Chen, S. Ito, S. A. Haque, T. Torres, F. Nüesch, T. Geiger, S. M. Zakeeruddin, M. Grätzel, and M. K. Nazeeruddin, "PbS and CdS quantum dot-sensitized solid-state solar cells: "Old concepts, new results"," *Advanced Functional Materials*, vol. 19, no. 17, pp. 2735–2742, 2009.

- [45] J. Tian, T. Shen, X. Liu, C. Fei, L. Lv, and G. Cao, "Enhanced Performance of PbS-quantum-dot-sensitized Solar Cells via Optimizing Precursor Solution and Electrolytes," *Scientific Reports*, vol. 6, no. March, pp. 1–9, 2016.
- [46] R. Gill, M. Zayats, and I. Willner, "Semiconductor quantum dots for bioanalysis," *Angewandte Chemie - International Edition*, vol. 47, no. 40, pp. 7602–7625, 2008.
- [47] S. Hoogland, V. Sukhovatkin, I. Howard, S. Cauchi, L. Levina, and E. H. Sargent, "A solution-processed 1.53 μm quantum dot laser with temperature-invariant emission wavelength," *Optics Express*, vol. 14, no. 8, p. 3273, 2006.
- [48] A. Sashchiuk, D. Yanover, A. Rubin-Brusilovski, G. I. Maikov, R. K. Čapek, R. Vaxenburg, J. Tilchin, G. Zaiats, and E. Lifshitz, "Tuning of electronic properties in IV-VI colloidal nanostructures by alloy composition and architecture," *Nanoscale*, vol. 5, no. 17, pp. 7724–7745, 2013.
- [49] T. Förster, "Zwischenmolekulare Energiewanderung und Fluoreszenz," *Annalen der Physik*, vol. 437, pp. 55–75, Jan 1948. Last visited on 28/07/2020.
- [50] Q. Wen, S. V. Kershaw, S. Kalytchuk, O. Zhovtiuk, C. Reckmeier, M. I. Vasilevskiy, and A. L. Rogach, "Impact of D₂O/H₂O Solvent Exchange on the Emission of HgTe and CdTe Quantum Dots: Polaron and Energy Transfer Effects," *ACS Nano*, vol. 10, no. 4, pp. 4301–4311, 2016.
- [51] "Florida State University webpage regarding the Jablonski diagram." <https://micro.magnet.fsu.edu/primer/java/jablonski/lightandcolor/index.html>, 2016. Last visited on 28/07/2020.
- [52] S. A. Hussain, "An Introduction to Fluorescence Resonance Energy Transfer (FRET)," pp. 1–4, 2009.
- [53] D. Devashish, O. S. Ojambati, S. B. Hasan, J. J. Van Der Vegt, and W. L. Vos, "Three-dimensional photonic band gap cavity with finite support: Enhanced energy density and optical absorption," *Physical Review B*, vol. 99, no. 7, pp. 1–16, 2019.
- [54] M. Wubs and W. L. Vos, "Förster resonance energy transfer rate in any dielectric nanophotonic medium with weak dispersion," *New Journal of Physics*, vol. 18, no. 5, pp. 1–20, 2016.

- [55] K. K. Nanda, F. E. Kruis, and H. Fissan, "Energy Levels in Embedded Semiconductor Nanoparticles and Nanowires," *Nano Letters*, vol. 1, no. 11, pp. 605–611, 2001.
- [56] J. L. Marín, R. Riera, and S. A. Cruz, "Confinement of excitons in spherical quantum dots," vol. 10, pp. 1349–1361, Feb 1998.
- [57] C. Fang, W. F. Li, R. S. Koster, J. Klimeš, A. Van Blaaderen, and M. A. Van Huis, "The accurate calculation of the band gap of liquid water by means of GW corrections applied to plane-wave density functional theory molecular dynamics simulations," *Physical Chemistry Chemical Physics*, vol. 17, no. 1, pp. 365–375, 2015.
- [58] J.-L. Liu, "Mathematical modeling of semiconductor quantum dots based on the nonparabolic effective-mass approximation," vol. 1, no. 1, pp. 58–79, 2013.
- [59] K. K. Nanda, F. E. Kruis, H. Fissan, and S. N. Behera, "Effective mass approximation for two extreme semiconductors: Band gap of PbS and CuBr nanoparticles," *Journal of Applied Physics*, vol. 95, no. 9, pp. 5035–5041, 2004.
- [60] C. Wang, M. S. Kodaimati, G. C. Schatz, and E. A. Weiss, "The photoluminescence spectral profiles of water-soluble aggregates of PbS quantum dots assembled through reversible metal coordination," *Chemical Communications*, vol. 53, no. 12, pp. 1981–1984, 2017.
- [61] J. D. Jackson, *Classical Electrodynamics*. John Wiley & Sons, 1999.
- [62] E. Fermi, "Quantum Theory of Radiation," *Reviews of Modern Physics*, vol. 4, pp. 87–132, Jan 1932.
- [63] W. L. Barnes, S. A. R. Horsley, and W. L. Vos, "Classical antennae, quantum emitters, and densities of optical states," *Journal of Optics*, vol. 22, Feb 2020.
- [64] D. L. Andrews and B. S. Sherborne, "Resonant excitation transfer: A quantum electro-dynamical study," *The Journal of Chemical Physics*, vol. 86, pp. 4011–4017, Apr 1987.
- [65] C. R. Kagan, C. B. Murray, and M. G. Bawendi, "Long-range resonance transfer of electronic excitations in close-packed CdSe quantum-dot solids," *Physical Review B*, vol. 54, pp. 8633–8643, Sep 1996.
- [66] F. Peres, *Transferência Ressonante de Energia entre Pontos Quânticos*. Bachelor thesis, University of Minho, 2014.

- [67] D. L. Dexter, "A theory of sensitized luminescence in solids," *The Journal of Chemical Physics*, vol. 21, no. 5, pp. 836–850, 1953.
- [68] M. McIrvin, "Physics FAQ: Some Frequently Asked Questions About Virtual Particles."
http://math.ucr.edu/home/baez/physics/Quantum/virtual_particles.html, 1994. Last visited on 28/07/2020.
- [69] A. Zee, *Quantum Field Theory in a Nutshell*. Princeton University Press, 2nd ed., 2010.
- [70] R. Dick, *Advanced Quantum Mechanics: Materials and Photons*. Graduate Texts in Physics, Springer International Publishing, 2nd ed., 2016.
- [71] J. P. S. Farinha and J. M. G. Martinho, "Resonance Energy Transfer in Polymer Nanodomains," *The Journal of Physical Chemistry C*, vol. 112, pp. 10591–10601, Jul 2008.
- [72] M. Born and E. Wolf, *Principles of Optics: Electromagnetic Theory of Propagation, Interference and Diffraction of Light*. Cambridge University Press, 7th ed., 1980.
- [73] D. Dexter, R. Knox, and M. Stavola, "Electron-hole pair excitation in semiconductors via energy transfer from an external sensitizer," *Physical Review B*, vol. 31, no. 4, pp. 2277–2289, 1985.
- [74] A. F. Van Driel, I. S. Nikolaev, P. Vergeer, P. Lodahl, D. Vanmaekelbergh, and W. L. Vos, "Statistical analysis of time-resolved emission from ensembles of semiconductor quantum dots: Interpretation of exponential decay models," *Physical Review B - Condensed Matter and Materials Physics*, vol. 75, no. 3, 2007.
- [75] E. N. Bodunov and A. L. Simões Gamboa, "Kinetics of Photoluminescence Decay of Colloidal Quantum Dots: Nonexponential Behavior and Detrapping of Charge Carriers," *Journal of Physical Chemistry C*, vol. 122, no. 19, pp. 10637–10642, 2018.
- [76] D. Deng, J. Xia, J. Cao, L. Qu, J. Tian, Z. Qian, Y. Gu, and Z. Gu, "Forming highly fluorescent near-infrared emitting PbS quantum dots in water using glutathione as surface-modifying molecule," *Journal of Colloid and Interface Science*, vol. 367, no. 1, pp. 234–240, 2012.
- [77] W. M. Haynes, *Handbook of Chemistry and Physics*. CRC Press, 2014.

- [78] A. Foubert, N. V. Beloglazova, A. Rajkovic, B. Sas, A. Madder, I. Y. Goryacheva, and S. De Saeger, "Bioconjugation of quantum dots: Review & impact on future application," *Trends in Analytical Chemistry*, vol. 83, pp. 31–48, Oct 2016.
- [79] J. W. Goodman, *Statistical Optics*. John Wiley & Sons, 2000.
- [80] "Wikipedia page regarding Moments in mathematics."
[https://en.wikipedia.org/wiki/Moment_\(mathematics\)](https://en.wikipedia.org/wiki/Moment_(mathematics)). Last visited on 03/08/2020.
- [81] G. B. Arfken, H. J. Weber, and F. E. Harris, *Mathematical Methods for Physicists*. Elsevier Inc., 7th ed., 2013.
- [82] G. Lindfield and J. Penny, *Numerical Methods: Using MATLAB*. Academic Press, 3rd ed., 2012.
- [83] S. W. Clark, J. M. Harbold, and F. W. Wise, "Resonant energy transfer in PbS quantum dots," *Journal of Physical Chemistry C*, vol. 111, no. 20, pp. 7302–7305, 2007.
- [84] R. Bose, J. F. McMillan, J. Gao, K. M. Rickey, C. J. Chen, D. V. Talapin, C. B. Murray, and C. W. Wong, "Temperature-tuning of near-infrared monodisperse quantum dot solids at 1.5 μm for controllable Förster energy transfer," *Nano Letters*, vol. 8, no. 7, pp. 2006–2011, 2008.
- [85] C. Blum, N. Zijlstra, A. Lagendijk, A. P. Mosk, W. L. Vos, M. Wubs, and V. Subramaniam, "Nanophotonic control of the Förster resonance energy transfer efficiency," *Physical Review Letters*, vol. 109, no. 20, pp. 1–5, 2012.
- [86] "Notes of the Sokhotski-Plemelj Formula by the Santa Cruz Institute for Particle Physics." <http://scipp.ucsc.edu/~haber/ph214/Plemelj.pdf>, 2017. Last visited on 28/07/2020.